Cranfield University

MULTIPOINT GAS DETECTION USING RANGE RESOLVED INTERFEROMETRY

JAMES BREMNER

Centre for Engineering Photonics
School of Aerospace, Transport and Manufacturing

PhD Thesis

Academic Years: 2017-2021
Submitted: July 2021

Supervisors: Dr Jane Hodgkinson
Dr Thomas Kissinger
Prof Ralph Tatam

ABSTRACT

The ability to detect and quantify gas in multiple locations is important in environmental and safety monitoring situations. This thesis describes the first application of Range Resolved Interferometry to the problem of gas sensing at multiple locations. Range resolved interferometry (RRI) is an interferometric signal processing technique that allows the separation of individual interferometric signals from superpositions of multiple interferometers and the rejection of interferometers other than those of interest. This allows the interrogation of the light intensity passing through each interferometer of interest which in turn allows a measure of the absorption of light by gas present within the interferometer arms. The application of the Beer-Lambert Law allows the measurement of a gas concentration from this information. Unlike previous interferometric techniques for multipoint gas measurement, RRI uses injection current modulation of a DFB laser and is therefore, cost effective.

The process of applying a ramp modulation to RRI in order to extract spectroscopic information is described along with the post-processing needed to extract gas concentrations from multiple locations simultaneously.

Three sensing regions were interrogated and the system was shown to have good linearity of response ($R^2 < 0.95$) and with the ability to measure methane at a concentration of 200ppm with no averaging time. Allen-Werle analysis showed that with sufficient averaging time, a limit of detection as low as 4ppm could be achieved. Cross talk experiments showed that the presence of gas in other sensing regions had no effect on gas concentration measurements.

The first use of RRI for spectroscopic measurements required extensive post-processing to account for the DFB laser's non-uniform response to sinusoidal

modulation as the driving injection current was varied to sweep the laser output wavelength. Application of an envelope function to the sinusoidal modulation provided a stable wavelength response to the sinusoidal modulation and so allowed real-time gas detection with no post processing required.

Experiments were performed to establish that the most suitable deployment topology for multipoint sensing is a serial-bus topology and that the amplitude of the sinusoidal modulation must be chosen to provide the chosen balance between the spatial resolution of the system and the signal strength provided by the measurement of light absorption by the gas under test.

The ability of RRI to distinguish between interferometers of interest and parasitic interferometers was used to extract the absorption measurements from a gas detection system with optical fringing and was shown to reduce the unwanted signal by a factor of 18.

ACKNOWLEDGMENTS

Ralph Tatam, Jane Hodgkinson and Thomas Kissinger: Some advice I read before starting this PhD said that the key was finding some work you could be interested in, and people who made you want to keep working at it even when it wasn't interesting. As my supervising team, you provided both of those things. The chance to work on this cross-over of technologies and problems was wonderful, and you all drove me to do the best at it that I could. You, along with the other academic staff, also made for a wonderful work environment.

As did all the students with whom I overlapped in my time in Engineering Photonics. Whether you were being imported to debug my code, showing me how to operate lasers or just laughing at me as I failed to live up to the spicy wings standards you all set. In particular, Sam and Kieran. Thank you for all the help and all the companionship in what could have been much harder times.

And of course Steve Staines, thank you for all the assistance, guidance and little(?) fixes along the way.

Going further back, I have to thank Chris Dewdney for making Physics at Portsmouth a thing once more and so making it so I could get to this point, and David Franklin for helping me make my way through the Portsmouth experience. And speaking of Portsmouth; Aidan, Alex, Chris, Dan, Jacob, Jack, Kate, Lucy, Sam, discussions have been so fruitful and long may they continue!

And lastly, to family matters. Mum, Dad, I got there in the end! And Helen, you did so much to help me get there, not least of which was moving yourself to a place we had never heard of just so I could do this. Thank you. It's a magical world, Helen, ol' buddy... Let's go exploring!

CONTENTS

LIST OF FIGURES

LIST OF TABLES

MATHEMATICAL CONSTANTS AND ABBREVIATIONS

α	Absorption coefficiant
η	OPD
λ	Wavelength
λ_{opt}	Optical wavelength
μ	Frequency
ξ	Fractional loss of light intensity
Φ	Optical phase
ϕ	Arbitary constant
τ	Time delay
υ	Arbitary constant
χ	Arbitary constant
ω_m	Angular frequency of modulation
ω	Angular frequency
A_{sm}	Amplitude of voltage modulation
A_d	Phase modulation amplitude of a demodulation signal
A_k	Phase modulation amplitude over a modulation period
A_n	Phase modulation amplitude associated with a given interferometer
a	Arbitary constant
A	Amplitude
b	Arbitary constant
C_{ideal}	The calculated ideal coupler ratio for any given system
C_n	Complex value of a notional interferometric
C_o	Coupler ratio
C	Gas concentration
c	Arbitary constant
c_0	Speed of light
$D(t)$	Demodulated signal
d	Arbitary constant
E	Energy
f_{opt}	Optical frequency
h	Height of absorption peak
$\hbar$	Reduced Planck's constant
I_0	Initial light intensity

I_D	Laser driving current
I	Light intensity
L_a	Arbitary length of optical fibre
L_b	Arbitary length of optical fibre
L_{ci}	Length of a circulator arm
L_{co}	Length of a coupler arm
L	Gas interaction length
n	Arbitary constant
P(t)	Function used to envelope sinusoidal modulation amplitude
P	Power
Q(t)	Quadrature signal
R_e	Repsonsivity of detector
R	Reflectivity
S_{bb}	Broadband suppression ratio
t	Time
U(t)	Photodetector signal
v	Velcoity
V	Visibility of fringes
Z	RRI Amplitude, the amplitude of Q(t)

AU	Absorbance units
CLaDS	Chirped laser dispersion spectroscopy
CH_4	Methane
CO_2	Carbon dioxide
DFB	Distributed feedback laser
FID	Flame ionisation detector
FSR	Free spectral range
FWHM	Full width half maximum
LOD	Limit of detection
NDIR	Non dispersive infra red detection
OSA	Optical spectrum analyser
ppm	Parts per million
QCM	Quartz Crystal microbalance
TDLS	Tunable diode laser spectroscopy
VOC	Volatile organic compound
WMS	Wavelength modulation spectroscopy

INTRODUCTION

1.1 THE NEED FOR MULTIPOINT GAS SENSING

The detection and quantification of gases is an important part of a number of processes. It plays a role in health monitoring of patients[1, 2], environmental monitoring[3, 4], and safety monitoring[5, 6]. In environmental terms, anthropogenic climate change has been described by the UN as "one of the most pressing issues of our time"[7] and is primarily caused by the release of carbon based gases into the atmosphere by industrial processes. The Paris Climate Agreement binds countries to work towards lowering their contributions to the release of these greenhouse gases[8]. One key greenhouse gas is methane, which has a global warming impact over 20 times greater than that of carbon dioxide over 100 years[9]. This means that any attempt to lower climate change will require the monitoring of sources of methane emissions.

In terms of safety, the risks to human health from gases can come from toxicity, such as with the presence of formaldehyde [10] or carbon monoxide[11], or come from the potential for explosions. The build up of natural gas has been judged to be associated with up 70% of explosions on offshore oil or gas platforms[12] making the detection of natural gas, or the components thereof, a safety critical process in these locations as well as in others such as mines or along gas transport infrastructure. Methane is the main component of natural gas and has the capability to ignite explosively when it is mixed with air in concentrations between 5% and 15%[13], therefore sensors must be designed to be able to detect methane at concentrations lower than 20% of the lower explosion limit so

that action can be taken before conditions with these explosive concentrations can develop. In addition, the sensing regime must be able to detect plumes of methane before they reach 6m in length as it is at this size that any ignition will be a hazard to equipment and human life[14]. This means that a regime of sensing must include the ability to detect methane over an area rather than just in a single location. Similarly, for environmental purposes, in locations such as landfill sites, which are sources of methane emissions need to be monitored over a large area, meaning many sensors or wide area sensing technologies must be employed[15].

1.2   GAS SENSING TECHNIQUES

Gas sensing technologies can be broadly divided into two types, non-optical and optical. Non-optical sensor technologies include those that detect changes in the electro-chemical properties of a medium in the presence of gases[16], the ionisation of the gas in the presence of a flame[17] or the change in mechanical or electrical properties when a gas adsorbs to a surface[18]. Optical sensors operate by exploiting the interactions between light and matter for their sensing mechanism. These sensors can offer high selectivity and specificity of gas detection[19] as well as the advantage that they can be coupled with fibre optics, allowing flexibility of placement with the more complex parts of the sensing apparatus placed in more convenient location rather than directly in the sensing environment, which can keep electrical equipment away from any explosive gases.

1.2.1   *Tunable Diode Laser Spectroscopy*

One particular form of optical gas sensing, and the one most closely related to the work presented in this thesis is tunable diode laser spectroscopy (TDLS). This is a system based on the fact that many gas species will absorb light at specific

wavelengths while remaining transparent to other frequencies. This means that a gas will have a characteristic absorption spectrum made up of a number of absorption features[20]. By tuning a laser so that its output wavelength crosses one of these absorption features, some of that light will be absorbed in proportion to the concentration of the absorbing gas. Because the lasers used in TDLS have narrow line widths, they are able to trace an absorption feature with a high resolution. This makes sensors based on this technique highly selective in the gas they can be tuned to respond to[21].
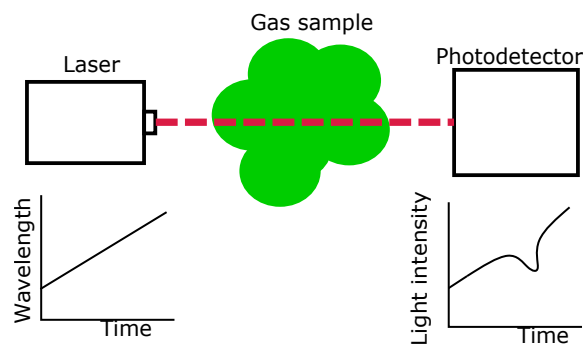
Figure 1.1: If a laser beam, passing through a gas sample has its wavelength changed, the amount of photons that pass through will vary as a function of that wavelength. When the wavelength matches the wavelength at which the gas absorbs photons, fewer will pass through and so a detector after the gas sample will record a lower incident light intensity.

1.3   MULTIPOINT OPTICAL SENSING

When sensing measurands in multiple locations at once, a number of strategies can be used. The simplest is the use of multiple, independent sensors. But, given the cost of individual parts of an optical sensor such as the laser, this is not cost-effective. A number of strategies have been developed that allow the measurement of gas concentrations at multiple locations using fewer components than would be necessary in the deployment of individual sensors.

The use of a fibre optic splitter allows the light from a single laser source to be used to perform TDLS measurements at a number of locations[22] with each

location being served by its own photodetector. This system, referred to as spatial multiplexing has been used to measure up to 64 locations simultaneously. A system that measures multiple locations using a single sensor can be set up using time division multiplexing. In this system, the sensing locations are each coupled to the laser and the photosensor using differing lengths of optical fibre. Thus, the time taken for a pulse to reach the photodetector via the sensing region can be used as a measure of the distance to that sensing region. Finally, multiple sensing regions can be interrogated with different frequencies of light, and this can be used to identify signals returning from different sensing regions[23]. Often, these frequency division multiplexed systems operate by combining the light returning from the different sensing regions with another light path and investigating the different interferences that occur as a result. A related process is at the heart of Range Resolved Interferometry (RRI) the multiplexing technique used in this thesis.

1.3.1   *Range Resolved Interferometry*

If a number of sensing regions are joined to form a complex interferometer and are interrogated using sinusoidally modulated laser light, then an interferometric pattern will be produced. This interferogram will be the superposition of all the constituent interferometers present in the system. Range Resolved Interferometry allows the extraction of information from each of these interferometers without the more complex laser modulation systems required in other, similar systems[24][25]
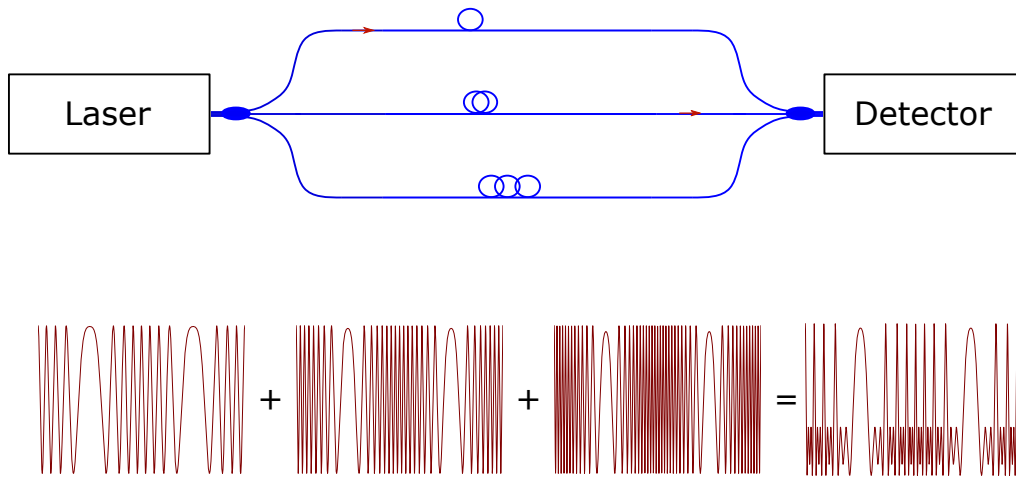
Figure 1.2: A system of multiple interferometers such as that shown here will produce, at a photodetector, an interferogram that is the summation of the the interferograms of all the constituent interferometers. Each of these interferograms contains information about the intensity and phase of the light passing through them. RRI allows the investigation of each of the constituent interferometers to extract this information.

1.4 THESIS AIMS AND NOVELTY

The aim of the work presented in this thesis was to combine, for the first time, the principles of RRI with those of TDLS to produce a new method for detecting gas concentrations in multiple locations simultaneously. This was broken down into the following specific objectives.

- Investigate the ability of RRI to show the presence of methane in a single location by combining the RRI measurements with spectral information provided by sweeping the laser's central emission wavelength across an absorption feature

- Determine if this method can be used to produce a measurement of methane concentration using a similar approach to TDLS

- Establish whether RRI can perform this measurement of methane concentration in multiple locations simultaneously and independently

- Investigate methods to extend the capability of the RRI gas sensing system to perform this measurement in real-time

- Characterise the limits of detection of the system built to perform these tasks

To date, RRI has been used to extract phase information and thus positional information from multiple interferometers[26]. This thesis describes the first use of RRI to measure the change in light intensity within individual interferometers as a function of time. It is also the first time that RRI has been described in use in conjunction with a ramped modulation to extract spectral information from sensing regions. Finally, this is the first time that RRI has been used to measure the presence of gases.

1.5   THESIS ORGANISATION

The first part of this thesis reviews prior work that forms the background for the novel experimental work

- Chapter 2 This chapter outlines prior work on gas sensor technologies, summarising their modes of operation and their advantages and disadvantages. Particular attention is paid to TDLS as it is the basis of the gas sensing technique used in this thesis.

- Chapter 3 This chapter describes some techniques that have been used to address multiple sensing regions using multiplexed sensors.

- Chapter 4 This chapter introduces and explains the concept of Range Resolved Interferometry and details the process by which the light intensity in each sensing region can be extracted from a superposition of multiple interferometers

The second part of the thesis describes the practical work to realise the sensor and measure its capabilities

- Chapter 5 This details the work to develop the first instance of a sensing system that measures methane concentration at multiple locations using RRI.

- Chapter 6 This chapter expands on the work in the previous chapter and shows the further development required to make a sensing system that was capable of operating in real-time. It also discusses the effects of different sensor topologies on the effectiveness of the gas sensing system.

- Chapter 7 This final chapter describes two additional experiments, one done to measure the effect of the laser modulation on the gas sensing potential of the RRI system, and one to test the capabilities of using RRI to combat unwanted optical interference fringes that are a problem in conventional TDLS measurement systems.

- Chapter 8 This summarises the work presented in the thesis and discusses potential avenues of research that the use of RRI would enable and the work that can be done to improve the system's capabilities.

A list of outcomes such as papers, conference presentations, patents and prizes, achieved to date is also provided.

AN OVERVIEW OF GAS DETECTION TECHNIQUES

2.1 GAS DETECTION

The need for gas detection runs across a wide range of fields including health monitoring, explosive detection, to vehicle performance monitoring. For example, the ability to detect acetone present in a patient's breath is an important, non invasive method for the investigation of possible diabetes in a patient[1]. The ability to detect the presence and concentrations of gases is also part of environmental monitoring. A localised example of this is the need to detect the presence of toxic, potentially carcinogenic formaldehyde gas that can be present in both residential and environmental environments[10]. On a global scale, the emission of carbon containing greenhouse gases is causing climate change with effects such as rising levels, ocean acidification and a rise in planetary temperatures likely to be over 1.5°C by the end of the 21st Century (compared to 1850-1900). While the greenhouse gas carbon dioxide (CO_2) is found at a higher concentration in the atmosphere than methane (at the time of writing, September 2020, carbon dioxide is found in the atmosphere at concentrations of around 400ppm, while methane is found at concentrations of 1.9ppm[27]), methane is a more potent greenhouse gas, with a warming potential of 34 times greater than CO_2 measured over 100 years, and 36 up to 86 greater over the period of time in which it remains in the atmosphere[28]. Methane enters the atmosphere as a result of man-made processes such as landfill and waste treatement[29]. Methane is also the main component of natural gas, and emissions from the upstream oil and gas facilities are considered to be some of the most significant and also

most immediately actionable[30]. In order to reduce industrial impact on the climate, it is vital for the emissions of methane to be reduced, in particular from the energy industry[31]. Part of any process to reduce emissions will require methodologies to detect the amount of methane present, and so methane sensors are a vital part of any such strategy. As well as an environmental hazard, methane gas is explosive and so forms a hazard to equipment and human life. 70% of accidents that occurred on offshore oil and natural gas extraction platforms were judged to be associated with the accidental release of flammable gas which usually includes the presence of methane[12]. Methane will sustain an explosion when mixed with air in concentrations between 5% and 15% (50000ppm and 150000ppm) [13]. These concentrations are, respectively, the lower explosive limit and upper explosive limit of methane. To prevent explosions, systems need to be able to detect gas in appropriate concentration ranges[14] so that alarms can be triggered and appropriate action, such as evacuation, or pipeline shutoff can occur. This thesis will describe the development and testing of a methane sensing instrument that is proposed for use in such a safety monitoring role, but that could potentially be improved for use in other fields such as environmental measurement. These two measurement regimes require different sensor capabilities, some of which are discussed in the next section.

2.2 PROPERTIES OF GAS SENSORS

There are a wide range of gas sensors that are used in a wide variety of use cases, some of which were described above. They all have different performance characteristics, some of which are summarised below (after Chaulya and Prasad[32])

- Sensitivity: The ability of a sensor to measure small changes in a gas concentration (measured in % or parts per million (ppm))

- Selectivity: The ability of a sensor to respond to one gas in particular rather than others that may be present

- Limit of Detection (LOD): The lowest concentration of gas that the sensor can detect (% or ppm)

- Dynamic Range: The range between the lowest and highest concentrations that a sensor can respond to

- Linearity: The degree to which a calibrated response of the sensor is proportional to the gas concentration (% or ppm)

- Life Cycle: The period of time over which a sensor can be used before it must be repaired or replaced.

To be of use in explosion prevention and safety applications, the system needs to be able to detect methane at a level of 20% of the lower explosive limit of methane (that is approximately 10000ppm), as this is a standard point at which action needs to be taken[33]. This, therefore defines the limit of detection that any sensor working in this region will require. In addition, there are likely to be other hydrocarbon gases and volatile organic compounds (VOCs) present in any location in which methane is present[34] and so the sensor will need to be able to respond selectively to methane. Furthermore, in order to be of use in safety critical operations, the response of the system needs to be fast enough to allow action to be taken. This response time is measured by the time it takes for the sensor to read 90% of the actual methane concentration present, and must be faster than 10 seconds[35]. A related problem is that of the variable composition of natural gas, meaning that a measure of methane alone is not sufficient for safety critical work. This problem can be ameliorated by the simultaneous measurement of another component of natural gas, ethane[36]. A number of technologies have been developed previously to allow the measurement of gases, some of which are already in use in the field of safety monitoring in offshore oil and gas ex-

traction operations. The next sections discuss a few of these technologies and their suitability for application to the needs of safety monitoring in oil and gas extraction environments.

2.3   NON OPTICAL GAS DETECTION TECHNIQUES

While this thesis describes the development and testing of an optical gas sensor, many industrial and environmental gas monitoring systems are based on non optical techniques and so some of these are described below, so that the proposed technique can be placed in a wider context of available gas sensing technologies which form a major part of the market into which it would be placed.

2.3.1   *Flame Ionisation Detector*

When burned in the presence of Hydrogen many organic compounds including methane, produce ionised fragments. A flame ionisation detector (FID) uses this principle as follows and as shown below in Figure 2.1. A collected sample of the gas under test is burnt in the presence of hydrogen gas, producing ions[37]. An electric field is present in the sensor due to the electrodes and the positive ions are attracted to the negative electrode, which causes the flow of a current which can then be detected. The current is proportional to the rate of ions being produced in the flame, which in turn is proportional to the number of carbon atoms in the sample, with the FID effectively acting as a "carbon counter"[38].
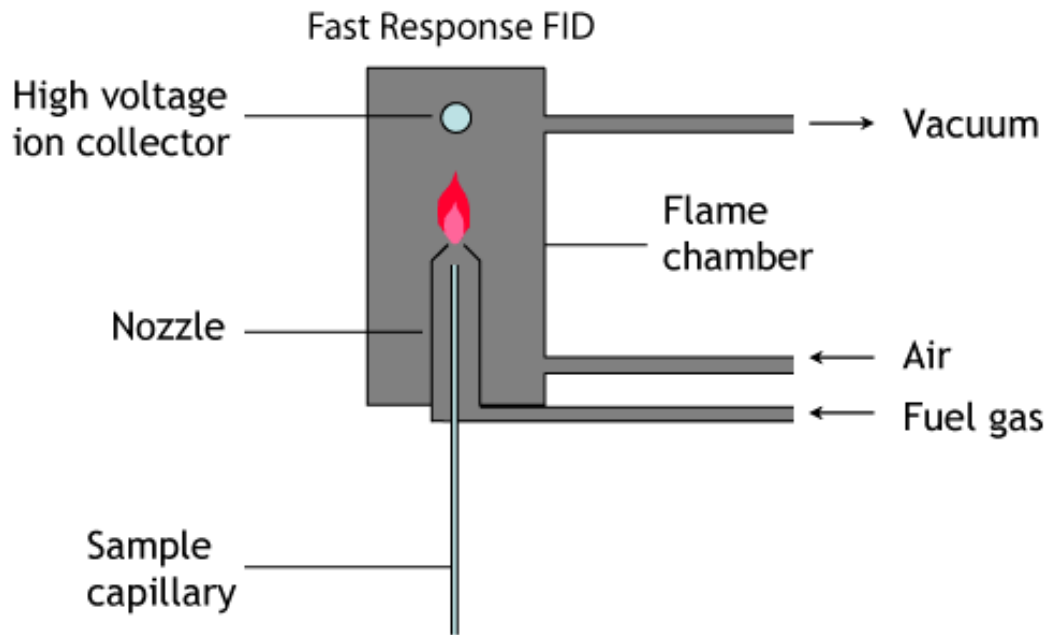
Figure 2.1: A Flame Ionisation Sensor, taken from Cambustion[39]

FIDs have a wide operating range of detection [32] with the ability to measure between 1-50000ppm[40]and they respond to all alkanes, making them useful across a wide range of applications from health [41] to mine safety [32]. However, the method of detection does not allow the identification of specific gases, merely the total amount of carbon atoms present in a sample. Detailed gas identification would be achieved using mass spectroscopy[42]. In addition, the presence of an open flame makes this methodology unsuitable for use in explosive or flammable locations which make up a major part of the use case proposed for the technology described in this thesis unless much more complex and expensive explosion proof systems are used[43]

2.3.2 *Electrochemical Sensors*

An electrochemical sensor works via the oxidation or reduction of an electrode and the consequent formation of charged particles. A typical schematic of an example of such a device is shown in Figure 2.2. The gas under test passes through a porous membrane and reacts with the counter electrode, causing the creation

of the charged particles which are then free to cross the liquid electrolyte to the working electrode which is held at an appropriate electric potential. This causes a current flow that can be measured and is proportional to the concentration of the gas under test.[44, 45].
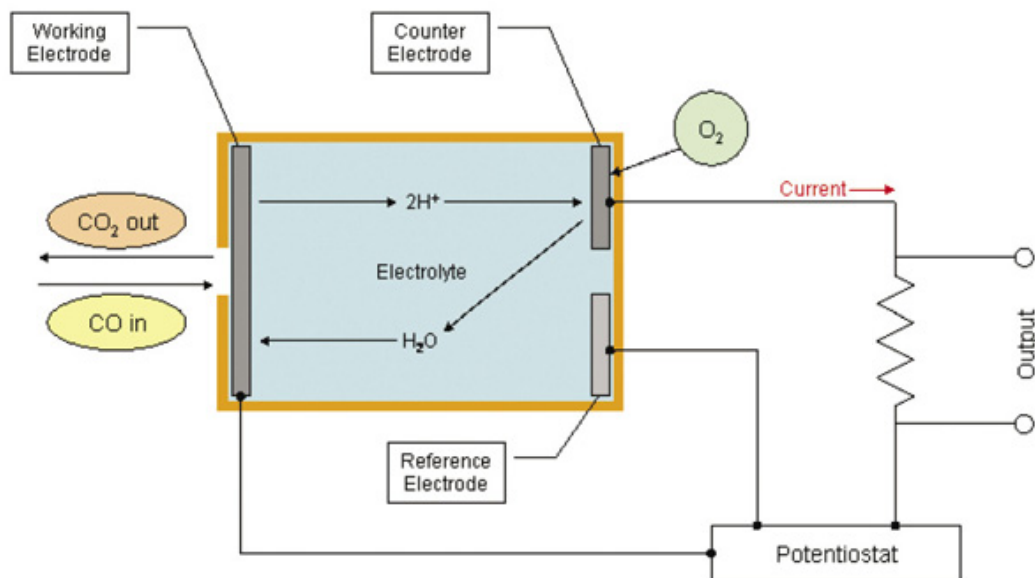
Figure 2.2: Schematic diagram of the working of an electrochemical carbon dioxide sensor taken from [46]

Electrochemical gas sensors are small in size and require little power to run while offering good linearity of response. Electrochemical sensors have the ability to detect some gas species at levels in the region of 0.1ppm [47]. However, they suffer from problems of low lifespan due to leakage or use of the electrolyte over time[48], and they have a tendency to deteriorate in performance quality in the presence of water vapour[49] as well as suffering from interferences from other gases including hydrogen[50] To date, only one electrochemical sensor detecting methane has been developed[51] and none have been commercialised.

2.3.3 *Metal Oxide Detectors*

These sensors consist of a thin layer of a metal oxide placed between two electrodes as shown in Figure 2.3. In the absence of a combustible, reducing target gas, electrons within the oxide are attracted to oxygen which adsorbs to the oxide surface. These electrons are thus fixed in place and not available for electrical conduction. In the presence of the target gas, the atmospheric oxygen reacts with the gas and is thus unable to retard electron mobility and so a current can flow, the amplitude of which can be used to determine the concentration of the gas present[52].
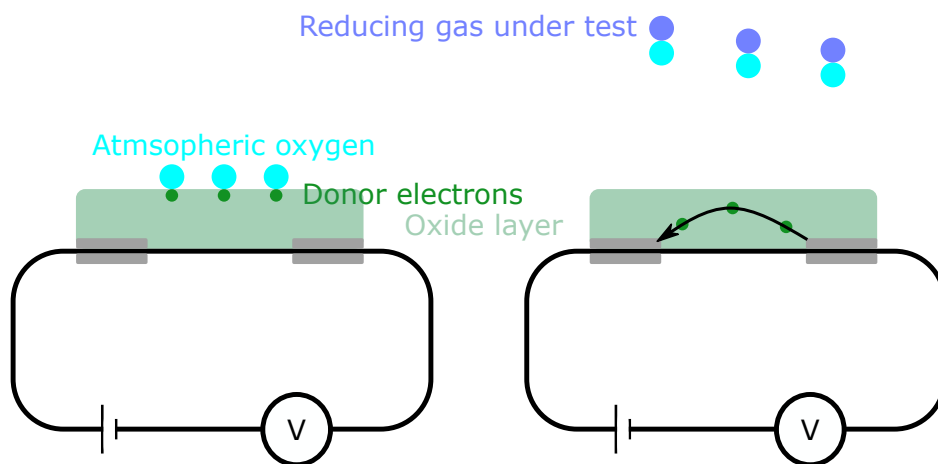
Figure 2.3: Schematic diagram of the workings of a metal oxide detector showing the fixed nature of the electrons within the oxide layer when no reducing gas is present compared to their freedom to produce current in the presence of such a gas

Due to the relative simplicity of their design, these sensors can be physically robust, and they are able to detect methane at single digit ppm concentrations[53, 54, 55]. However, they suffer from a low selectivity in gas species detection, as multiple gases can react with the atmospheric oxygen, and similarly, they are prone to influence from temperature and humidity fluctuations[56].

2.3.4   *ElectroAcoustic Sensing*

Electroacoustic devices operate on the principle that the resonant frequency of an object is determined in part by its mass. A device is set to oscillate by way of an exciting signal. The device is coated with chemicals to which the target gas can selectively adsorb. For example, one such device uses supramolecular kriptophan A, as a methane binding chemical[18]. The adsorption of the methane to the device alters its mass causing a change in the resonant frequency of the system that is then detected and converted into a measure of the amount of gas present[57]. Electroacoustic sensors can be designed to detect the effect of gas adsorption on bulk acoustic properties or surface wave propagation using the same fundamental process. Devices that operate using the bulk acoustic properties are referred to as quartz crystal microbalance (QCM). QCM devices not have a wide enough range of operation for safety critical methane detection as their sensing ability becomes saturated at around 0.2% (2000ppm) concentrations of methane[18] which is too far below the lower explosive limit of methane. Systems that work by measuring surface waves have been developed that can measure concentrations of methane of around 0.5% (5000ppm) which would make them operable in the region of methane concentrations required for gas detection. However, these systems are susceptible to drift caused by humidity and temperature[58].

2.3.5   *Pellistor Devices*

Widely used in safety applications, including in offshore oil and natural gas extraction, a pellistor or catalytic sensor operates by measuring the heat produced by the oxidation of combustible gases. A typical pellistor system is shown below in Figure 2.4

Porous refractory bead
containing catalytic particles

Platinum wire
heater

1mm
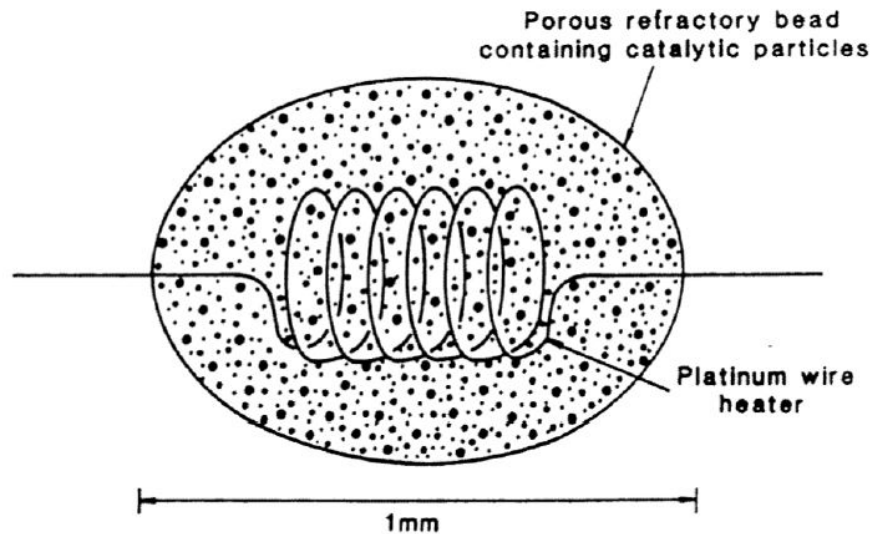
Figure 2.4: A pellistor sensor, taken from Moseley[59]

The pellistor bead itself is a coil of thin aluminium wire encased in a porous substance such as alumina or palladium which is coated in a catalyst that encourages the oxidation of the combustible gas[53]. Electricity is passed through the coil, raising the temperature to the combustion temperature of the hydrocarbons (approx 500°C) and the combustion of the gases further increases the temperature. This in turn further increases the temperature of the coil and so decreases its resistance. This change in resistance can be compared, via a Wheatstone Bridge, to the resistance of a similar pellistor that has not been coated with the catalytic substance so whose resistance remains unchanged by the presence and oxidisation of the gas under test[59]. The difference between these resistances is linearly proportional to the gas concentration. Pellistor sensors are simple, well proven technology, but they suffer from at least three significant drawbacks. Firstly, they offer low sensitivity with a high limit of detection of around low parts per thousand by volume[56]. Secondly, they can be rendered contaminated by the presence of chemicals such as sulphur compounds or heavy metals, resulting in the presence of an inert layer on the reactive pellistor preventing the efficient combustion of the gas. Finally, their mode of operation means

that the presence of any combustible gas will be detected as it oxidises meaning that they lack selectivity[59].

2.3.6   *Summary of Non Optical Gas Sensing*

It would be useful to summarise the findings here. Each of the methodologies described uses a different principle of operation to detect the presence of methane and consequently has different advantages and disadvantages as well as different performance characteristics. These are summarised below in Table 2.1

Table 2.1: Summary of some selected non optical gas detection methodologies

Method	Principle of operation	Advantages	Disadvantages	Selected performance characteristics
Flame Ionisation[38]	Gas is ionised by combustion and current caused by ions is detected	Wide concentration range of operation. Wide range of gas species can be detected	No gas specificity. Not suitable for explosive environment	Linear range of 6 orders of magnitude. Picogram measuring capabilities
Electrochemical[47]	Gas interacts with electrode causing ionisation and thus current	Good linearity of response	Not available to detect methane at present	Limit of detection of 0.1ppm for some gases
Metal Oxide[53]	Gas interacts with atmospheric oxygen, changing the conductivity of a metal oxide	Robust design, low limits of detection	Limited gas specificity Poor stability over time	Limit of detection <10ppm methane
Electroacoustic[57]	Adsorption of gas alters resonant frequency of a vibration sensor	High sensitivity	Response can saturate at relatively low methane concentrations	Saturates at 2000ppm
Pellistor[56]	Combustion of gas changes temperature and resitance of platinum coil	Simple, well proven technology	Low Sensitivity Can be degraded No gas specificity	Limit of detection 250-500ppm Response time 20-30s

As discussed above, the non optical methods of gas detection have multiple drawbacks such as limited gas specificity or being inappropriate for use in explosive environments. By using the properties of light and the nature of its interactions with gases, devices can be designed that improve upon the non-optical techniques.

2.4.1   *Interactions Between Light And Matter*

Previously, in Section 2.3 non optical methods for gas detection were discussed, and in the following section, some optical methods will be introduced. First, however, it is necessary to discuss the interactions between light and matter that make optical gas detection possible.

When a gas molecule is illuminated by a photon, there is the potential for the molecule to absorb the photon's energy. A gas molecule has a set number of allowed states in terms of orientation, configuration and electron distribution. The transitions between these states, with energy levels E_1 and E_2 respctively, releases or absorbs energy in quantised forms such that the frequency of light released or absorbed obeys the Bohr condition as in Equation 2.1[60]

$$\nu = \left| \frac{E_1 - E_2}{h} \right| \tag{2.1}$$

These transitions can take the form of a change in the molecules physical orientation, a change in the relative physical positions of atoms within the molecule, or a change in the distribution of electrons within the atoms of the molecule. If a photon of light incident upon a molecule of gas has the quantity of energy associated with the transition from a lower to a higher energy state, then it may be absorbed causing the molecule to undergo that transition. Figure 2.5 shows

some examples of the transitions possible in a hypothetical two-atom molecule along with the characteristics of the photons whose absorption would induce such a transition.
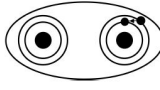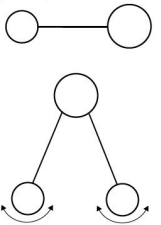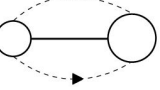
X-ray 100pm - 10nm	Visible and UV 10nm - 1μm	Infra-red 1μm - 100μm	Microwave 100μm - 1cm
Change of electron configuration		Change of configuration	Change of orientation

Figure 2.5: The possible electron transitions caused by varying energies of light absorption adapted from[61]

As the energy of a photon depends on its wavelength, this process means that photons of certain wavelengths (or colours) will be absorbed by certain gas species. Thus, light that passes through a gas will have a lower intensity if it is a wavelength absorbed in the process of one of these transitions. As a result, a spectrum of light passed through a gas will display regions of relative darkness at these transition wavelengths. Databases such as HI-TRAN have been created detailing these transitions and the strength of the absorption[62]. For example, in methane CH_4, upon absorption of a 3.3 μm photon, the molecule undergoes a transition in which the C-H bonds are stretched. Thus, methane absorbs light at the wavelength of 3.3μm and also at the harmonics of this absorption including the first harmonic at 1.65 μm In the paragraphs above, it was suggested that light was absorbed in perfectly discrete wavelengths which would lead to perfectly discrete absorption lines in an absorption spectrum, this is not actually the case. Three factors combine to broaden the wavelength range of absorption and so produce a finite width to the absorption feature.

Once raised to a higher energy level by the absorption of a photon the molecule will eventually decay down to the ground state in such a way that after a period

τ half of the excited atoms will have decayed to their lower energy, ground state, undergoing a change in energy states of ΔE ($E_1 - E_2$ in Equation 2.1). The Heisenberg Uncertainty Principle, as shown in Equation 2.2, when combined with Equation 2.1 (and assuming that $\Delta t = \tau$), produces a value for the uncertainty in the absorption frequency as shown in Equation 2.5 where $\hbar$ is the Planck constant.

$$\Delta E \Delta t \geqslant \hbar \tag{2.2}$$

$$\Delta \nu h \tau \geqslant \hbar \tag{2.3}$$

$$\Delta \nu \geqslant \frac{\hbar}{h\tau} \tag{2.4}$$

$$\Delta \nu \geqslant \frac{1}{2\pi\tau} \tag{2.5}$$

Equation 2.5 describes a process called natural broadening which provides the minimum possible width of an absorption feature, but under most experimental regimes, the quantum effects are negligible. Isolated molecules will experience natural broadening of their line shapes, but in the presence of other molecules, they will undergo collisions. These collisions shorten the half life (τ) of the excited state of the molecule. By way of Equation 2.5, this decrease in the half life of the excited state leads to an increase in the uncertainty of the absorption frequency and so a broadening of the absorption feature. This process depends on the number density of possible collision partners and is therefore referred to as pressure broadening. It produces a Lorentzian line shape of the absorption feature[60]. Natural and pressure broadening of a line shape affects all the atoms in a sample homogenously but a third cause of line broadening acts inhomogeneously through a sample. Just as the Doppler effect means a moving observer experiences a sound wave of fixed frequency as being at a higher or

lower frequency than a stationary observer does, so a molecule under motion will experience incoming photons differently depending on the molecule's motion relative to the source of the illumination. Thus, when an atom is travelling towards a detector at a velocity v then the observed transition frequency (v_a) will be related to the actual transition frequency in a stationary atom (v) by way of Equation 2.6[20]

$$v_a = v \left(1 - \frac{v_a}{c} \right)$$ (2.6)

As a result, the observed frequencies of absorbed photons will depend on the velocity of the molecules within the gas sample. The Maxwell-Boltzman distribution of these velocities is such that the broadening of the line shape is proportional to the square root of the absolute temperature of the gas, and produces a Gaussian form of the line shape. This process is called Doppler broadening Pressure broadening and Doppler combine within a sample in ratios depending on the temperature and pressure of the gas. Thus the absorption line shape will be a convolution of Lorentzian and Gaussian, forming a Voigt curve an example of which is shown below in Figure 2.6. The physical reason for the width of the Voigt curve being greater than that of the Lorentzian and the Gaussian is that the Voigt describes the absorption feature when all possible broadening mechanisms are occurring, rather than a small subset as for each of the other broadened line shapes.
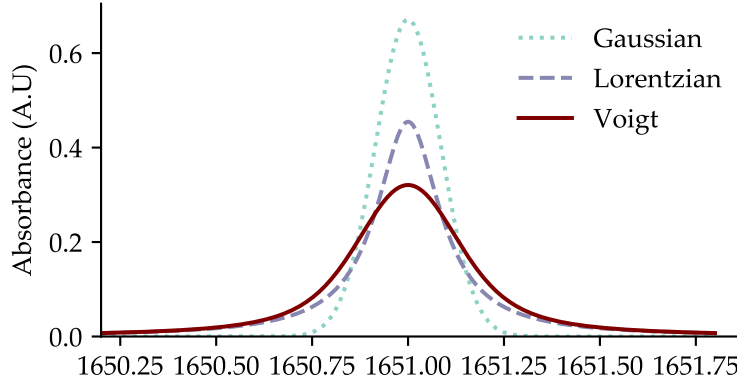
Figure 2.6: Showing the Voigt curve formed from the convolution of the Doppler broadening (Gaussian) and the pressure broadening (Lorentzian)

In the regime that the relevant to this thesis, namely atmospheric pressures and temperatures, the gas absorption lines are most affected by pressure broadening, and so the Voigt curve is mostly Lorentzian in shape, and indeed, is modelled in this work as a Lorentzian curve. Quantitatively the measured intensity of light at a particular wavelength (I_λ) that has passed through a gas for a distance in metres (L) (referred to as the interaction length) is related to the initial intensity of the light at that wavelength (I_{0_λ}) by the Beer-Lambert Law[63] (Equation 2.7).

$$I_\lambda = I_{0_\lambda} e^{-\alpha_\lambda CL} \qquad (2.7)$$

In Equation 2.7, C is the concentration of gas present in ppm, while α is a specific absorption coefficient at the wavelength λ in units of m^{-1}ppm^{-1}. The difference between the incident intensity and the transmitted intensity at each wavelength ($I_\lambda - I_{0_\lambda}$) is the absorbance of the gas sample, which normalised against the incident intensity I, produces

$$\frac{I_{0_\lambda} - I_\lambda}{I_{0_\lambda}} = 1 - e^{-\alpha_\lambda CL} = \frac{\Delta I_\lambda}{I_{0_\lambda}} \qquad (2.8)$$

At low concentrations (C) and short interaction lengths (L) the value of $1 - e^{-\alpha_V CL}$ can be approximated as $\alpha_V CL$. So under these conditions of low concen-

trations and short interaction lengths, a linear relationship between normalised absorption (A) and gas concentration (C) can be derived as in Equation 2.9.

$$A = \frac{I_{0_\lambda} - I_\lambda}{I_{0_\lambda}} \approx \alpha_{(\lambda)}CL \qquad (2.9)$$

The normalised absorbance is a unitless value, but is usually referred to in Absorption Units or AU. Values of the absorption coefficient for various gases at various wavelengths of light ($\alpha_{(\lambda)}$) have been experimentally measured and are available from databases such as HI-TRAN[62]. Thus, measuring the incident, and transmitted intensity of light of a known frequency through a known interaction length of gas allows the calculation of the concentration of that gas, while knowing the wavelength being absorbed allows, with a high degree of specificity, knowledge of the gas species being measured.

2.4.2 *Tunable Diode Laser Spectroscopy*

Initially developed in the 1970s [64, 65], tunable diode laser spectroscopy (TDLS) utilises the absorption of light by chemical species as described in section Section 2.4.1. By adjusting the injection current of a diode laser, the emitted wavelength can be controlled. Thus, ramping the injection current allows the laser wavelength to scan across one or a small number of gas absorption features that were described in Section 2.4.1[66]. When the light is passed through a sample of gas, and the resultant transmission will show a rising function (due to the fact that increasing the injection current also increases the output intensity of the laser) and a dip caused by the absorbance of light as the laser wavelength passes through the gas absorption feature. See Figure 2.7 for an illustration.

Using the intensity of the incident and transmitted light in Equation 2.8 or Equation 2.9, a value for the concentration of the gas under test can be obtained. In order to establish a value for the incident intensity over the whole wavelength

scan, the values during when the output wavelength is outside an absorbance feature can be extrapolated as in Figure 2.7.
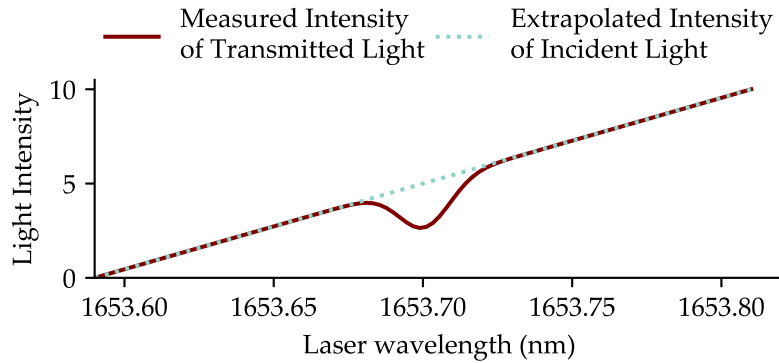
Figure 2.7: A simulated measurement of the intensity of light measured after passing through a sample of methane (I). An absorption feature is shown at 1653.7nm. Also shown is an extrapolated value of the intensity in the absence of the absorption feature (I_0)

The extrapolated value for I_0 and the measured value I can then be used to calculate a normalised absorption at each wavelength along the ramp modulation. This normalised absorption is unitless but is usually expressed in Absorbance Units (AU) can be plotted against the laser wavelength as shown Figure 2.8.
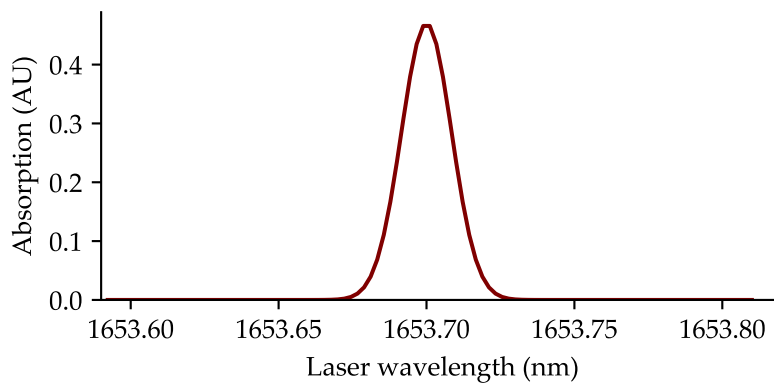
Figure 2.8: A plot of the normalised, Lorentzian, absorption ((I_0-I)/I_0) using the simulated data presented in Figure 2.7

The plot in Figure 2.8 is analogous to the plot in Figure 2.6 and consequently will show the effect of the various broadening processes discussed in Section 2.4.1.

Under most conditions experienced (standard temperatures and pressures) in the regimes relevant to this project, the curve can be fitted to a Lorentzian line-shape using algorithms such as the Levenberg Marquardt algorithm[67]. When this is done, various properties of the curve can be extracted such as the wavelength of the peak of absorption, the peak height of the absorption curve (h), the line width of the curve defined as the full-width half-maximum (FWHM) and the integrated area under the curve. It is the final value, the area under the curve that is strictly proportional to the number density of gas molecules in the sample, and this can be calculated from the FWHM and the height of the curve.

Modern diode lasers have narrow linewidths (2Mhz for the laser used for the work described in this thesis[68]) compared to the width of gas features (In the order of several GHz)[69, 21] and so, as their wavelength is scanned, they can produce a high resolution measure of absorption as a function of wavelength. In association with known absorption coefficients of gases at specific wavelengths, this allows high specificity of gas identification[19]. The ability to scan the output wavelength of a laser across multiple absorption features also allows the measurements of more than one gas species at a time. The limit of detection of a TDLS system is determined by the uncertainties in the values of I_o and I in Equation 2.9 which combine to produce a minimum height of A in the same equation that can be detected.

2.4.2.1 *Optical Fringes*

A major issue in the performance of TDLS is the existence of optical interference fringes on the signal[70]. These are caused by the interference of light reflected from various partially reflective surfaces in the path of the laser beam. These surfaces set up etalons and the interference is manifested as wavelength-dependent variation in the intensity of light passing through the system as shown below in Figure 2.9. These fringes sit upon the signal, and thus limit the ability of the sys-

tem to differentiate between them and the absorption caused by the gas under test[71].
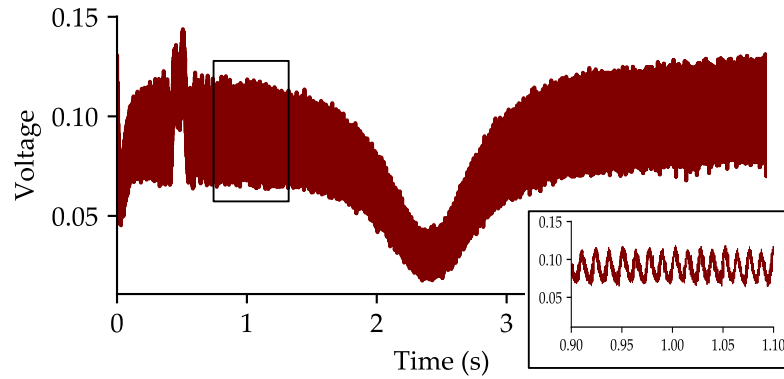
Figure 2.9: An example of a TDLS signal with optical fringing. The zoomed in section shows the sinusoidal nature of the fringing, making it distinguishable from random noise.

The problem is particularly apparent when the etalons cause fringes with a free spectral range (FSR) similar to the width of the gas absorption line being detected. The partially reflective surfaces that give rise to the system can take a number of forms, such as the windows of the gas cells[70] or even dust[72]. Techniques such as adjusting the angles of any reflecting surfaces and the use of anti-reflective coatings[73], can be used to reduce the amplitude of the fringes, but they cannot be completely removed and, due to the presence of temperature fluctuations and vibrations altering their position, they cannot be simply subtracted away from the signal. Apart from physically removing the reflections or directing them such that interference cannot occur, the signal can be dithered (that is to say a sinusoidal modulation can be added) at a high frequency and the signal integrated[74]. In post-processing, the signal can be filtered[73, 75], or be processed using Fourier analysis and arithmetic removal of the interference fringes[76].

2.4.2.2 *Wavelength Modulation Spectroscopy*

While TDLS uses only a simple ramped modulation of the laser current (and thus wavelength), a related technique, Wavelength Modulation Spectroscopy (WMS) adds a rapidly changing sinusoidal modulation to the ramp[77]. This sinusoidal modulation is a much higher frequency (often of the order of kHz to low MHz) than the ramp modulation, and a lower frequency than the gas line (often of the order of 4GHz)[78]. The ratio between the amplitude of this sinusoidal modulation and the width of the gas line is referred to as the modulation index. A typical arrangement for WMS is shown below in Figure 2.10
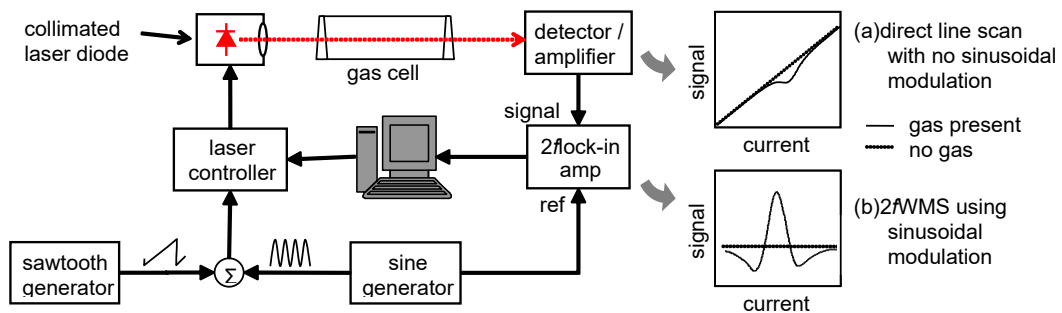
Figure 2.10: A typical layout for wavelength modulation spectroscopy. Taken from[19]

This additional modulation allows the extraction, using a lock-in amplifier, of the derivatives of the absorption feature in the form of the harmonics of the output voltage of the light detector. Figure 2.11 shows these harmonics as the laser's central output wavelength is ramped across a gas feature
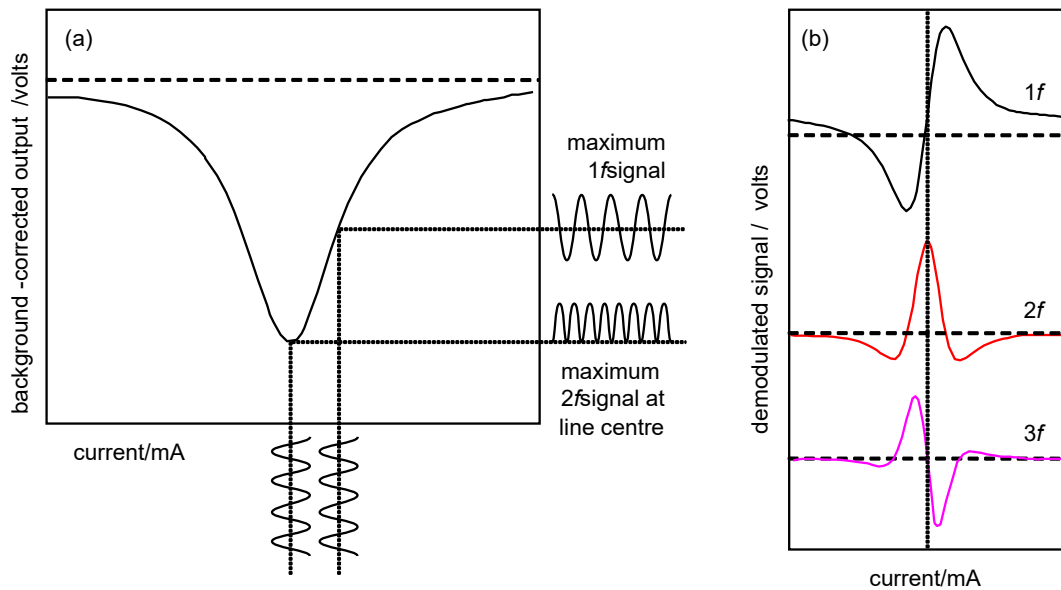
Figure 2.11: The measured values of the different harmonics produced y WMS

Using the second harmonic measurement for gas detection reduces the effect of laser power on the baseline of the measurement (although such an effect does still exist), while the first and third harmonics can be used for signal processing techniques[79]. Measurement of a modulated signal at the 2nd harmonic (2f) moves the signal to higher frequencies, at which laser noise, as well as background environmental fluctuations are smaller[19]. This means that WMS can typically be an order of magnitude more sensitive than direct absorption spectroscopy[80][81] with methane detection being achieved at 0.4ppb[82] using a variant of WMS.

2.4.3   *Photoacoustic Spectroscopy*

First investigated by Alexander Graham Bell in 1880[83], this methodology depends on the fact that when light interacts with gas, as described in Section 2.4.1, there is mechanical work being done on the molecules, causing a change in the temperature of the gas, with the vibrational energy being translated to the kinetic energy of the gas molecule. Therefore, if the light is periodically interrupted

(chopped) then the temperature of the gas will periodically change causing pressure fluctuations[84]. These fluctuations can then be detected by a microphone. Given a known incident light frequency and the absorption coefficient of the gas under test, the gas concentration can be determined[85] by measurement of the intensity of the output acoustic waves. Devices built on these principles have the following advantages: They are relatively immune to noise in the transmitted light intensity since their signal is proportional to the absorbed light[86]. They have a large dynamic range and have achieved limits of detection for methane of 1.7ppm[87]. However, they are sensitive to environmental vibrational noise[88] as well as the presence of water vapour, which leads to a reduced signal for a given concentration of gas[89].

2.4.4 *Non Dispersive Infra Red Detection*

Like TDLS, as described in Section 2.4.2, non dispersive infra red (NDIR) systems work on the principle that gases are selectively transparent at different wavelengths of light[90]. Rather than use a narrow band laser light source that is scanned across a range of output wavelengths which includes a gas absorption feature, NDIR uses a broadband source to illuminate a gas sample. The light then passes through a pair of filters, one of which allows the passage of light in a wavelength region absorbed by the gas under test and one which allows the passage of light in a wavelength region that is not absorbed by the gas. Using a pair of light sensors, a comparison can be then made between the intensity of light that illuminates the sample and the intensity of light that is absorbed by the gas and so a value for the gas concentration can be obtained. A diagram of a typical NDIR sensor is shown in Figure 2.12
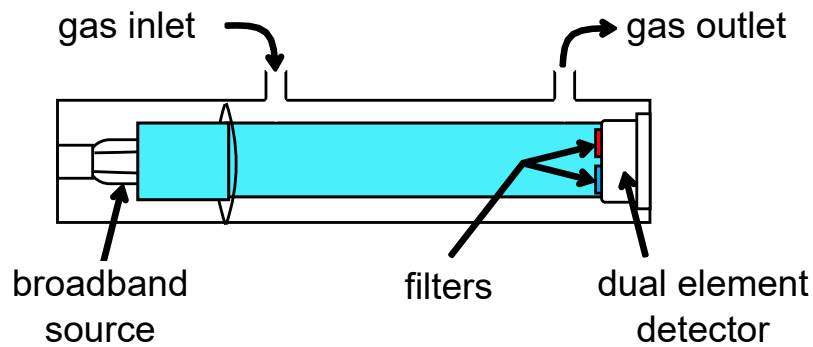
Figure 2.12: A schematic diagram of an NDIR gas concentration sensor taken from[19]

Due to the simplicity of their design, NDIR sensors are compact, lightweight and cheap in comparison to TDLS systems, with an industry standard model being entirely contained with a cylinder of 200mm diameter and 16mm height[19]. However, they suffer in comparison to TDLS systems as the use of relatively broadband light sources and filters means they lack gas specificity. Light sources and sensors in their construction are also prone to drift, meaning they need to be periodically recalibrated[90]. In addition, as there are two combinations of sensors and filters, anything that blocks the transmittance of light through one of them, such as environmental dust, will lead to an incorrect ratio of light intensity measured by the sensors and so an incorrect gas concentration reading. This is in contrast to a TDLS system which uses a single sensor and is self referencing over a number of measurements. The limit of detection for an NDIR system is governed by the minimal measurable difference in light intensity between the two channels, and systems have been developed with sensitivities to methane concentrations in the ppm range[91, 92] while a readily available model is available that has a limit of detection of 500ppm[93], well within the required sensing region of a methane safety regime as discussed in Section 2.1, and a suitable example against which the system described in this thesis can be compared.

2.4.5 *Dispersion Spectroscopy*

As well as attenuating the intensity of light passing through, interactions between light and a gas have an effect on the phase of the transmitted light. This is due to the fact that the refractive index of a gas is dependent on the wavelength of light passing through the gas[94]. The refractive index is related to the absorption coefficient as used in the Beer-Lambert Law by way of the Kramers Kronig relations[95]. In Chirped Laser Dispersion Spectroscopy (CLaDS), as in TDLS, a laser is modulated so its output wavelength sweeps (chirps) across a gas absorption feature using an acousto-optic modulator[96]. The laser output is then split into two beams, one of which is wavelength shifted. The beams are then recombined and passed through a sample of gas and due to the fact that they are spectrally shifted from one another, effectively experiencing different refractive indices of the gas, causing a phase difference between them.

The signal created at the detector by combined beams is then frequency demodulated to produce a signal the amplitude of which is proportional to the ramp (chirp) frequency and the concentration of gas present. As it is based on the phase of the light rather than the intensity, a CLaDS system produces signals that are immune to signal intensity fluctuations. And the dispersion effect of a gas sample is linear with respect to concentration which is an advantage in long interaction lengths, unlike the absorption effect which is described by the non linear Beer-Lambert law [97]. CLaDS systems have been shown to have the capability to measure methane at the sub 2ppm level and have been commercialised for use in methane leak detection[98]

2.4.6 *Summary of Optical Gas Sensing*

As with the non optical methods, a summary table of some important characteristics of the optical methods is shown in Table 2.2

Table 2.2: Summary of selected optical gas detection methodologies

Method	Principle of operation	Advantages	Disadvantages	Selected Performance Characteristics
Tunable Diode Laser Spectroscopy[99]	Laser wavelength is modulated and changes in transmission detected	Fast, high specificity	Lasers and detectors can be expensive	LODs of 20ppb
Wavelength Modulation Spectroscopy[82]	Laser is modulated with induced dither and harmonics of the transmission signal are detected	Allows greater sensitivity than TDLS	Extracting the harmonics requires additional signal processing and signal detection at higher bandwidths	0.4ppb LODs
Photoacoustic Spectroscopy[87]	Light absorption by gas is converted into mechanical work which is then detected	Large dynamic range	They are sensitive to environmental vibrations	LOD of 1.7ppm
NDIR[93]	The differential absorption of light that has been filtered to on and off absorption wavelengths is compared	Simple and cheap	Lower gas specificity Sensitivity to dirt	LOD 500ppm

In general, the optical techniques discussed here have better gas specificity than the non optical methods and have fast operation. However, this comes at a monetary cost, they are more expensive to implement than the most commonly used method of pellistor sensors. This cost will only expand if multiple sensors are needed.

2.5 CONCLUSION

This thesis will discuss the use of a system that, like TDLS, measures the intensity of light that passes through a gas sample, and uses that intensity as a measure of the absorption. This means it will have the advantages of TDLS, namely fast operation, sensitivity and gas specificity. However, as it will be a multiplexed system, using a single laser and detector to measure gas concentrations at a number of locations simultaneously, the cost per sensing region can be reduced. This concept of multiplexing sensors and measuring at multiple locations will be the focus of the next chapter.

MULTIPOINT OPTICAL GAS SENSING AND MEASUREMENT

3.1 INTRODUCTION

In the previous chapter, some technologies were discussed that allow the measurement of the presence and calculation of gas concentrations. Each of these technologies was discussed in the context of the measurement of gas at a single location, but in many situations, gas concentrations will need to be measured in multiple locations simultaneously. For example, on offshore platforms, it has been shown that a plume of hydrocarbon gases greater in size than 5m will produce pressures and flame speeds that are a danger to both equipment and operators on the platform [100]. As a consequence, good working practice is to place sensors no more than 5m apart on such a platform[14] enabling plumes to be detected before they reach this size[101]. Similarly, mines require the ability to detect poisonous or explosive gases in a number of locations at once[102]. The simplest solution to the need for multipoint gas detection is the deployment of a number of independent sensors, each of which is monitored individually. An example of a similar (although non gas sensing) system would be the individual smoke alarms that must be placed on each storey of rented accommodation[103]. However, the deployment of multiple gas sensors leads to an increase in cost in both equipment, and maintenance and calibration. If each gas sensor is a complex system in and of itself, this can lead to high degrees of complexity in the system overall, with multiple points of failure.

In this section, a selection of other methods that have been used to address the need for multiple regions of gas sensing are described to give an idea of the technological landscape into which Range Resolved Interferometry can be applied. In addition, the ways in which sensors are connected are introduced and some advantages and drawbacks of these are discussed to lay the foundations for work on the most suitable connection topology for a field-deployed RRI system

3.2   SPATIAL DIVISION OF MULTIPLEXING

One of the earliest means by which multiple optical gas sensors were connected using optical fibre was described by Stewart *et al.* [22]. In this work, the authors illuminated a number of micro-optic cells using light from a single laser that was divided using fibre splitters. Each of the sensing regions was illuminated by at most 1/n of the total light produced by the laser, where n is the number of sensing regions.
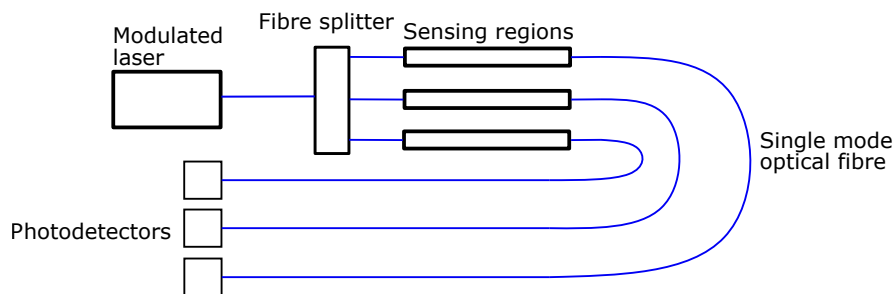
Figure 3.1: Spatial Multiplexing (After Stewart *et al.*[22]) All the sensing regions are illuminated by the light from a single source that has been split.

The light passing through each of the sensing regions is then detected by the photodiode associated with the sensing region. Depending on the modulation applied to the laser this can be used to perform either Tunable Diode Laser Spectroscopy[104] or Wavelength Modulation Spectroscopy[22, 105]as described in Chapter 2. As well as being used in fibre coupled systems, similar topologies of sensors have been used in free space applications, such as the monitoring of

the flames associated with combustion engines[106, 107]. While systems such as these do allow for the monitoring of multiple locations using a single laser, they still require a photodetector and signal acquisition systems for each of the sensing regions, which increases the complexity of the system and the number of possible points of failure. Each photodetector also adds to the cost of the system as a whole; Culshaw *et al.* suggested that multiplexed systems of over 60 sensing regions would be needed to make such a system cost effective against other, non optical, gas sensing techniques such as those described in Section 2.3[108]. However, changes in laser and photodetector prices since then will have lowered the number of sensing regions at which such systems are economical. It is also possible to apply spatial division multiplexing within a single, continuous light path by placing the sensing regions in series using photoacoustic sensing techniques, wherein each sensing is illuminated by the same pump laser and the photoacoustic effect in each region is separately measured[109, 110, 111]. In photoacoustic sensing, the signal used to measure the gas concentration is directly proportional to the intensity of the light illuminating the sensing region. In a system arranged in series, the intensity of light illuminating any sensing region will be affected by the light losses in the system prior to that sensing region. In particular, this will be a factor of the losses caused by coupling into and out of the sensing regions and by the absorption of light by gas in previous sensing regions. Wang *et al.* modelled the incident power on the final sensing region in systems with increasing numbers of sensing regions, and showed the drop in signal strength in each of three serially connected sensing regions[109]. A similar analysis is necessary for evaluating the design of a gas sensing system using the techniques outlined in this thesis and can be found in Chapter 6. In addition, serially connected systems suffer from the issue that the signal from downstream sensors is imprinted on the upstream signal, increasing measurement uncertainties as a result. The major limitation with regard to signal-to-noise and thus concentration in spatially divided TDLS systems are those found in any TDLS system, namely

the existence of interference fringes and sensitivities of a "few ppm" have been reported[22].

3.3   TIME DIVISION MULTIPLEXING

In a time division multiplexed system, the location of the measurement is calculated from the time at which the measurement is recorded. An example of such a system, using a forward-coupled ladder topology of sensing regions (labelled S_n), is shown below in Figure 3.2[112].
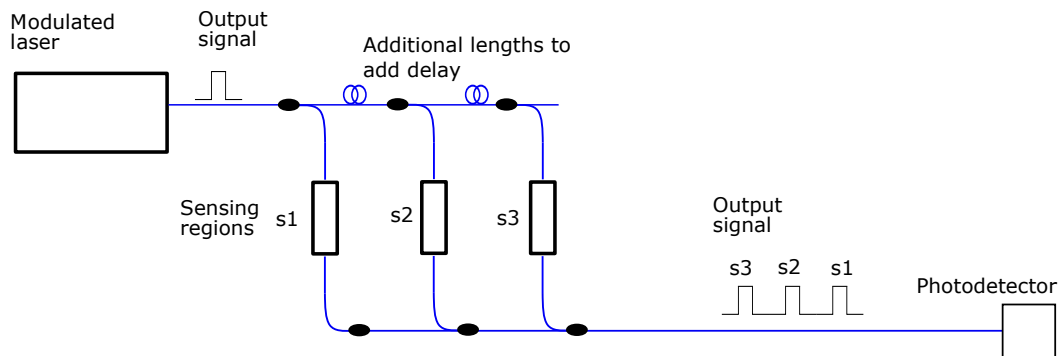
Figure 3.2: Time division multiplexing showing the illunination of multiple sensing regions from a single source and the use of delay fibres.

The laser is modulated to form a pulse and additional optical fibre lengths introduce a time delay between the signals. Fibre lengths of 60 m provide delay times of 300 ns per sensor, which means that pulses arrive at the photodiode 300 ns apart in the order determined by the length of delay fibre each pulse experienced. Timed switching separates the pulses after detection at the photodiode allowing them to be individually interrogated. Each pulse contains a WMS modulated ramp, meaning that it can be used to measure the gas concentration in the sensing region through which it passed. A system with three sensing regions was shown to have the capability to measure 81ppm concentrations of acetylene[113] and with cross talk sensitivities determined by the extinction ratio of the modulation technology used. Computer simulations of similarly linked systems of

sensors suggest that methane could be detected at 100ppm levels in 100 sensing regions[114].

3.3.1 *Photothermal Optical Time Domain Reflectometry*
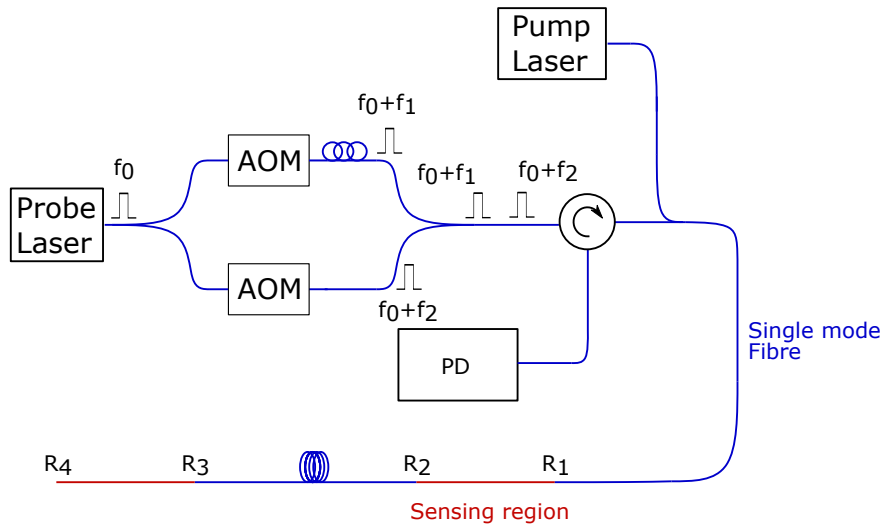
Figure 3.3: Photothermal optical time domain reflectometry, showing the reflection of differentially frequency shifted light from reflectors (R_n) and their detection at a photodiode (PD) (adapted from Jin *et al.*[114])

Figure 3.3 shows the experimental layout for a system of multipoint gas detection based on the fact that when a gas absorbs light, it is heated and its refractive index changes[115]. This heating is performed by a modulated pump laser with operating power of the order of 100mW. The probe consists of two pulses of light formed from a single pulsed laser source. Each pulse is frequency shifted by a different amount by acousto-optic modulators (AOM) to produce frequencies of $f_0 + f_1$ and $f_0 + f_2$ and a time delay (τ) is established between them by way of fibre delay loops. These pulses are reflected back at specific points along the sensing path to the photo detector (R_n) where they are detected at times determined by the distance they have travelled and the time delay they experienced in fibre loops. Careful selection of the time delay length and the length of the distance between the reflectance points means that the pulse with frequency $f_0 + f_1$ re-

flected back from reflection point R_1 will arrive at the photodiode at the same time as the pulse $f_0 + f_2$ that has been reflected back from R_2 and interfere to produce a beat signal, the phase of which is determined by the phase difference between the two pulses. Similarly, at another instant of time, these pulses, reflected back from R_3 and R_4, will arrive at the photodetector and interfere. The time that these signals arrive at the photodetector is determined by the distance they have travelled and it is this that allows the identification of each sensing unit. The phase difference between the two pulses, and so the phase of the beat signal, is determined by the distance they have travelled relative to one another and the refractive index of the medium they have travelled through. The sensing region is made up of structured optical fibre where light is guided in airspaces within the fibre rather than in a glass core, meaning that the light is able to interact with the gas within the fibre[116, 117]. An example of a structured optical fibre is shown in Figure 3.4. The change of the gas refractive index by the pump laser means that the phase of the beat frequency from each sensing region in this manner is proportional to the gas concentration.
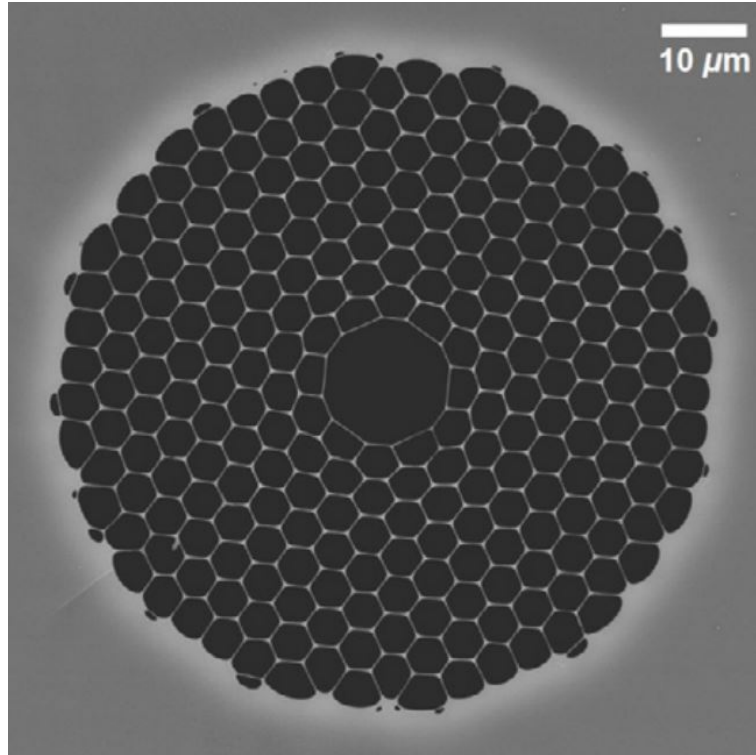
Figure 3.4: Structured optical fibre. In this example, the light is guided down the central air filled core, which can also act as a gas cell (from van Brakel *et al.*[118].)

As well as reflections from the reflective surfaces, optical fibres backscatter light along their whole length, and this backscattered light can be measured in a similar way to that reflected light. These techniques have been used to measure concentrations of acetylene as low as 10ppb, with spatial resolutions, determined y the pulse width and the temporal spacing between the two pulses, of around 30m[115].

3.3.2 *LIDAR*

Named for its resemblance to RADAR, Light Detection And Ranging (abbreviated to LIDAR)[119] is a somewhat loosely defined, free-space form of sensing that wherein a target if illuminated by a laser, generating a signal in response. This signal can be cause by a number of process such as Rayleigh scattering[120, 121] or Raman scattering[122]. A schematic of a generalised LIDAR system is

shown below in Figure 3.5 that shows a laser sending a beam to a surface (S) that is then reflected back as a response beam to optical systems that measure the intensity of the response signal as a function of time.
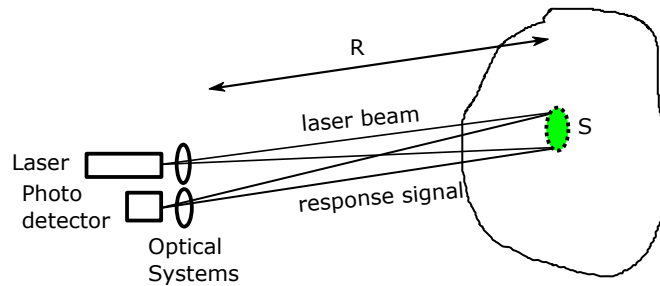
Figure 3.5: Principles of LIDAR (after [119, p340] showing a laser being reflected from a surface S at a distance R from the source

The power of the signal at the detector over time will be determined by various factors such as the response of the illuminated object to the laser(including its reflectance), the distance between the object and the light source as well as information about how light propagates in the medium between the light source and the object under test.

If the laser beam is pulsed then the power of the response beam as a function of time would contain information about the time taken for the pulse to travel from the laser to the target and back. This, combined with the speed of light enables the distance to target to be calculated. This is the basis of the use of LIDAR as a range detection system, such as in autonomous driver controls[123, 124, 125]. As well as detecting solid objects, the back-scattering of light by the atmosphere can be used to measure wind speeds[126, 127]. These wind measurement systems do not interrogate the returned light directly but measure its interferometric interactions with another local source of light. It was with the aim of using this interferometric method of measuring wind speeds that the

technique used in this thesis, Range Resolved Interferometry was first theorised before it was used for fibre based shape sensing[128, p2]. Since the return signal contains information about any absorbance of the beam by the atmosphere it passes through LIDAR can be used as a gas sensing technology. By using two laser pulses of different wavelengths, one corresponding to an absorption feature of the gas under test, and one away from this absorption feature. By measuring the difference in the returned power (P_{det}) at each wavelength, the concentration of gases in the atmosphere can be calculated using the Beer-Lambert Law (see Section 2.4[129]. This, in addition to a pulse modulation encoded in the signal, allows a distributed measurement of the concentration of gas along the path of the laser beam. This process is known as differential absorption LIDAR (DIAL) and has been used to measure the concentrations of methane of approximately 1ppm with spatial resolutions of 100m[130] over ranges of 800m, while other experiments over shorter ranges have shown similar concentration detection capabilities with spatial resolution of the order of 10m[131].

3.4 FREQUENCY DOMAIN MULTIPLEXING

LIDAR is a free-space measurement system that operates by measuring the light reflected back towards the device and interrogating its power. Similar principles to those used in LIDAR, in particular the interferometric forms, can also be used in fibre linked systems for the measurement of locations of items of interest and to provide information about the medium through which the light is passed. One such methodology is Optical Frequency Domain Reflectometry (OFDR)[132, 133], of which Frequency Modulated Continuous Wave (FMCW) interferometry is a specific example, shown in Figure 3.6.
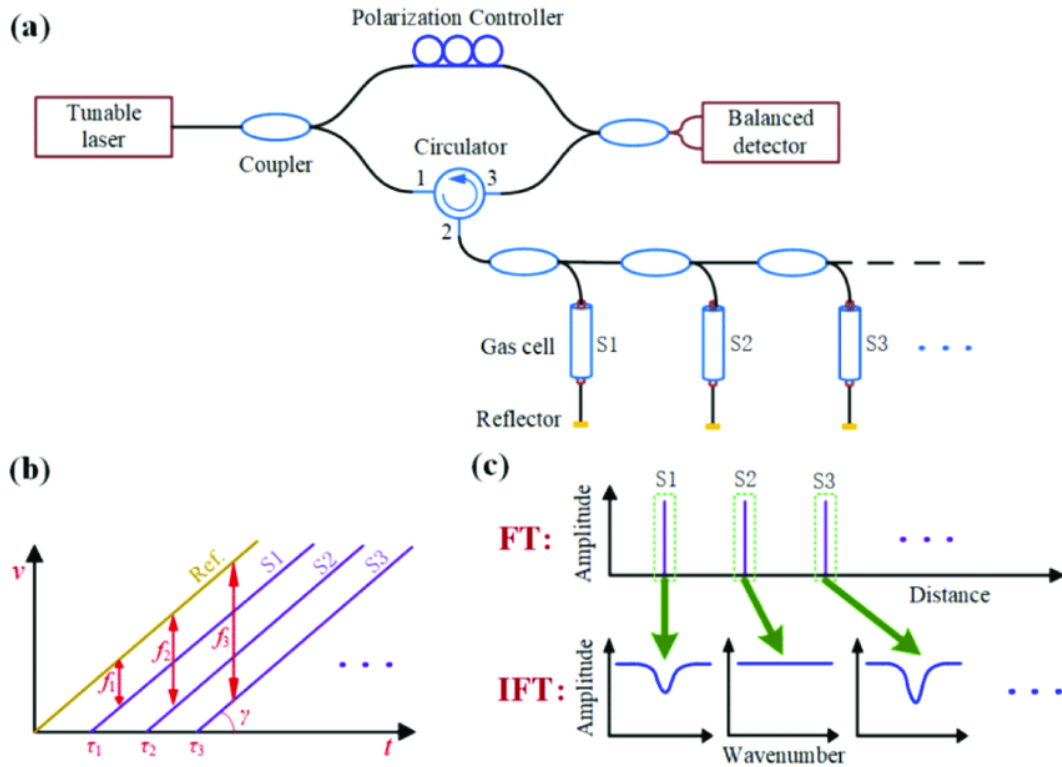
Figure 3.6: The experimental layout of a gas sensing system using FMCW. After Lou 2020[23] a) Schematic setup of system showing swept laser illuminating multiple sources and reflected light detected by balanced detector b) Wavelength of light returning via each path is time dependent c) Fourier transormation of the signal at the balanced detector allows measurement of gas absorption in each sensing region(From Lou *et al.*[23])

Based on the principle that interference between light beams of different frequencies will produce beat notes, the frequency of which is determined by the difference in frequencies between the beams, FMCW has been used to measure temperature[134], strain[135] and indirectly the presence of gases [136]. To directly measure the absorption of gases, the experiment shown in Figure 3.6 is used. A swept laser is split into two paths(Figure 3.6(a)), a sensing path (via the polarisation control) and a branched sensing path (S1-3). Light from the sensing path is reflected back and combines with the light passing down the reference path. Due to the differences in path lengths, the light from each path will be of a different frequency (ν) upon arrival at the detector (Figure 3.6(b), causing beat production with a frequency determined by the difference in frequencies. The frequencies of these beat notes, and thus the path differences of the beams,

can be seen via a Fourier transform (Figure 3.6(c i)) of the interferometric signal. Taking the inverse Fourier transform of specific spatial parts of this provides the spectral response caused by the absorption of the light by the gas in the sensing region. This can then be analysed to provide a measure of the gas concentration at each of the sensing regions(Figure 3.6c ii)[23]. This methodology has been used to make measurements of acetylene with concentrations as low as 55ppm at a distance of 52m, and a spatial resolution of 30cm.[23]. A system that similarly relies on different frequencies combining, but using a frequency shifter is described by Ye *et al.* [137] and was able to measure acetylene at 230ppm. This technique uses the difference in phases of beams reflected from different points in the length of a single fibre to determine the relative positions of those reflection points.

Range Resolved Interferometry, the technique described in this thesis is itself an FMCW technique using a sinusoidally rather than ramp modulated laser. Like other FMCW it allows the measurement at a number of points but with the advantage of using a simple and cost effective DFB laser as opposed to the more complex lasers used in other FMCW techniques.

3.5 TOPOLOGIES

As well as using different sensing techniques, it can be noted that the fibre linked systems described above have their sensing regions connected in different arrangements. While a larger number of such topologies exist[138, 139], 4 are discussed as potential topologies for the shown in Figure 3.7.
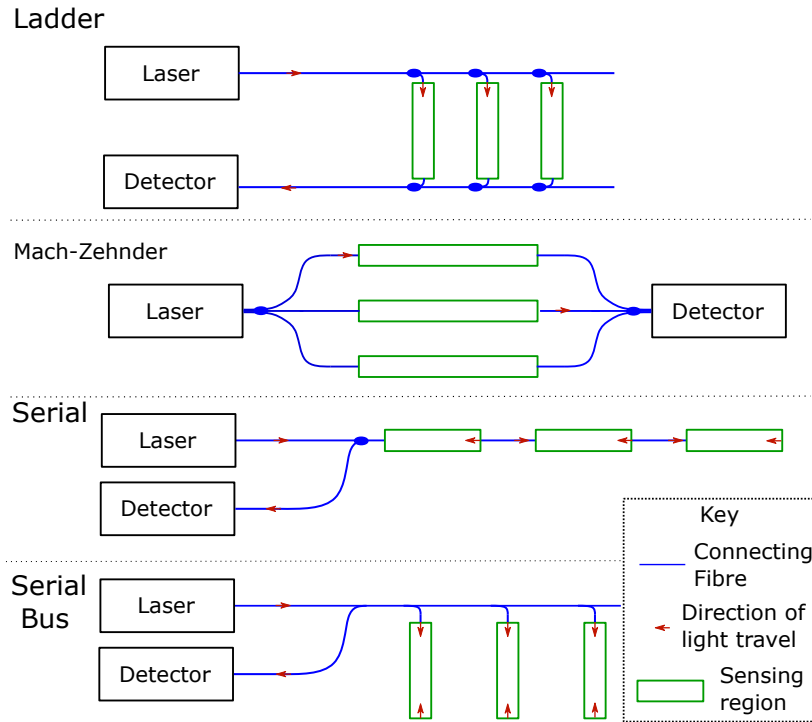
Figure 3.7: Four possible topological arrangements of sensing regions. From top to bottom: Ladder, Mach-Zehnder, Serial and Serial-Bus

In the ladder topology, light passes through in one direction through the sensing regions, with each sensing region branching off from a common path, before being recombined in a similar path. In such a system, the amount of light passing through each sensing region will depend on its place in the ladder and the coupling ratio used to direct light into it. If constant coupling ratios are used for all branches of the ladder, then each rung of the ladder will be illuminated by a lower intensity of light than the previous one. Alternatively different coupling ratios for the different rungs of the ladder to ensure an equal light intensity within each sensing region. In the Mach-Zehnder configuration, the light is split into a number of paths before passing through the sensing regions after which is recombined to form an interferometric signal that can be interpreted. In this arrangement, the intensity of light passing through the sensing regions is determined solely by the coupling ratio used. A serial topology uses a number of senor regions joined together sequentially with partial reflectors between them. Light passes through the sensing region and at each partial reflector a portion is

sent back towards a detector. In this case, the intensity of light that reaches each sensor region is a function of both the amount of light that is absorbed in the sensing regions before it in the system and the reflectivity of the partial reflectors used. A serial bus topology is similar to the ladder topology in that light is coupled off from a common path into each sensing region, but unlike the ladder topology, it is reflected back toward the common path and then to a detector. As with the ladder topology, the intensity of light in each sensing region is determined by a combination of its position within the system and combinations of coupling ratios used. It has been shown that absorption based systems in the ladder topology suffer less from problems wherein light backscattered within the fibres interferes with unscattered light which carries the signal associated with the gas concentration [140]. However, these systems are more complex in terms of fibre layout than the serial and serial bus topologies[128] and so may not be the most suitable for real world deployment.

3.6 POLARISATION EFFECTS

Fibre interferometric sensors are susceptible to polarisation induced signal fading. This occurs when the polarisation states of the combined light approach orthogonality, causing the visibility of the interferometric fringes to be reduced[141]. This change in relative polarisation states of the beams is caused by the differential changes in the birefringent properties of the fibre constituting the two paths that the light can take, and is effected by variations in the temperature and position of the fibre[142], with bending in the fibre being one specific cause[141]. In order to mitigate this effect, there are effectively two approaches, to prevent the change from occurring or to apply techniques to mitigate after the fact. Polarisation state changes within the fibre can be lessened with the use of polarisation maintaining fibres or countered using polarisation controls[141]. Similarly, in reflection mode interferometers, Faraday reflectors can be used to add stability to

polarisation states upon recombination[143] by ensuring that any polarisation changes in each fibre path are reversed on the return journey. In order to mitigate the effect of the polarisation differences, a system of polarisation diversity sensing can be used which polarise the received light in three or more independent polarisers and measuring the resultant optical signals, it can be made certain that there will never be complete fading of the fringe visibility[144, 145].

3.7 SUMMARY

The potential for reduced cost per sensing unit, as well as lower levels of complexity in comparison to systems of multiple sensors, make the development of multipoint sensors a highly desirable goal. A number of techniques have been developed to meet this goal. While multiplexed photothermal has been shown to offer the ability to detect methane at suitable levels for the work use cases envisioned within this thesis, it does so using lasers with relatively high powers which carries the risk of ignition of the gas if greater measurement distances were used. It also requires the careful placement of the reflective surfaces. FMCW also has potential for use in this operating regime, but the requirement for more complex lasers makes it more expensive than the diode laser based Range Resolved Interferometry methodology that will be introduced in the next chapter.

4

RANGE RESOLVED INTERFEROMETRY

4.1 INTRODUCTION

Range Resolved Interferometry (RRI) is a form of frequency modulated continuous wave interferometry that allows the measurement of the characteristics of individual signals from within the signal produced by a system of multiplexed interferometers. Unlike the Frequency Modulated Continuous Wave (FMCW) systems described in Section 3.4 which use linearly ramped wavelength modulation, RRI uses a sinusoidal modulation to produce the interferences which are then interrogated. The work published thus far using RRI has been based on the extraction of phase information from the interferometers and using changes in phase as a measure for changes in optical path differences in the constituent interferometers. This has allowed the technique to be used in both free space configurations and in fibre optics for the measurement of vibrations of surfaces[146], structural dynamics in helicopter rotor blades[147], the position of a translational stage[148] and work piece position sensing in robotic manufacturing[149]. The experimental work described in this thesis is the first use of the RRI technology to extract spectral information from sensing regions using intensity measurements extracted using RRI, and is thus comparable to the spectral analysis work used in Lou *et al.*[23], but while Lou *et al.* used an external cavity laser, the RRI approach uses a more cost effective distributed feedback (DFB) laser, reducing the cost of the system significantly. A complete description of the process of Range Resolved Interferometry can be found in the work of T Kissinger[128, 24]. This chapter, which is based on those works, will provide a level of description

of the process necessary to understand the steps taken to extract the intensity of light passing through each gas sensing region.

4.2 INTERFEROMETRY

Assuming a linear wavelength response to current modulation, A DFB laser, as used in the work in this thesis, when subject to a sinusoidal injection current with an ,modulation frequency f_m will produce an output whose optical wavelength $\lambda_{(t)}$ will be given by Equation 4.1 where $\Delta\lambda$ is the amplitude of the wavelength modulation and is determined by the amplitude of the modulating current, and λ_0 is the centre wavelength.

$$\lambda(t) = \lambda_0 + \Delta\lambda \sin\left(2\pi f_m t\right) \tag{4.1}$$

In a two armed interferometer such as that shown in Figure 4.1 (assuming coherence and polarisation matching between the arms), this would produce a signal at the photodetector given by Equation 4.2 where in P_1 and P_2 are the light power passing through each arm of the interferometer, R is the responsivity of the detector, and $\Delta\Phi$ is the phase difference of the beams passing through the arms[24].

$$U(t) = R[(P_1 + P_2) + 2\sqrt{P_1 P_2} \cos(\Delta\Phi)] \tag{4.2}$$
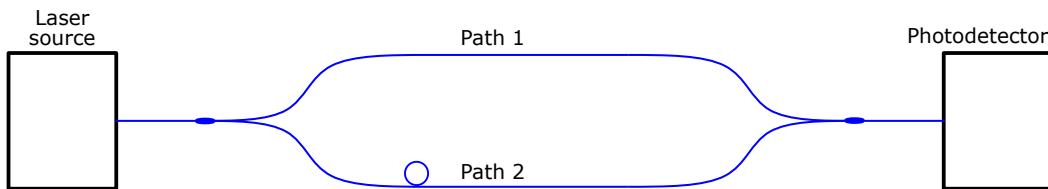
Figure 4.1: A simple, two armed interferometer

This can also be expressed in the form of Equation 4.3 in which In this equation, R is the responsivity of the detector, P_{avg} is the average power in the detec-

tor, V is the visibility of the fringes, τ is the time of flight delay for beams of light passing through the two arms of each interferometer and $\phi(t)$ is the interferometric phase of the signal. A is the amplitude of a phase carrier function which is described below.

$$U_t = RP_{avg} + V_n \cos(A \sin(\omega_m(t - \tau)) + \phi(t)) \tag{4.3}$$

A more complex interferometer, such as one with three arms as in Figure 4.2 will similarly produce a signal at the photodiode that is a superposition of the multiple interferometers within the system.
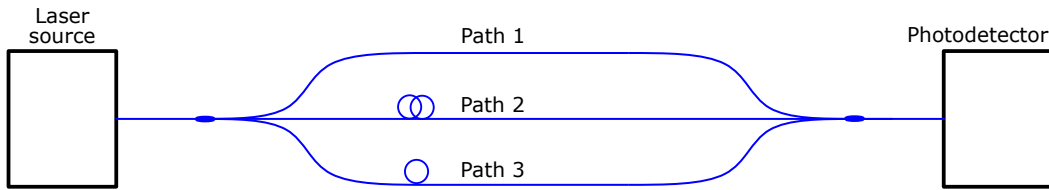
Figure 4.2: An interferometer formed of three arms

In a three armed interferometer, there are three constituent interferometers, created by the pairs of optical path lengths within the system. In this case, the pairs are formed by Path 1 & Path 2, Path 1 & Path 3 and Path 2 & Path 3. The resulting interferogram produced by a system of N interferometers is given by Equation 4.4[24].

$$U(t) = RP_{avg} + \sum_{n=1}^{N} RP_n V_n \cos(A_n \sin(\omega_m(t - 0.5\tau_n)) + \phi_n(t)) \tag{4.4}$$

In this equation, which is an extension of Equation 4.3 R is the responsivity of the detector, P_{avg} is the average power in the detector, V_n is the visibility of the fringes caused by each individual (nth) interferometer, τ_n is the time of flight delay for beams of light passing through the two arms of each interferometer and $\phi(t)$ is the interferometric phase of the signal from the nth interferometer. A_n is the interferometric phase carrier amplitude for each interferometer caused by the modulation of the laser shown in Equation 4.1. Assuming small values of

τ_n, A_n will be proportional to the OPD of the interferometer and the amplitude of frequency modulation and is given by Equation 4.5 in which Δf_{opt} is the amplitude of the frequency modulation of the light, while η_k is the OPD of the interferometer in question and c_0 is the speed of light in a vacuum[24].

$$A_n = \frac{2\pi\Delta f_{opt}\eta_k}{c_0} \tag{4.5}$$

It is this proportionality between A_n and the OPD and the modulation amplitude that makes the separation of signals based on range information by RRI possible, as will be discussed below. The interferometric signal produced at the detector (U) in an interferometric system such as that in Figure 4.1 is shown below in Figure 4.3. In this instance, the values of A_n are set to be 25, 50, and 75 rad for each of the constituent interferometers.
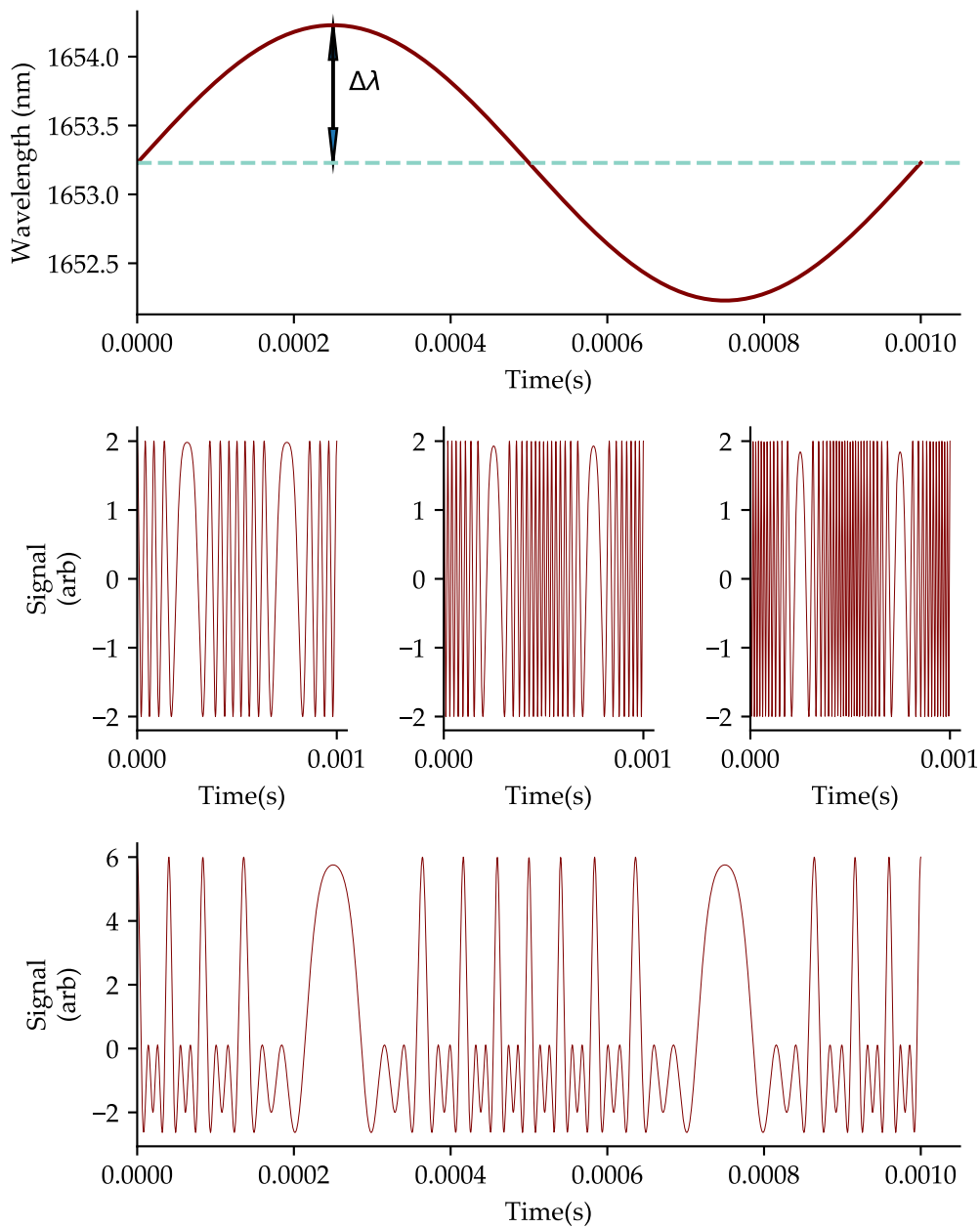
Figure 4.3: Top: The sinusoidal modulation of the laser with arbitrary units of angular frequency. The amplitude of this modulation ($\Delta\lambda$) is given by the maximum height above the central value (λ_0).
Middle: The interferograms that would be be recorded for each of the three constituent interferometers in Figure 4.1
Bottom: The resultant signal at the photodiode ($U(t)$) when the modulated laser is coupled through the interferometer

As can be seen in Equation 4.4, the photodiode signal (U)is a summation of the interference patterns produced by all the possible pairs of arms in the in-

terferometric system, and the role of RRI is to extract information pertaining to each individual interferometer, and the proportionality of A_n to the OPD and the amplitude modulation is the key to this process. The interferograms shown here represent the signal after some correction. The pure interferometric signal that would be measured at the photodiode contains the residual amplitude modulation that is present as a result of the laser modulation being current driven. However, this is normalised by the RRI systems used in this thesis and it is this normalised interferogram that is shown in Figure 4.3.

4.3   RRI SIGNAL DEMODULATION

In order to extract the information associated with each individual interferometer from the superposition of them all, the photodiode signal is demodulated by way of complex carriers ($C(t)$) with properties derived from the expected properties of each of the constituent interferometers in the system. An interferometric signal, in complex form, that would be produced by an interferometer with known values of A_d, ω_m, $t_s p$ and τ_d is given by Equation 4.6.

$$C(t) = e^{iA_d \sin(\omega_m(t - t_s p - 0.5\tau_d))} \tag{4.6}$$

An example of the real and imaginary parts of the complex carrier that would be produced by the constituent interferometer of Figure 4.1 with the phase carrier amplitude of 25rad is seen below in Equation 4.6.
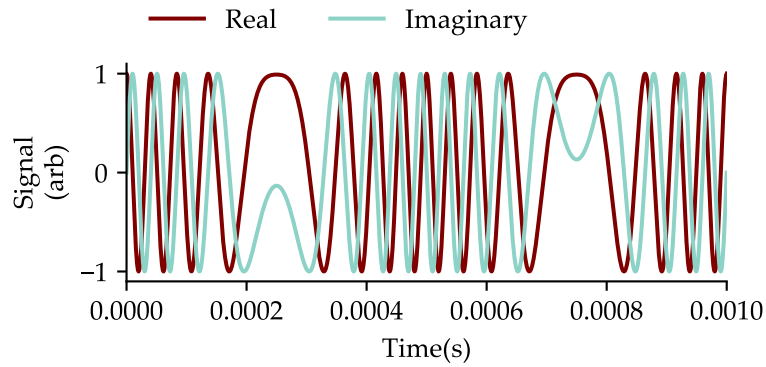
Figure 4.4: The real (red) and imaginary (blue) parts of the complex carrier signal ($C(t)$) associated with an interferometer with interferometric phase carrier amplitude A_d of 25 rad

In order to extract information about the portion of the interferometer signal ($U(t)$) that corresponds to a constituent interferometer with a given OPD, and thus a given interferometric phase carrier amplitude (A_n), the photodiode signal taken over the period of one sinusoidal modulation is multiplied by the complex carrier with that same phase carrier amplitude. In order to suppress the baseband contributions from other constituent interferometers than the one of interest, a Gaussian window function ($W(t)$) is also multiplied by these two functions. This results in a time varying, complex, product ($D(t)$). This demodulated signal is given by Equation 4.7. The value of $D(t)$ over a single modulation period is then lowpass filtered to produce a single, complex value for $Q(t)$ for each modulation period. This process is illustrated in Figure 4.5

$$D(t) = U(t)C(t)W(t) \tag{4.7}$$
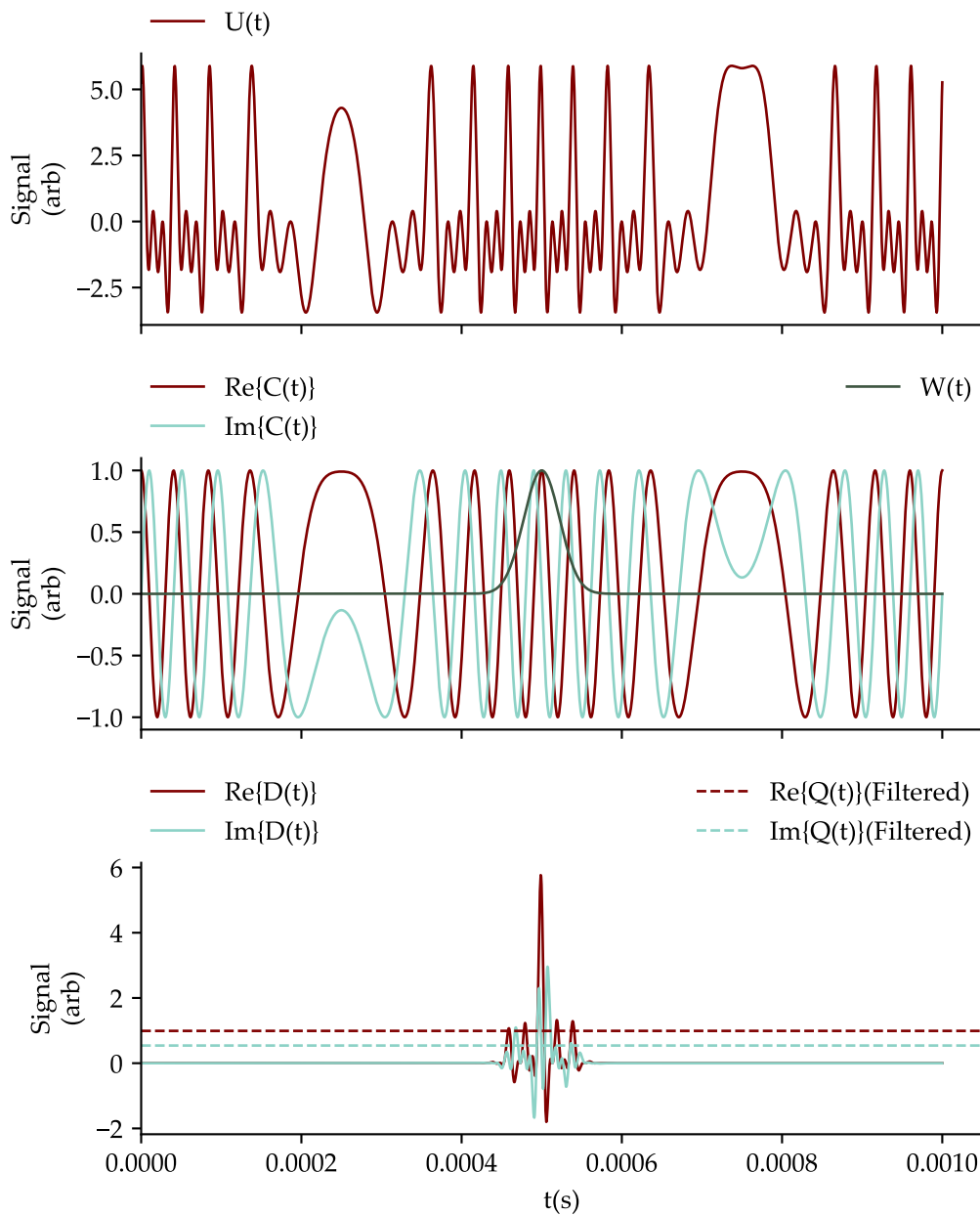
Figure 4.5: The RRI demodulation process.
Top: The photodiode signal (U_t) taken over the period of a single sinusoidal modulation period in the interferometer in Figure 4.1.
Middle: The complex carrier($C(t)$) associated with an interferometric phase carrier amplitude of interest along with the window function ($W(t)$) applied to suppress cross talk from other signals.
Bottom: The quadrature signal ($D(t)$) produced from the product $D(t)=U(t)C(t)W(t)$, along with a real and imaginary value of the quadrature signal values($Q(t)$) found by applying a low pass filter to the real and imaginary parts of $D(t)$

The interferometric signal produced by the nth, two armed interferometer in a system of interferometers such as that in Figure 4.1 shown in can be given in a simplified form as in Equation 4.8, where Z is the amplitude of the signal, and $\Delta\Phi$ contains its phase information.

$$U_n(t) \propto Z \cos \Delta\Phi \tag{4.8}$$
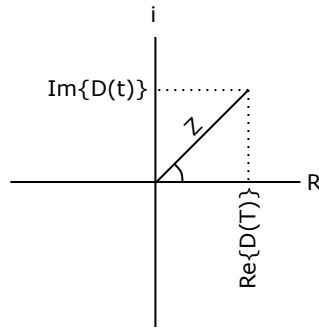
Figure 4.6: Argand Diagram showing the extraction of signal amplitude (Z) from the real (Re) and imaginary (Im)parts of the RRI signal

The value of Z can be extracted from the filtered quadrature signal (Q_t) by calculating the magnitude of the complex number Q_t as indicated by Z, the length of the line shown in Figure 4.6. This calculated value for Z is referred to in this thesis as the RRI amplitude. The phase information can also be extracted by taking the phase of Q_t, and this value is used in most RRI applications to date, but the work in this thesis only requires knowledge of the amplitude. For a given interferometric signal ($U(t)$), the use of different values of A_d, and thus different values of $C(t)$ will allow the measurement of the RRI amplitude as a function of A_d creating a map of the interferometer system.

4.4   RANGE RESOLUTION

With a given interferogram, the value of the RRI amplitude (Z) is a function of two factors, the intensity of light passing through the arms of the interferometer

and the similarity of the interferometric phase carrier amplitude of the demodulating complex carrier (A_d) and the interferometric phase carrier amplitude of specific interferometers in the system (A_n). Figure 4.7 shows the effect of demodulating with a value of A_d equal to that of a value of A_n and with a value of A_d different from A_n.
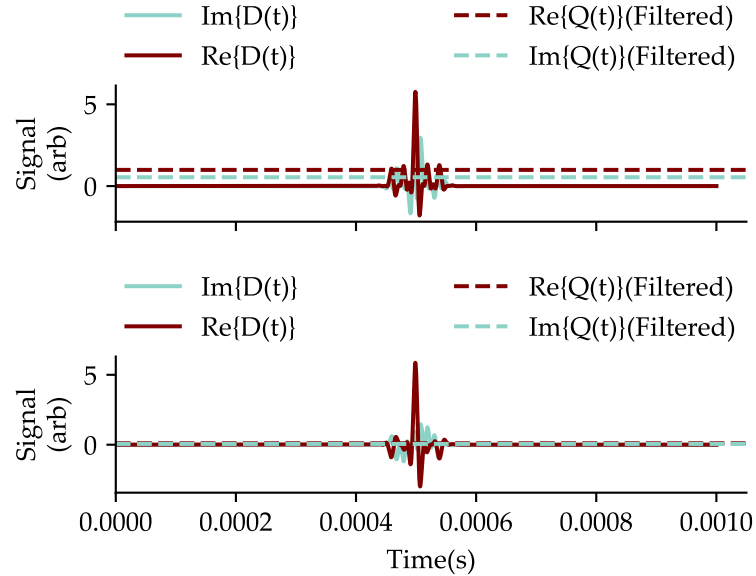
Figure 4.7: The effect of the chosen A_d value on the RRI Amplitude. With the same interferogram as in Figure 4.5, the top figure shows C(t) when A_d is chosen to be equal to a value of A_n, ($A_d = A_n = 25$rad), while the bottom shows the effect when they have different values, $A_d = 10$rad

By demodulating the interferogram (U(t)) with a series of complex demodulation carriers (C(t)) with different values of phase carrier amplitude (A_d), a plot can be made showing the RRI amplitude (Z) as a function of demodulation phase carrier amplitude (A_d). A plot of this type, known as an amplitude map, for the system shown in Figure 4.1 can be seen in Figure 4.8
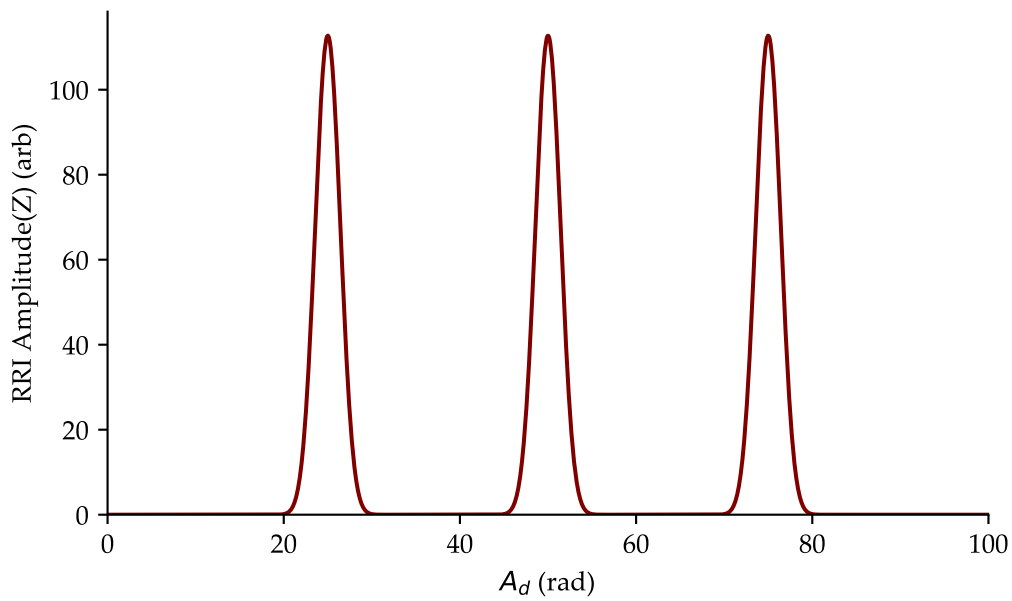
Figure 4.8: Plotting the RRI amplitude (Z) as a function of demodulation phase carrier amplitude (A_d), shows the locations of the OPDs of the constituent interferometers in radian space. This example shows an interferometer similar to that in Figure 4.1, with three arms and thus three constituent interferometers.

Each of the peaks of Figure 4.8 (referred to in the rest of this thesis as RRI amplitude peaks) shows the location, in radian space, of the constituent interferometers in the interferometric system. This information is then used in the measurement of the changing properties of those interferometers as a function of time.

4.4.1 Parasitic Peaks

For any given interferometric signal, it is unlikely that all the constituent interferometers will be of interest and it is necessary to be able to identify those which are of no interest. In the example of gas sensing, using an interferometric system like that in Figure 4.1, a system such as Figure 4.9 will be used.
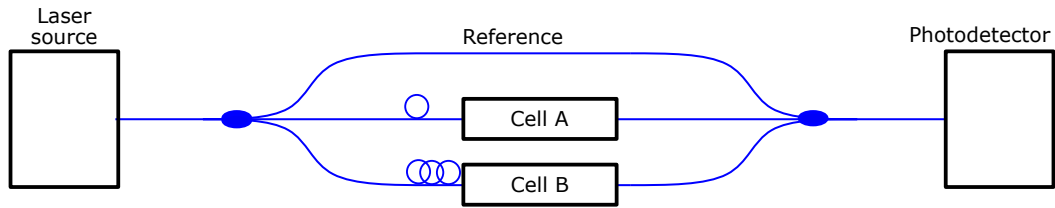
Figure 4.9: An interferometric system containing two gas cells and a reference arm. Additional lengths of optical fibre produce the required OPDs for interrogation.

This is a system in which two of the three arms contain gas cells and the other acts as a reference arm. In order to measure the behaviour of the light passing through each gas cell, the light is examined when it has interfered with the light passing through the reference arm. That is to say, we are interested in the behaviour of interferometers <Reference & Cell A> and <Reference & Cell B>. Assuming constant behaviour of the light in the reference arm, any change in the recorded RRI amplitude of the interferometers can be ascribed to changes in Cell A or Cell B. In the case of the work in this thesis this will be due to the presence of methane in the cell, absorbing the light. The interferometer caused by interaction of light passing through Cell A and Cell B is not of interest to us, as it would not be possible to determine the location of the cause of any change in the properties of the interferometer. The interferometer that is not of interest, in this case <Cell A & Cell B>, is referred to as parasitic, and the RRI peak associated with it is referred to as a parasitic peak. In this simplified example, there is just a single parasitic peak, but in more complex systems with multiple arms, or in more complex topologies there will be a larger number of these parasitic peaks, and their positions need to be considered when designing the system. They can be identified on the RRI amplitude map with knowledge of their approximate OPDs in relation to the OPDs of the interferometers of interest and thus do not need to have their properties measured. An example of an RRI amplitude map showing the parasitic peak is shown in Figure 4.10.
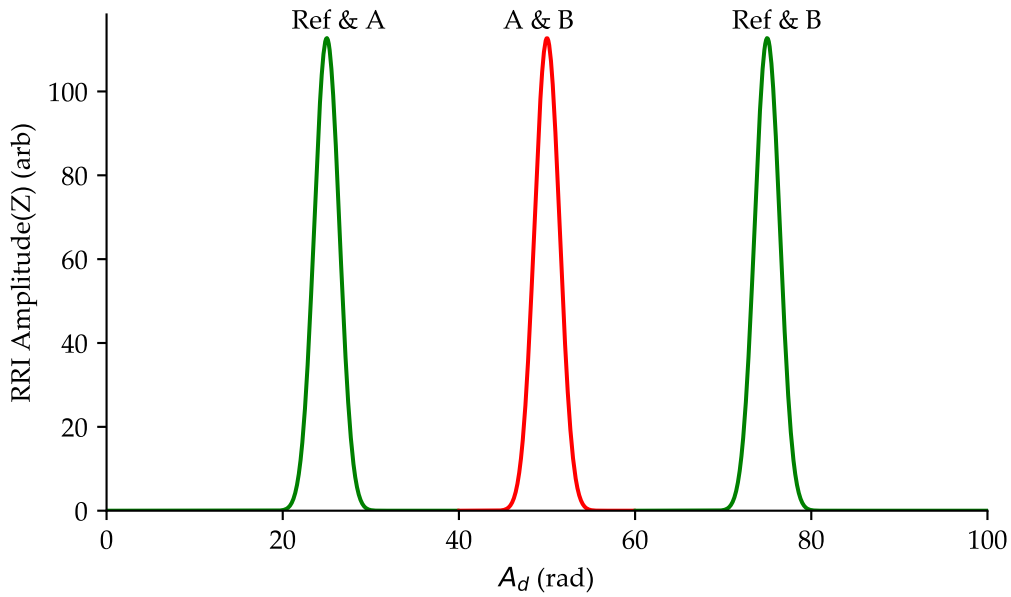
Figure 4.10: The RRI amplitude map of the interferometer shown in Figure 4.9, with the peaks associated with the combinations of gas cells with the reference arm shaded in green, while the parasitic peak formed by the interference between the two arms containing gas cells is shown in red.

4.5 AMPLITUDE DEMODULATION

Once the interferometers of interest have been identified and their phase carrier modulations have been measured using the technique described above, their properties can be measured as a function of time. In order to investigate the properties of each of the interferometers, the value of $Q(t)$ for each of them is measured using $C(t)$ with the appropriate value of A_d for each interferometer of interest. This is done in parallel for each of the interferometers allowing a continuous measure of the RRI amplitude (Z) for each interferometer as a function of time. For example; the interferometers of interest in Figure 4.9 are known to be those at 25 rad and 75 rad, a system would repeatedly calculate Z_1 and Z_2, by applying Equation 4.9 with C_n being the appropriate complex carriers with A_n, having values of 25 rad and 75 rad.

$$D_n(t) = U(t)W(t)C_n(t) \qquad (4.9)$$

This process is applied for each period of the modulation, and simultaneously for all values of C_n. This requires the use of fast processing capabilities and for the work done in this thesis is achieved using an RRI demodulation system developed in the Engineering Photonics Centre at Cranfield University. Having a measure for the RRI amplitude of each interferometer, this can be used to calculate a measure of the light intensity within each interferometer using a modified version of Equation 4.8, as shown below in Equation 4.10, where I_1 and I_2 are the light intensities passing through each of the constituent arms of the interferometer.

$$U_n(t) \propto \sqrt{I_1 I_2} \cos \Delta\Phi \qquad (4.10)$$

As a consequence of Equation 4.10, if we again assume that the light through the reference arm is constant and there is no drift in polarisation states, then Z_n^2 can be used as a measure of the intensity of light passing through the gas cell of interest. This ability to measure the light intensity passing through multiple gas cells simultaneously, along with an understanding of the Beer-Lambert Law and tunable diode laser spectroscopy (Section 2.4.2) is what makes the RRI system capable of multipoint measurements of gas concentration.

4.6 SUMMARY

By demodulating the interferometric signal produced by a system with multiple constituent interferometers, RRI can be used to locate the positions of the constituent interferometers within that system allowing the identification of parasitic interferometers as well as interferometers of interest. The information about their location in radian space can then be used to constantly demodulate the in-

terferometric signal to provide information about the intensity of the light within each of the interferometers of interest, which in turn will allow the measurement of gas concentration at a number of locations.

The process of range resolution, and the time variant demodulation to provide a measure of the RRI amplitude is summarised below in Figure 4.11

Range Resolution

Acquire photodetector signal over one modulation period (U)
↓
Generate window function (W)
↓
Set initial value of demodulation amplitude (A_d)
↓
Generate demodulation signal (C) ←
↓
Multiply $D = U \times A_d \times C \times W$
↓
Low pass filter on D to produce complex number Q
↓
Amplitude of Q is RRI amplitude at this value of A_d →

Increment demodulation amplitude (A_d)

Signal demodulation

Generate window function (W)
↓
Set value of demodulation amplitudes (A_d)
↓
Generate demodulation signal (C)
↓
Acquire photodetector signal over one modulation period (U) ←
↓
Multiply $D = U \times A_d \times C \times W$
↓
Low pass filter on D to produce complex number Q
↓
Amplitude of Q is RRI amplitude for this modulation period →

Next modulation period

Figure 4.11: The processes by which the RRI amplitude map is created (left) and the RRI amplitude is monitored as a function of time at a given demodulation amplitude (right)

4.7 GLOSSARY

A number of terms have been introduced in this chapter that are unique to RRI in general and this use of RRI in particular, and so a glossary is provided below

for future reference:

RRI Amplitude: The magnitude of the complex value of $Q(t)$ which is in turn given by Equation 4.7

RRI Amplitude Map: A plot of the RRI Amplitude as a function of the phase carrier amplitude of the demodulating signal $C(t)$

RRI Peak: A peak present in an RRI amplitude map

Parasitic Interferometer: A constituent interferometer within the system other than those of interest

Parasitic Peak: A peak in the RRI amplitude map that is associated with a parasitic interferometer
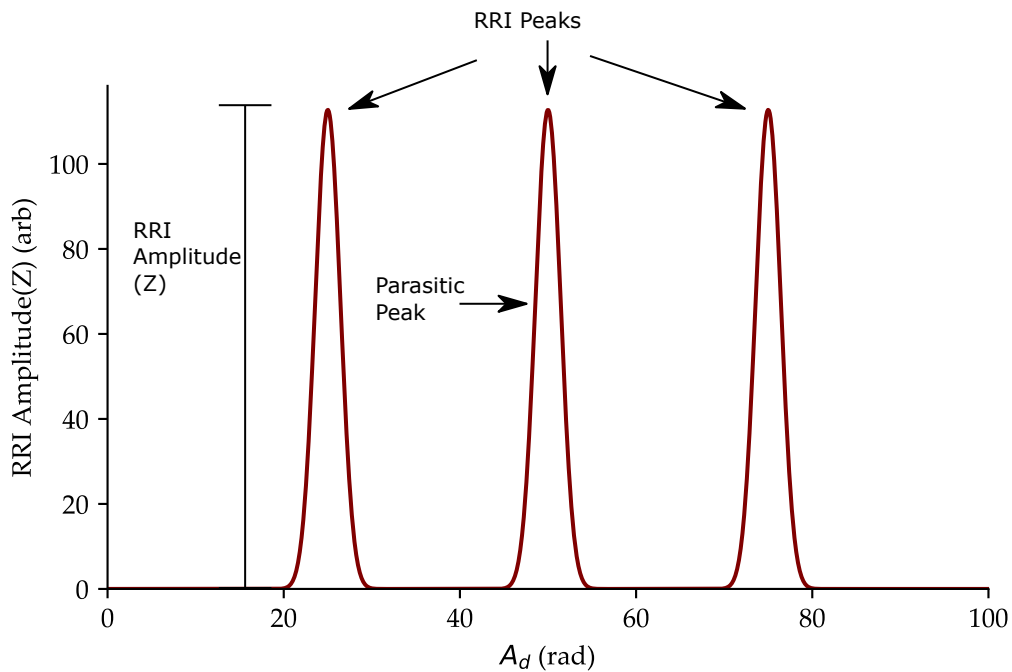
Figure 4.12: An RRI amplitude map with selected items from the glossary identified

5

PROOF OF CONCEPT WORK

5.1 INTRODUCTION

Section 2.1 describes the need for gas detection in both the environmental and safety regimes, while Section 2.4.2 describes the use of Tunable Diode Laser Spectroscopy (TDLS) to identify and measure the concentration of gas species. TDLS has a number of advantages including low signal to noise ratios[19] and gas specificity[150]. However, it is relatively expensive compared to other techniques such as electrochemical methods as described in Section 2.3. This means that in situations that require multiple sensing sites, it has not achieved widespread use[114] despite attempts to multiplex gas cells so that they can be interrogated using a single laser and/or detector[22, 114].

Chapter 4 discussed the principles of Range Resolved Interferometry, a method used to extract both phase and amplitude information of individual interferometers from a superposition of interferometers. While it has mostly been used for positional measurements[149] using the phase information, extraction of the amplitude of the interferometric signal would allow the measurement of light intensity in the constituent interferometer arms. This, in turn, would allow the measurement of light absorption in gas cells that form parts of an interferometer with multiple arms and so provide the potential for multiplexed gas detection.

The experimental work described in this chapter comprise the first steps towards implementing such a system.

5.2   INITIAL EXPERIMENTS

5.2.1   *Experimental equipment used*

In the experiments described in this thesis, a range of equipment was used and is described here.

5.2.1.1   *Laser and laser control*

- Laser: NEL NLK1U5EAA. A distributed feedback laser, wherein a diffraction grating provides the reflection necessary for the creation of the lasing cavity. It is capable of a wavelength in the range 1625-1670nm with a typical linewidth of 2MHz. In these experiments, it is modulated over a maximum range of approximately 1nm.

- Laser mount: ThorLabs LM14S2

- Laser temperature control: ThorLabs TED200

- Laser current control: ThorLabs LED202. This sets the driving current applied to the laser, and allows the modulation of that current through an applied voltage to an input of the current controller.

- Range Resolved Interferometry system: Two different RRI systems were used to apply a sinusoidal modulation to the laser controls. These are described in appendix A.

- Signal generator: Stanford Research DS345 function generator. This was used to apply the sawtooth modulation needed to sweep the laser's output wavelength across a methane absorption feature.

- Voltage adder: Stanford research systems SRS SR 560 low-noise voltage preamplifier. This was used, with no amplification, to combine the ramped

voltage from the signal generator with the sinusoidal voltage from the RRI system.

These items were used to control the output wavelength of the laser during the experimental work. While it is the driving current, and operating temperature of the laser that determines this wavelength, for the experiments described in this thesis, it was the voltages applied to the voltage adder along with the set points of the temperature and current control devices that were monitored.

5.2.1.2   *Light guidance*

Items used to control the path of the laser

- Optical fibre: SMF 9/125 fibre was used to couple light into other optical components and as additional fibre to produce differing path lengths within the interferometer arrangements.

- Couplers: $2\times$ 2 ThorLabs TW1650R5A2 couplers and 1×4 couplers from Fibrestore were used to split and recombine the light.

- Partial reflectors: ThorLabs in-line partial reflectors with 90% reflectance

- Collimating lenses: ThorLabs TC12APC-1550 collimating lenses were used to couple light into and out of the free space regions of the system

- Retroreflectors: ThorLabs, PS975M-C, SM1 thread mounted retroreflector prisms coated with a 1050-1700nm anti reflection coating were used to reflect light back through sensing regions in one arrangement of the system.

- Circulators: Fiberstore 33364 3 port circulators were used to ensure unidirectional travel of light in some of the configurations

5.2.1.3 *Sensing region equipment*

The following were used to create gas tubes in which light could interact with inserted gases. Each sensing region consisted of a clear plastic tube with windows at each end to allow gas to pass through.

- Gas tube: The gas was contained within clear acrylic tubes with an internal diameter of 15mm and a length of 1m

- Windows: ThorLabs WW11050-C wedged windows that prevent internal etalon formation were used at each end of the gas tubes

- Window mounts: SML103T angled optic mounts were used to hold the windows at a 10° angle to prevent back reflections

- Lens tubes: ThorLabs SM1L20 lens tubes were used to hold the window mounts and were screwed onto the plastic piping, using PTFE tape for a better gas seal. Holes were drilled into the tube, and metal piping was attached to allow the insertion of gas into the tubes.

The fact that the lens tubes screwed onto the acrylic tubes allowed the length of the whole gas tube to be adjusted so that each was 1.09m in length, giving an approximate volume of 770cm^3 for each sensing region.

5.2.1.4 *Light detection and recording*

- Photodetector: ThorLabs PDA 10CS - EC InGaAs amplified detector, 700-1800nm range 17MHz bandwidth

- Oscilloscope: Tektronic DPO2014

- Optical Spectrum Analyzer: Yokogawa AQ6307 with a resolution of 0.02nm

5.2.1.5 *Gas*

Gas was provided from cylinders provided by BOC, and fed into the sensing regions by acrylic tubing and metal piping. The flow from each gas cylinder into the sensing regions was controlled by a mass-flow control system as shown in Figure 5.1

- Gas cylinders: Methane mix of 2.5% and 1000ppm with nitrogen balance. Synthetic air cylinder

- Gas flow control: The flow of gas was controlled by Brooks GF Series thermal mass flow controls with flow rates of 0-1000ccs^{-1}, 0-100ccs^{-1} and 0-10ccs^{-1} with stated repeatability of 0.15%. Connecting the gas cylinders to these allowed a controlled mixing of synthetic air and methane to the desired concentrations.

5.2.1.6 *Control Of Gas Concentration*

For the behaviour of the system in response to varying gas concentrations to be measured, it is necessary for the methane concentrations in the gas tubes to be controlled. The mechanism for this is described here.

the sensing regions described in Section 5.2.1.5 were part of a gas flow system shown below in Figure 5.1
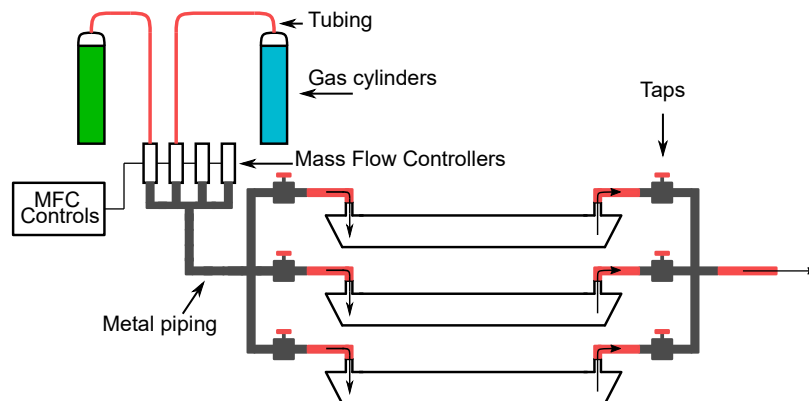
Figure 5.1: A schematic diagram of the gas flow control system

The valves allow each tube to be independently filled and isolated from the environment. The flow of gas from the cylinders to the gas tubes is regulated by a set of Brooks GFE100 Mass Flow Controllers (MFCs). There are four MFCs, two of which (MFC1 & MFC2) operate with flow rates of 0-1000cm^{3}min^{-1}, while the other two(MFC3 & MFC4) have operating ranges of 0-100cm^{3}min^{-1} and 0-10cm$^{3-1}$ respectively with a stated repeatability of 0.15% of the set flow rate. A cylinder of synthetic, hydrocarbon-free air is connected to MFC-1, with a flow rate of 0-1000cm^{3}min^{-1}. Meanwhile, a cylinder of 1000ppm methane mixed with air is attached to one of the other MFCs, depending on the required flow rate. The flow from the MFCs in use is then mixed in the common pipeline, to provide a methane concentration given by Equation 5.1 where FR refers to the flow rates of each gas as reported by the mass flow controllers, and Conc refers to the concentration.

$$\frac{\text{FR(Methane)} \times \text{Conc(MethaneIn)}}{\text{FR(Methane)} + \text{FR(Air)}} = \text{Conc(Mix)} \tag{5.1}$$

After mixing in the common pipeline, the gas mixture is divided into the three gas tubes. Each tube is controlled by taps at each end, opening and closing the upstream valve allows each tube to be independently filled or not with the gas mixture, while closing the downstream along with the upstream valve keeps the concentration within the gas tube constant for testing. When all valves are open, gas is allowed to vent into the laboratory ceiling close to an air extraction vent by way of a length of tubing.

In order to fill the gas cells with a set concentration of methane, the flow rates of the MFCs are set to produce the required concentration and the valves are set to allow the gas to flow through the tubes. In order to ensure flushing of any previous gas in the tube, gas is allowed to flow through the system for 600 seconds. With a total flow rate of approximately 1000cm^{3}min^{-1}, this provided the system with sufficient gas flow in that period to fill the three gas tubes twice over, once to flush the previous contents and once to fill the gas tubes. When

closing the valves for experimental testing, the downstream taps were closed first so that the tube remains at atmospheric pressure.

5.2.2 *Establishing the Presence of a Methane Absorption feature*

In order to measure the presence of gas, it was first necessary to ensure that the laser output wavelength, when modulated would sweep across the absorption feature of a methane gas line. To this end, the experimental scheme shown below in Figure 5.2 was set up.
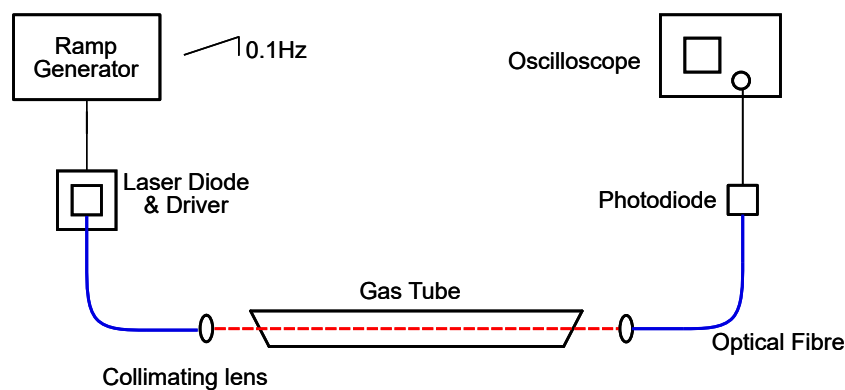
Figure 5.2: Experimental equipment that was used to perform Tunable Diode Laser Spectroscopy to ensure that the laser was sweeping across a gas line.

The gas tube was filled with 2.5%$_v$ methane and the signal generator was programmed to provide a 0.5V$_{pp}$ sawtooth modulation to the laser current driver. This modulation caused the laser output wavelength to be modulated by approximately 0.5nm, enough to cover a gas line while providing some baseline measurement off the gas line. The output voltage of the photodetector was monitored using the oscilloscope and the driving current and the temperature of the laser driver were adjusted using the temperature and current control units (TED and TEC) until an absorption line, indicated by a drop in the photodiode voltage, was found as shown in Figure 5.3.
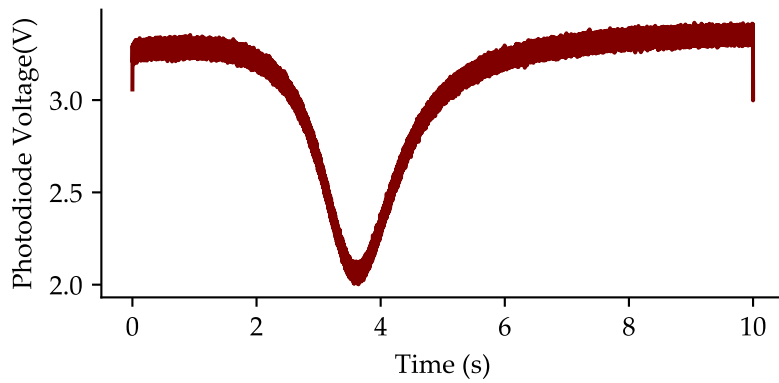
Figure 5.3: The photodiode signal measured as the laser frequency was swept across an absorption feature of 2.5% concentration in an approximately 1m column

Having set the laser output frequency so that a ramped modulation causes it to sweep across a methane absorption feature, the central wavelength was measured using the optical spectrum analyser and found to be 1653.7($\pm$0.02)nm which is a known absorption feature of methane[62]. The applied central driving current of the TEC control was 97.75mA, while the resistance value applied by the temperature control was 5.142kΩ

5.2.2.1 *First Application of Range Resolved Interferometry*

The experimental apparatus as shown in Figure 5.4 was then assembled to begin investigation of Range Resolved Interferometry as a gas detection system.
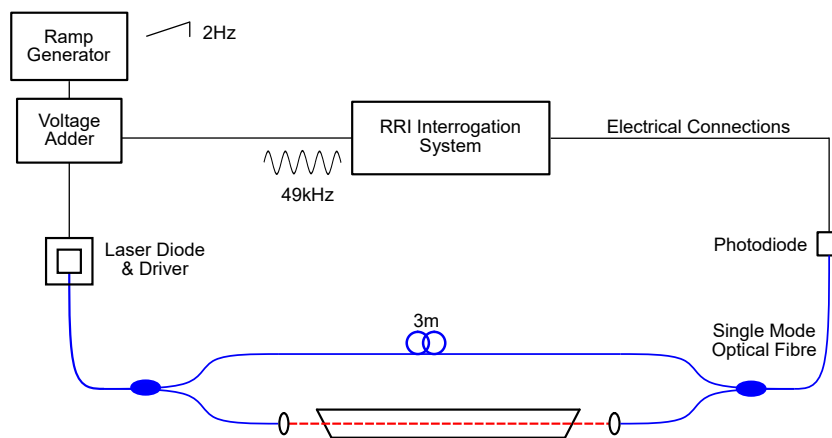
Figure 5.4: Experimental equipment used in the first application of Range Resolved Interferometry to detect methane

The RRI unit provided the laser with a sine wave modulation with an amplitude of 7mA and a frequency of 49kHz. Alone, this produced a wavelength modulation of 8($\pm$0.02)pm. This wavelength modulation was measured using the Yokogawa OSA using the technique described in more detail in Chapter 6

The system shown above in Figure 5.4 formed a single Mach-Zehnder interferometer between the reference arm, and the arm containing the gas cell. The resultant interferometer produced the interferometric signal as shown below in Figure 5.5. The interferometric signal shows the sinusoidal amplitude modulation in the light intensity associated with the sinusoidal modulation of the laser driving current, but this effect is removed within the software of the RRI interrogation unit. Using the algorithm in Section 4.4, the RRI interrogation unit showed a peak in the RRI amplitude map at approximately 33 radians as shown in Figure 5.6.
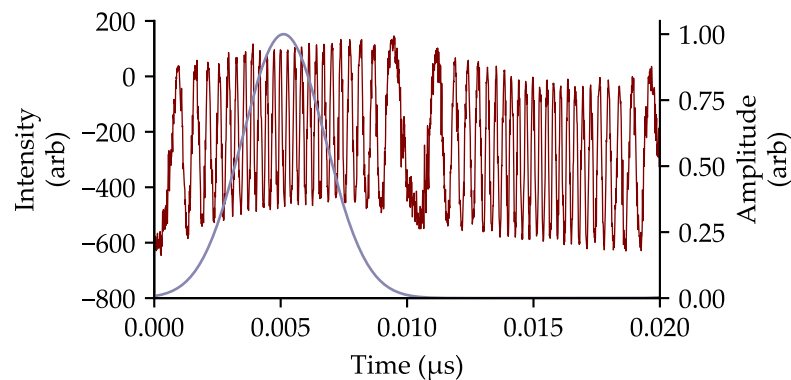
Figure 5.5: Interferometric signal produced by the modulation of a DFB laser by 49kHz, 7mA signal in the interferometer as shown in Figure 5.4 along with the window ($W(t)$) used in demodulation
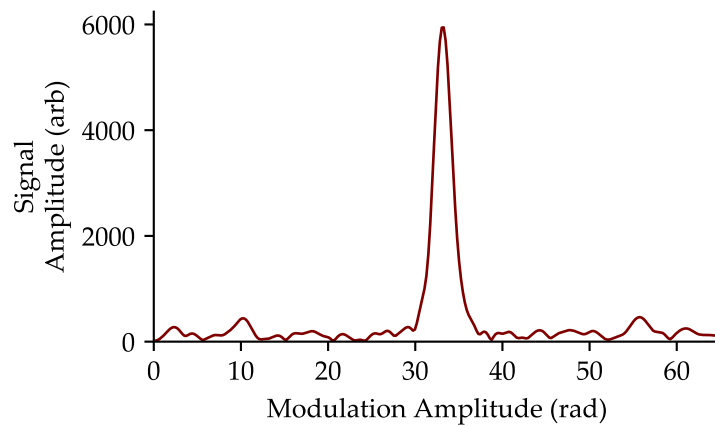
Figure 5.6: Range resolved amplitude map produced by a single gas tube and a 3m reference arm

This position of 33 radians was chosen for the continuous measurement of the signal amplitude. The ramp modulation used previously in Section 5.2.2, but operating at 2Hz rather than 0.1Hz was added to the RRI modulation using the Stanford pre-amplifier to sweep the laser wavelength across the methane absorption feature.

The gas cell was filled with gas from a cylinder containing 2.5% methane for 5 minutes before the taps were closed (see Figure 5.1). The taps were closed starting at the filling end to ensure that the gas cells would remain at atmospheric pressure. The RRI system was set to measure the signal amplitude at the range of 33rads, over a 1 second period, to capture signal over two of the slow ramp periods. Over the duration of the ramped laser modulation, it was seen that RRI peak shown in Figure 5.7 moved. This was due to the different response of the DFB laser to modulation at different central bias voltages and will be investigated and described further in Chapter 6, but an example of such a shift is shown below in Figure 5.7.
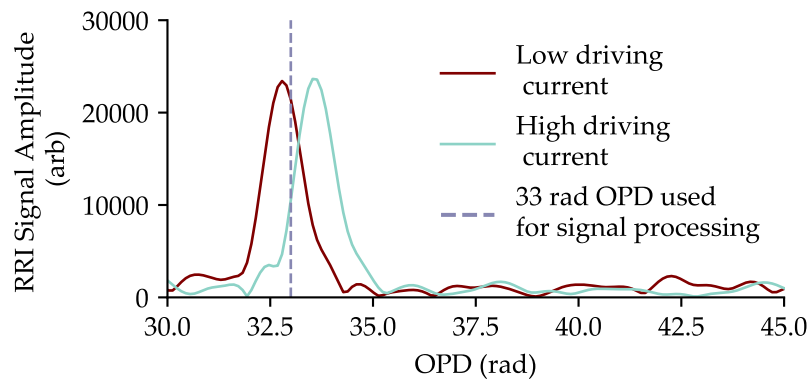
Figure 5.7: Visualisation of the apparant shift in OPD space (x-axis) of a typical RRI amplitude peak due to the presence of a ramped modulation of the laser's central output wavelength, showing position fo RRI peak at low driving current (red) and high (blue)

The RRI amplitude was measured at the 33 radians position over 1 second, and is shown below in Figure 5.8.
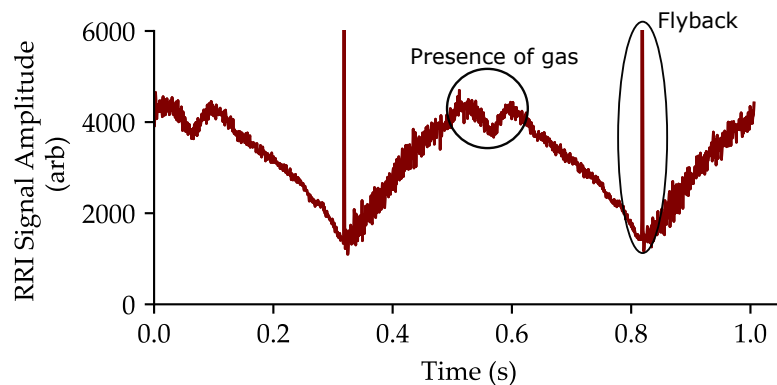
Figure 5.8: The RRI signal amplitude measured using the equipment from Figure 5.4, measured at an OPD of 33 radians. This shows the presence of a 1000ppm concentration of methane.

Figure 5.8 shows the result of the apparent motion of the RRI amplitude peak mentioned earlier and shown in Figure 5.6, with the amplitude of the signal rising and falling as RRI amplitude peak moved across the 33 radian measurement OPD. The vertical spikes occured at the point where the ramp ends and quickly restarted, causing the system to be unable to interpret that instant as a signal amplitude. However, at the centre of the ramp there was an apparent dip

in the measured signal intensity which corresponded to an absorption feature of methane as established in Figure 5.2.

In order to produce a standard TDLS-like plot as described in Section 2.4.2, it was necessary to capture the amplitude of the light intensity throughout the ramp as the RRI amplitude peak moved. To achieve this, the RRI interrogation unit was made to capture the signal amplitude at 23 points (the maximum provided by the RRI interrogation unit used) ranging from 21 rads to 44 rads to capture the peak across its whole range of motion. The combined measurements of multiple channels is shown in Figure 5.9. In Figure 5.9, each of the lines shows the amplitude of the RRI signal demodulated at a different notional OPD.
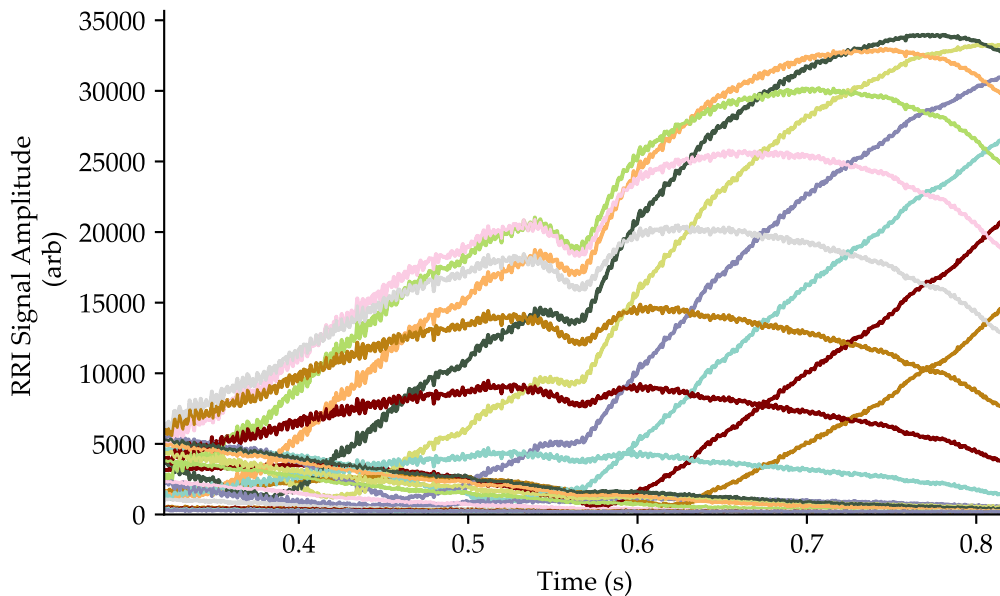
Figure 5.9: The RRI signal amplitude measured using the equipment from Section 5.2 with the presence of 1000ppm methane. The Signal amplitude was measured at 23 OPDs ranging from 21 to 44 radians. Each line represents the RRI amplitude measured at one of the 23 notional OPDs

Figure 5.9 has similarities to a TDLS curve as shows the presence of an aborption feature at approximately the centre of the sawtooth modulation, as previously seen in Figure 5.8 along with the increase in laser intensity across the ramp period caused by the increasing injection current. By taking the highest RRI amplitude measured at each instant, a plot as shown in Figure 5.10 can

be created which shows a TDLS-like image, with a clear absorption feature that could be used to determine the concentration of gas, as described in Section 2.4.2. In Figure 5.10, a single line is plotted corresponding to the highest value of the plots in Figure 5.9. The colour of the line changes to show which of the plotted lines in Figure 5.9 is contributing that highest value.
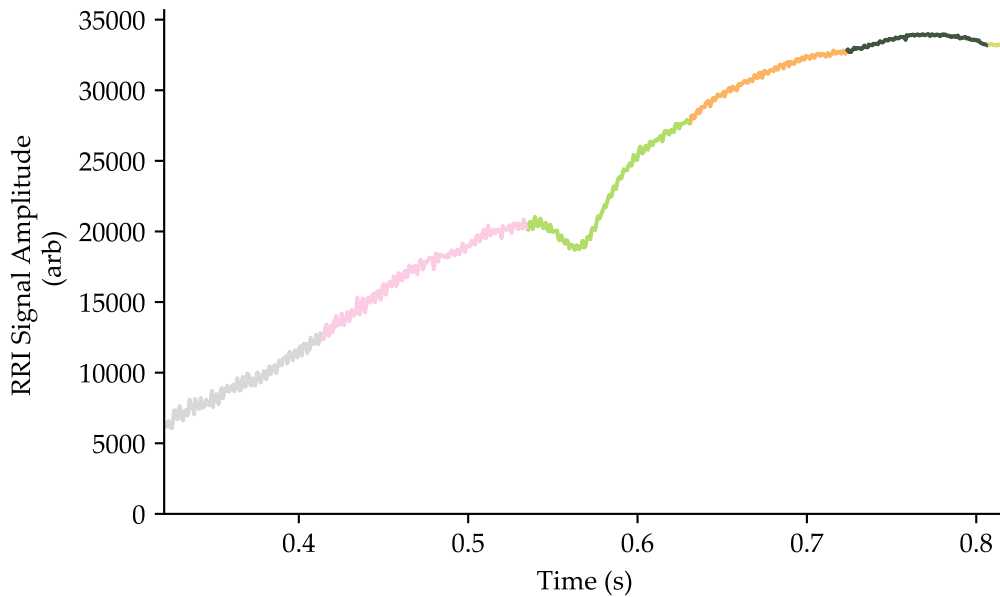
Figure 5.10: Using the highest RRI amplitude signal at each instant, the data in Figure 5.9 plotted to form a TDLS-like absorption feature. The colour of the line corresponds to the notional OPD that is providing that highest value as shown in Figure 5.9

5.2.3   *Creation of a TDLS-Like Output*

While Figure 5.10 shows the presence of the characteristic dip in intensity associated with TDLS, and is an improvement on Figure 5.8, it still inherits the latter's curved appearance as a result of the motion of the RRI amplitude peak as shown in Figure 5.7, and so a different technique was developed to produce a measure of light intensity passing through the sensing region that more closely mapped the expected output from a TDLS like system.

In order to achieve this, it was necessary to capture the height of the RRI amplitude peak for each RRI modulation period across the duration of the ramp.

Each of the RRI amplitude peaks of interest are interrogated using 7 of the available channels, rather than the 23 that were used in Figure 5.9 to allow for measurement of multiple sensing regions. 7 measurement channels were used for each sensing region as this gave the highest equal number of measurement points available across the 3 sensing regions. The RRI system then measured the RRI amplitude at each of these 7 channels as a function of time. To capture the height of the RRI amplitude peak as a function of time, these 7 amplitude values were used to reconstruct the RRI amplitude peak at each measured modulation interval.

5.3   DATA PROCESSING TO EXTRACT GAS CONCENTRATION

5.3.1   *RRI Amplitude Gaussian Fitting Algorithm*

The Range Resolved Interferometry system provides a value for the RRI amplitude at each of the interrogated notional OPDs at a frequency of 1.5kHz, that is a value every 7ms. This data is shown on screen and saved to a comma separated value (CSV) file for later processing. Software for post-processing of the data was created by the author in the Python programming language. The principle of operation is as follows: At each point in time ins which a measurement of signal amplitude was taken by the RRI system, each of the interrogated notional OPDs has a calculated RRI amplitude. The software divides these into as many sets as there are interferometers being investigated. The set of measured amplitudes for each interferometer is then fitted to a Gaussian curve using the lmfit Python module[67]. The heights of these fitted curves are then extracted and saved as a function of time. This process is illustrated in Figure 5.11
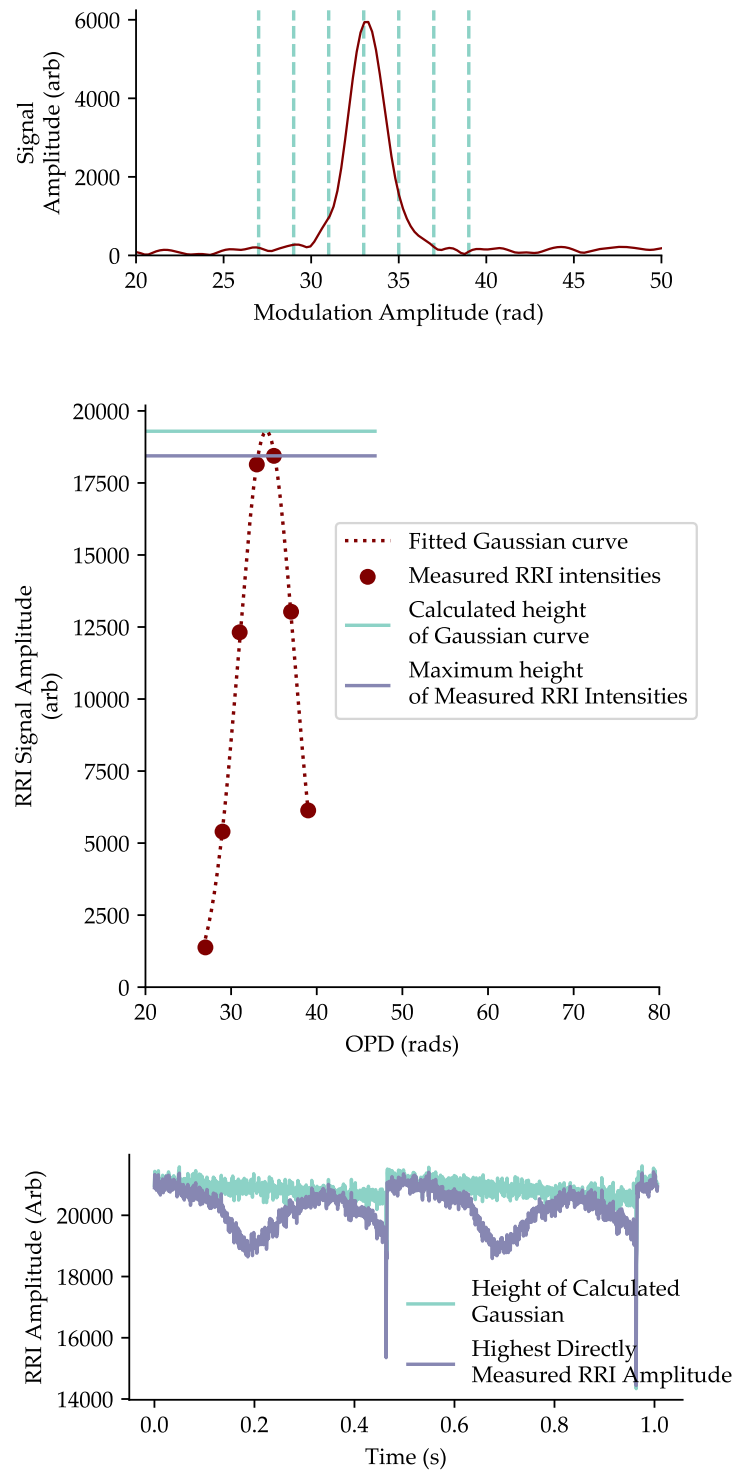
Figure 5.11: The process of getting from the measured RRI amplitudes produced by the interrogation system to a measure of light intensity as a function of time.
Step 1: Notional OPDs to interrogate each peak of interest are established.
Step 2: Each measurement channel provides a single RRI amplitude for each measurement interval. These are fitted to a Gaussian to allow the measurement of the height of a reconstructed curve
Step 3: The calculated peak height is then plotted as a function of time to produce a TDLS-like function. Taking just the highest value of the measured RRI amplitudes produces a non linear response over time.

Step 3 of Figure 5.11 shows the necessity of this extra step of fitting the individual measurements to a Gaussian peak and extracting the height. The grey line in step 3 shows the plot produced by plotting the maximum recorded RRI amplitude. At times the highest measured value of RRI amplitude is substantially lower than the calculated height of the reconstructed Gaussian curve, causing the undulating shape shown in Figure 5.9 By reconstructing the Gaussian peak, this is avoided and the resulting plot of recovered amplitudes vs time has the characteristic straight ramp quality of a TDLS measurement, examples of the different reported heights are shown in more detail in Figure 5.12.
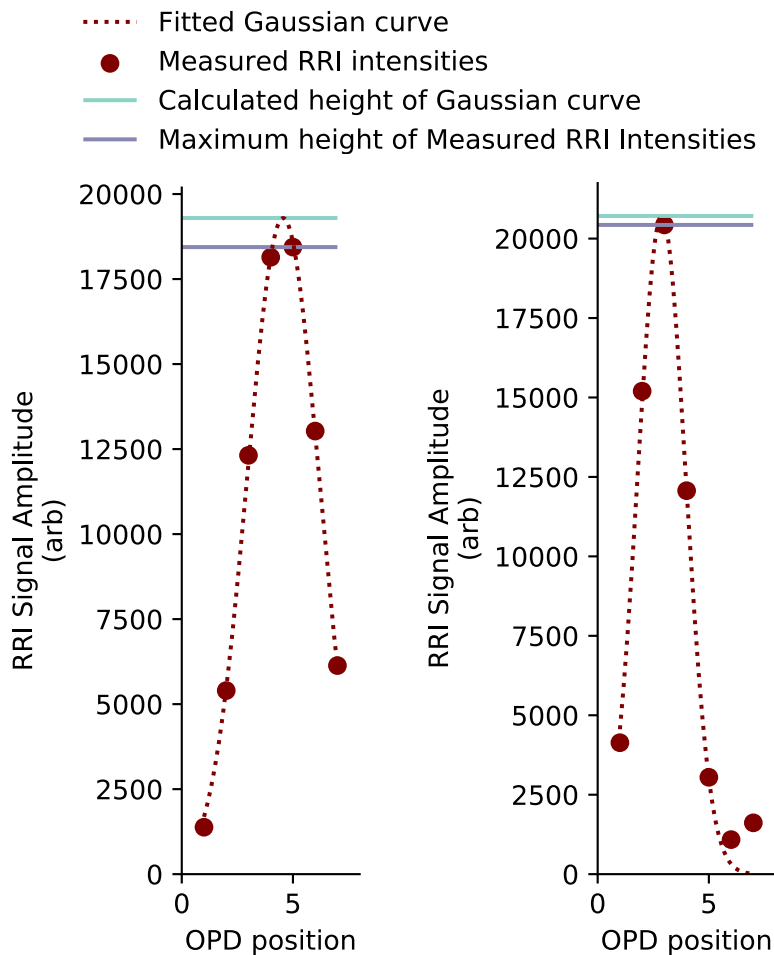
Figure 5.12: The effect of using the highest measured RRI amplitude, rather than fitting the measured leads to a lower value for the peak amplitude. The magnitude of this effect is time variant and leads to the undulating effect seen in Figure 5.11

The final result of the extraction of calculated RRI amplitude for the sensing region as a function of time over the full 1s period of the ramp modulation is shown in Figure 5.13. It should be noted here that for these measurements (and some others through this thesis) the instrument used to combine the ramp voltage sweep with the sine modulation was a voltage subtractor, rather than an adder as had previously been used. Consequently, the direction of the ramp applied to the laser driver is reversed.
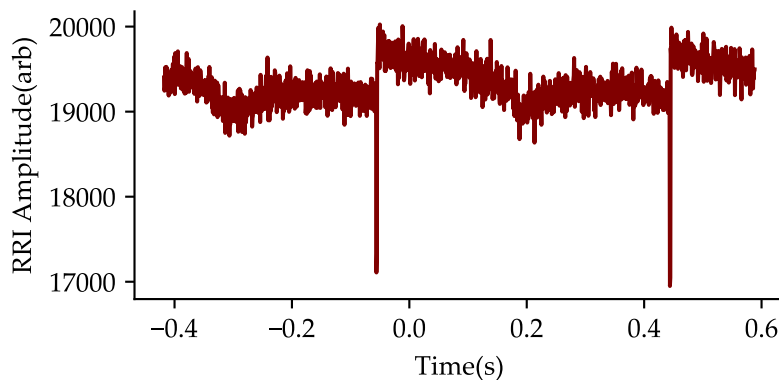
Figure 5.13: Extracted RRI Signal Amplitude As Function of Time. The start and end of the ramp modulations are again shown by the presence of the vertical flyback lines. The presence of 1000ppm methane is shown by the observed dip in the light intensity passing through.

While reconstructing the Gaussian peak and extracting the height removes the effect of the highest measures amplitude not always corresponding to the height of the peak itself, it comes at a cost. In order to extract the 1536 sets of 3 Gaussian peaks (1 per RRI modulation period) produced in a second's worth of measurement, takes approximately 120 seconds of processing time on a regular desktop PC. While this could potentially be improved with better coding, the need for post-processing is a fundamental problem with using the RRI system as designed for measuring the location of potential gas leaks in a gas sensing regime. The application of a new system designed to negate this need is described in Chapter 6, but the effectiveness of this post-processing system for gas

detection was investigated as a proof of concept for the technique of gas detection using RRI.

5.3.2 *Calculation of Gas Concentration*

Having produced a value for light intensity passing through each gas cell as a function of time, the next step is to use that to measure the concentration of gas present. As described in Section 2.4.2, the amplitude of an absorption curve is proportional to the concentration of gas under test and so the next step in the process is to extract this absorption curve from the data. This is achieved using another Python script. The ramp function used to sweep the laser output wavelength has a frequency of 2Hz, and in each measurement, data is taken for 1 second. In order to extract the 0.5s of data that corresponds to a single ramp period, the location of the flyback that occurs at approximately 0.32s in Figure 5.13 was found by calculating the difference between consecutive values of the RRI amplitude. The highest value of this difference was taken to be the flyback, which marks the start of the ramp modulation. If this value was found to occur before 0.5s, then 768 measurement points were taken starting from the flyback. If the flyback was found to occur after the 0.5s point, then all the data from that point until the end of the measurement were taken, along with enough data points from the start of measurement to make up a full 768 data points to cover one ramp modulation period, with the two sets of data points pasted together to form a whole ramp period. Finally, as in Equation 4.10, the RRI amplitude at each point is squared to produce a proxy measurement for the light intensity passing through each gas tube.

With a single ramp period of squared RRI amplitudes, hereinafter referred to as light intensity, the properties of any absorption feature (as seen in tube 1 in Figure 5.13) could then be extracted as follows. Portions of the light intensity data were taken from either end of the ramp modulation period. This was

then fitted to a straight line using the lmfit procedure[67] in Python. This fitted straight line was constructed from data points away from the absorption feature, and so when extrapolated over the whole of the scan, it produces the value I_0 in Equation 2.7. The light intensity over the whole range of the data is the I value in the same equation and so the normalised absorbance (A) can be calculated from Equation 5.2.

$$\frac{I_0 - I}{I_0} = A \tag{5.2}$$

The process is shown below in Figure 5.14
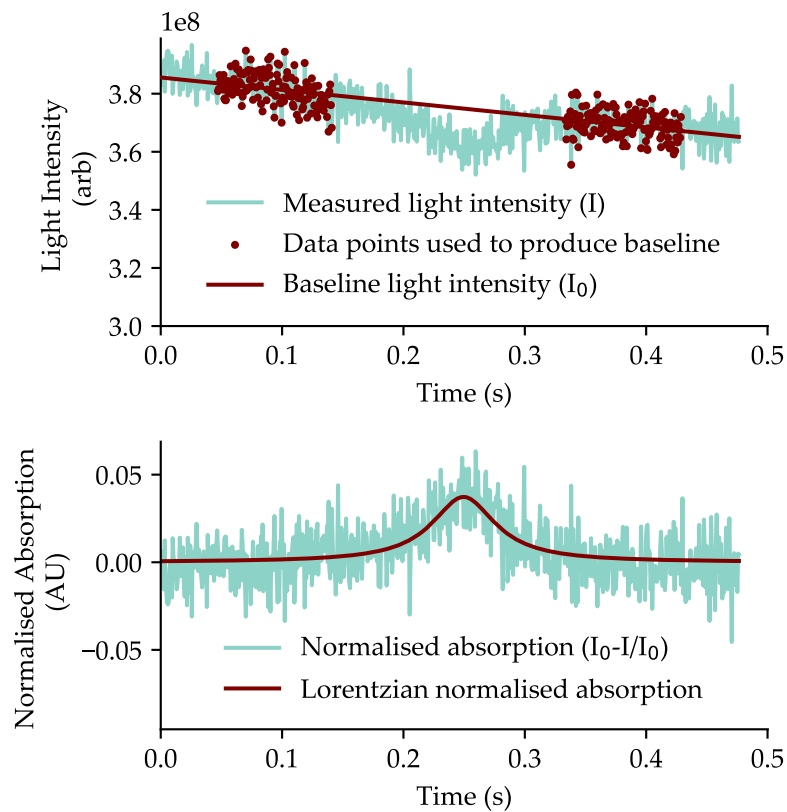
Figure 5.14: Top: The measured light intensity passing through a gas tube (I), the data points used to produce the baseline that shows the amount of light that would pass in the absence of absorption and the fitted baseline (I_0)
Bottom: The calculated normalised absorption (I_0-I)/I_0) and the Lorentzian line shape fitted to that absorption curve from which parameters such as height or amplitude can be extracted

This normalised absorption curve is then fitted to a Lorentzian using the lmfit procedure and its relevant parameters are extracted. Specifically, the height of the Lorentzian curve is extracted for gas concentration analysis along with some parameters related to the quality of the fit.

5.4   MULTIPOINT GAS DETECTION

The method described above allows for the extraction of the transmitted intensity through the sensing region, and thus the concentration of methane within that sensing region. The system, as used in these experiments, is used to measure 3 sensing regions simultaneously, and the following section describes the characterisation of its performance when measuring the concentration of gas within these sensing regions.

5.4.1   *Experimental Set Up*

5.4.1.1   *Equipment layout*

The equipment shown in Figure 5.15 was set up, with three gas cells that could be independently filled with gas of different concentrations. Succeeding each of the gas cells, single mode optical fibres of different lengths were placed so that the interferometers formed between the paths with the gas cells and the reference arm had different path differences, allowing them to be interrogated separately. The additional fibre lengths, and thus the OPDs between the sensing arms and the reference arms were 1,3 and 5m.
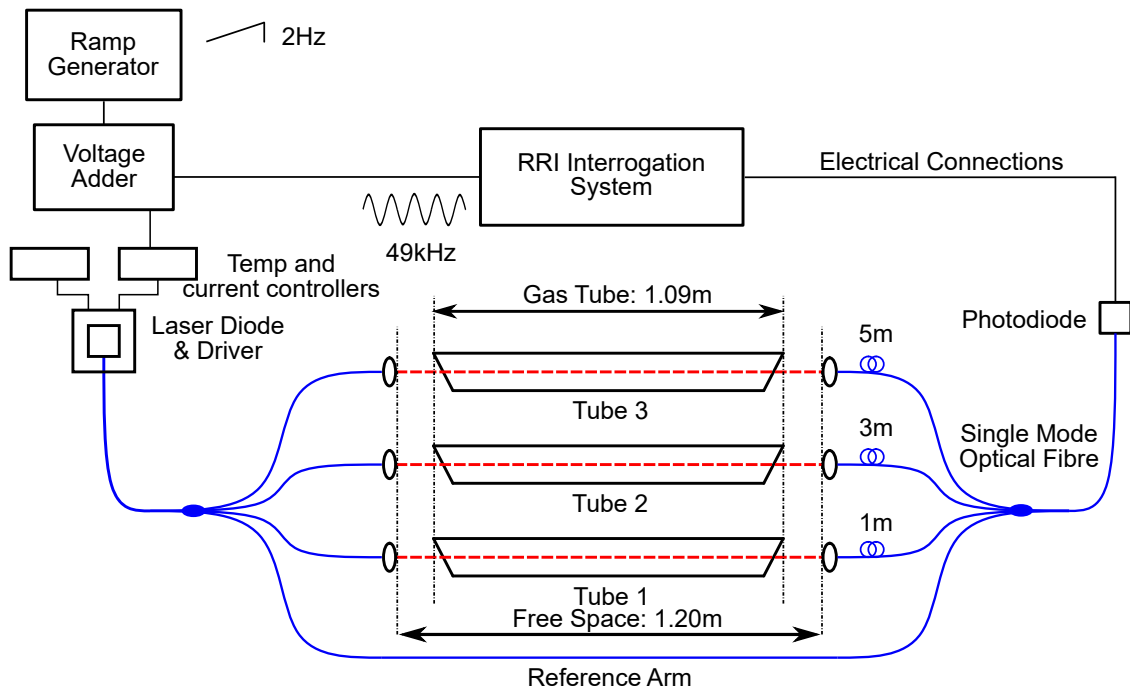
Figure 5.15: The equipment used to demonstrate the measurement of gas in three locations
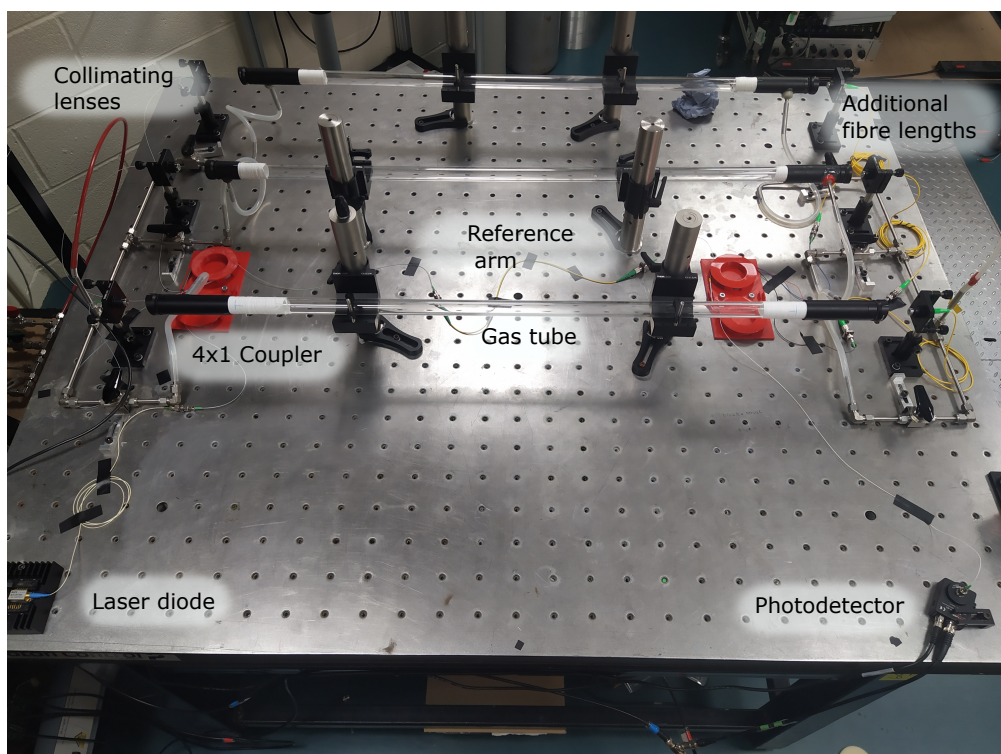
Figure 5.16: The equipment used to demonstrate the measurement of gas in three locations

In this iteration, when no ramp modulation was applied, the OPDs of interest were found to be at 40, 100, and 158 radians respectively. In order to capture the RRI amplitude as the RRI moved, each tube was interrogated at 7 notional OPDs around the OPD of interest. The OPDs of interest are not the only interferometers present within the system. As well as interferences between the gas tubes and the reference arm, there are also parasitic interferometers set up between the paths that pass between the combinations of gas tubes. These show up as extra peaks on the RRI amplitude map. The peaks of interest and spurious peaks can be theoretically differentiated by their location on the amplitude map, or practically by selective blocking of light in individual paths while noting which peaks remain present for which combinations of available interferometers. The RRI amplitude map of the system, along with the notional OPDs used for interrogation are shown in Figure 5.17.
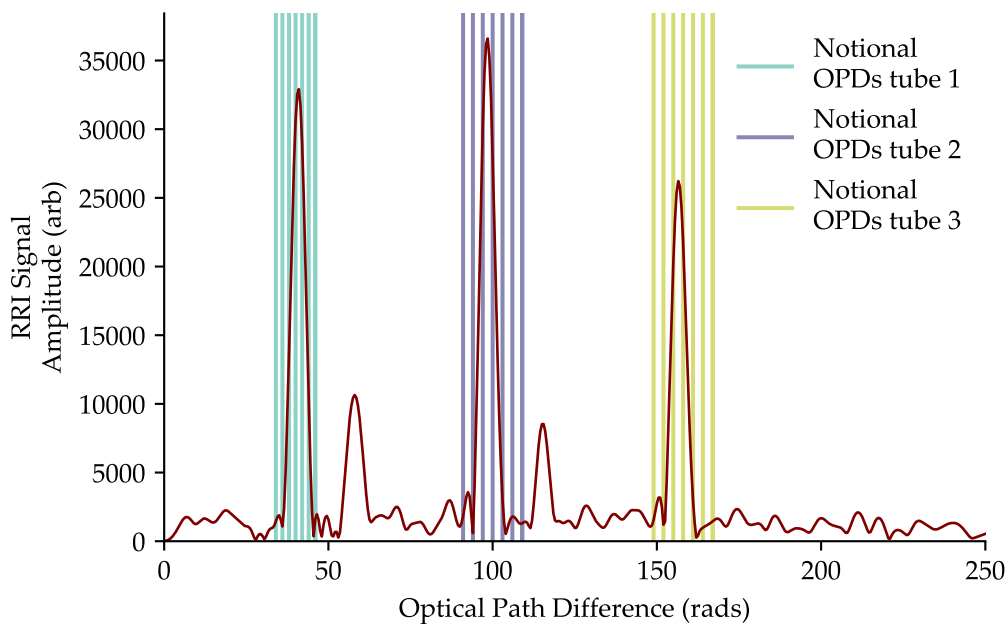
Figure 5.17: The RRI amplitude as a function of OPD for the system with three gas tubes, showing the peaks of interest formed by interference between the gas tubes and the reference line as well as the spurious peaks caused by intra-tube interferences. Also shown are the notional OPDs used for interrogation.

5.4.2 *Calibration*

In order to measure the response of the system to different concentrations of methane, a cylinder of synthetic hydrocarbon free air was connected to MFC1 (flow rate 0-1000ccm^{-1}), while a cylinder of 1000ppm was connected to the other MFCs, in turn, to provide varying mixed concentrations of methane to the gas tubes. Keeping the total flow rate at a value of 1000ccm^{-1}, the flow rate of the air and methane was adjusted to provide mixed concentrations of methane ranging from 0ppm to 1000ppm.

Once each cell was filled with equal concentrations of methane and closed, a series of ten measurements were taken in each tube at each concentration, repeated for multiple concentrations in the range 0-1000ppm. The data produced by the RRI interrogation system was then post-processed to produce the parameters of a Lorentzian curve for each measurement. The lmfit procedure, implemented in Python, produces a curve for all data sets it is provided with, even if a Lorentzian curve is not present in the data. As such, it can produce some false positives that need to be filtered from the data set. The output wavelength of the laser is set such that the centre of the absorption feature is at the centre of the ramp modulation and has been observed to be relatively stable over periods of hours. Using this information, and calculated absorption peak with a reported centre more than 25 points (out of the 763 total points, so about 3%) from the centre of the ramp was rejected from further calculations. Further, all calculated absorption peaks with a negative height were excluded. The remaining data was grouped by gas concentrations and the mean and standard error of the mean of each group was calculated and plotted below in Figure 5.18. As well as variations in the measured absorption height, there is also uncertainty in the supplied concentration of methane, coming from a combination of uncertainty in the composition of the supplied gases, and uncertainty in the flow rates allowed by the mass flow control system. However, this uncertainty in the gas

concentration present has been calculated to be lower than 0.25% of the calculated concentration and so is not visible in the plot.
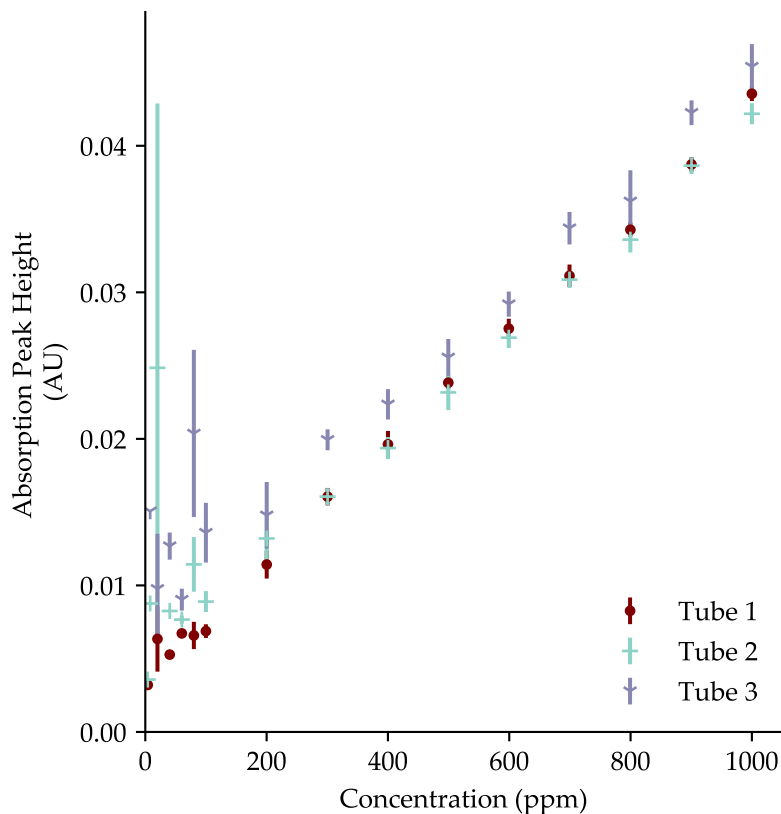
Figure 5.18: The effect of varying methane concentration in each gas cell on the calculated height of the associated absorption peak

While efforts were made to ensure that the gas tubes were identical, the measurements from the three tubes were different in a quite consistent manner. Even after normalisation, the absorption curves produced from readings in tube 3 had a consistently greater height than those of the other tubes. We would expect, in the absence of methane, the size of the absorption curve to be zero, and so for the response lines of each tube to pass through the origin, but they do not. It is possible that this offset is due to aspects in the curve fitting technique related to the baseline noise in the measurements (the average calculated height of peaks calculated in the absence of methane is of the same order of magnitude as the intercept value) but further work would be needed to support or reject this hy-

pothesis. However, we can calibrate this offset by fitting the concentration and mean absorption peak height data to a linear model and calculating the intercept of this fit and subtracting it from each value. After the subtraction of this intercept value from each measurement, the mean values were plotted again. The result of this process is shown below in Figure 5.19.
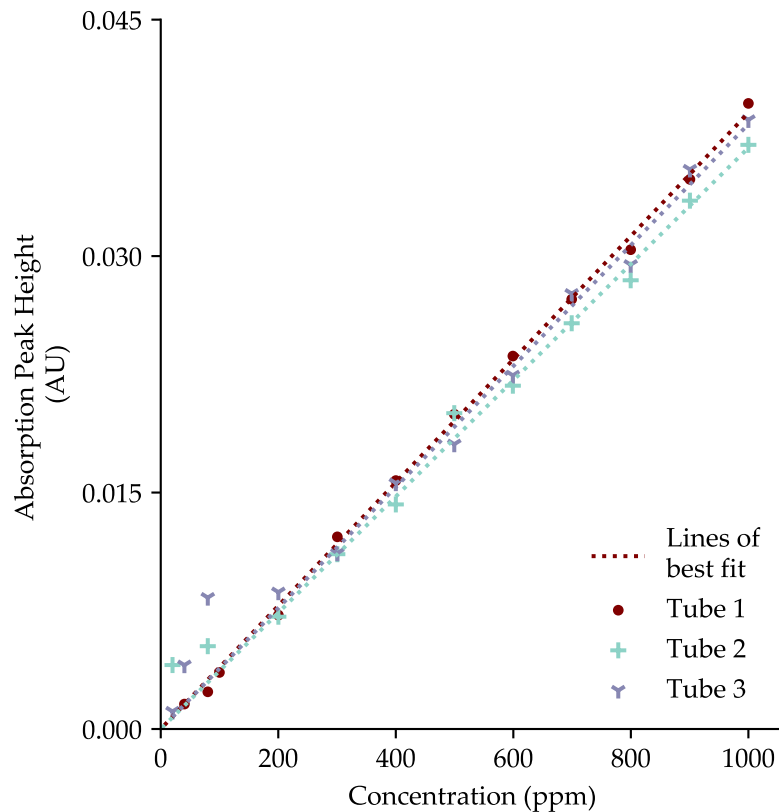
Figure 5.19: This shows the same data as Figure 5.18, but with the values calibrated such that the lines of best fit for each gas tube pass through the origin. This was achieved by subtracting a calibration factor for each tube from the measurements previously shown.

Figure 5.19 shows the three sets of results produce good linearity from concentration values greater than 200ppm. Using the results shown in Figure 5.19 this concentration range (200ppm-1000ppm) gives R^2 values of 0.99, 0.97 and 0.95 for tubes 1, 2 and 3 respectively. The line of best fit for each tube from the data in Figure 5.19 can then be used to convert a calculated absorption peak height into a measured gas concentration.

5.4.3 *Limit Of Detection*

As well as linearity of response, in instrument design and testing, it is useful to know the lowest level of methane the system can detect. This limit is a function of the signal to noise ratio and as a consequence can be improved by averaging. One method used to determine the limits of the effectiveness of this averaging is the Allan-Werle Deviation measurement[151]. In order to perform this test, a large number (k) of measurements of a system under stable conditions are taken at regular intervals producing values (x). These measurements are then arranged sequentially into a number of bins (N), with bin sizes ranging from 1 to the one half of the total number of measurements taken. The contents of the bins are then averaged, and the difference between the means of consecutive bins are taken and squared. These squared differences are then summed and normalised against 1/2N to produce an Allan-Werle variance ($\sigma^2_{(N)}$) for a given bin size, and thus averaging period. This is summarised in

$$\sigma^2_{(N)} = \frac{1}{2N} \sum_{i=1}^{N} (\bar{x}_{N+1} - \bar{x}_N)^2 \tag{5.3}$$

The averaging time (τ) is calculated by multiplying the length of one measurement period by the number of measurement periods in each bin size. Plotting this Allan-Werle Deviation against the averaging time shows the effect of different averaging periods on the signal to noise ratio of measurements and is shown below in Figure 5.20
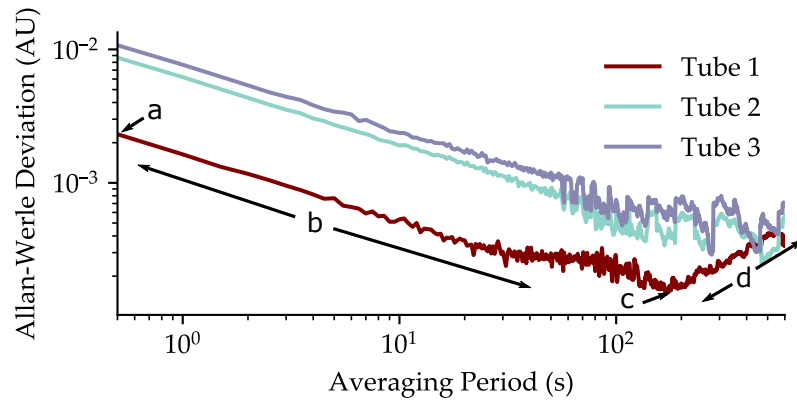
In

Figure 5.20: The Allan-Werle plot shows the effect of differing averaging times on the noise within the system. (a) gives the measure of the noise with no averaging. (b) is the region of averaging in which white noise dominates, with noise being lessened as averaging time increases (c) gives both the optimum averaging period for the system (169.5s) and the noise that would remain at that averaging period (1.5×10^{-4} AU). (d) marks the region of averaging times in which longer term instabilities (drift) dominate in the system

An Allan-Werle plot such as that shown in Figure 5.20 has a number of points of interest. Looking at the plot for the results taken from tube 1 as an example, 4 regions or points of interest can be identified. Point (a) shows the standard deviation of all the measurement points with no averaging. This is a measure of the signal to noise ratio of a single measurement. Region (b) shows the effect of increased levels of averaging with increased bin sizes. Over this region, the influence of high frequency noise is being reduced by this averaging until point (c) is reached. Point (c) marks the point at which averaging has the greatest effect on lowering the signal to noise ratio. As the averaging period increases in region (d) long period effects, known as drift, become dominant and so further averaging increases the signal to noise ratio.

In this experiment, position c shows that the optimum averaging period is 169.5 seconds or approximately 3 minutes. With this averaging period, the standard deviation of the sampling is 1.465×10^{-4} AU. As this is a theoretical value of an absorption peak height, we can use the the calibration chart (Figure 5.19, to calculate noise equivalent absorption of 3.77ppm. The measurements in tubes 2 & 3 have a greater high frequency noise component and so do not reach the

inflection point (d) (this is potentially due to their longer path lengths and so higher phase noise), but using the optimal averaging period of tube 1 for each of them, the visual inspection of Figure 5.19 gives noise equivalent concentrations of 11ppm & 16ppm respectively.

5.4.4 *Cross Talk Analysis*

In order to be useful as a multipoint detection system, it is necessary that each measurement location is sampled independently from the others. This is to avoid situations in which a gas leak is reported in the wrong location or in which the presence of gas in one location prevents the measurement of gas in another location. Thus, the presence or absence of gas in tube 2 or 3 should have no effect on the measured concentration of gas in tube 1. In order to test this, we investigated the effect of different concentrations of gas in tubes 2 & 3 on the reading taken with a constant concentration in gas tube 1. In order to test this, gas tube 1 was filled with 1000ppm methane using the method described above in Section 5.4.2. Tube 1 was then closed, while the other tubes with filled with the concentrations shown below in Table 5.1.

Table 5.1: The concentrations used for the experiments to determine the effect of cross talk on system measurements

	Methane concentrations in each tube (ppm)		
Experiment	Tube 1	Tube 2	Tube 3
1	1000	<0.1	<0.1
2	1000	<0.1	1000
3	1000	1000	<0.1
4	1000	1000	1000

Tubes 2 & 3 were then closed, and for each experiment, ten measurements of the absorption peak height from tube 1 were taken. The mean and standard error in the mean for these sets of ten measurements were plotted in Figure 5.21,

with the standard error acting as a measure of the uncertainty of the averaged reading.
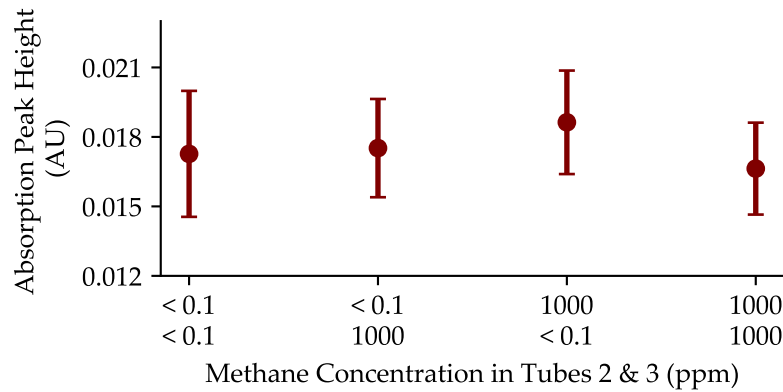
Figure 5.21: The measured absorption peak height in tube 1 is shown here to be independent of the presence or absence of methane in the other tubes.

Experiment 1 acted as a control test, showing the measurements taken from tube 1 when no methane was present in tube 2 or tube 3. Experiments 2 and 3 show the measurement taken from tube 1 when there is 1000ppm methane present in one of the other two tubes, and experiment 4 shows the measurements taken from tube 1 when 1000ppm is present in both tubes 2 and 3. The results in Figure 5.21 show that in experiments 2, 3 & 4 the average peak height measured in tube 1 lies within the uncertainty of the measurements in experiment 1. Consequently, we can say that the presence of methane in the other locations has no effect on the measurement of methane in tube 1.

5.5 SUMMARY

It has been shown that the application of Range Resolved Interferometry to a system in which gas tubes are coupled by fibre optics to a swept laser source and a detector allows the detection of the characteristic drop in light intensity associated with tunable diode laser spectroscopy. This is achieved by monitoring the amplitude of the signal associated with a given optical path difference

within an interferometer. However, due to non linearities in the laser response to modulation, the measured response is not the linear response one would expect. In order to obtain the linear response of TDLS, for each measured location, a number of OPDs must be simultaneously measured and the linear response reconstructed. This requires off-line signal processing, preventing the use of the system in this configuration in a real-time setting. In addition, there was no measurement made of the effect of polarisation changes on the measurement of the system. In order to keep the polarisation states as stable as possible and the visibility of the fringes as high as possible, the extra fibres within the sensing arms of the interferometers were positioned such that the RRI amplitude peaks associated with each interferometer of interest were as high as possible and then taped in position to prevent motion over the course of the experiments. However, as a proof of concept, some tests were performed to evaluate the response of the system to methane and its possible suitability as a multipoint methane detection system should the problems with signal processing be overcome. In its current configuration, the system has a linearity of response with an $R^2 \geqslant 0.95$ for methane concentrations above 200ppm making the system suitable for use as a methane measurement system. Allan-Werle deviation analysis of the system shows that there is the potential to measure concentrations as low as 3.8ppm given sufficient averaging time, allowing use at concentrations well below typical industry alarm levels. Finally, we were able to show that the presence of methane in other locations does not impact measurements in a given location, meaning that the system can reliably locate the location of methane concentrations.

TOWARDS A DEPLOYABLE SENSOR

6.1 INTRODUCTION

The results presented in Chapter 5 show the possibility of using RRI to detect the presence of methane. However, the experimental work has been done with a Mach-Zehnder interferometer configuration. While suitable for benchtop laboratory work, this arrangement would be impractical for field deployment as it would involve as many fibre paths as there are sensing units. To be more easily field deployable, a multiplexed gas sensing unit would ideally be available as a single, serially connected set of sensing units. To this end, two possible topologies are considered; a serial arrangement of sensing regions with partial reflectors placed between them to provide the different path lengths necessary for RRI, and a serial bus system with individual sensing regions coupled to a common backbone. These were chosen due to their simplicity and their potential for modular deployment. Each could be laid out in such a way that further sensing regions could be added to the end of an already deployed system with no major alterations to the current deployment required. In each case, a common oscillator path, similar to the common bypass line used in Section 5.2 are included. Each of the topologies will differ in terms of the light power that will be reflected back from the furthest sensing region. The losses involved depend on the losses and distributions caused by the reflectances, the coupling and the losses due to coupling inefficiencies into and out of the sensing regions. The following sections of this thesis will therefore compare the two proposed topolo-

gies with regard to the light intensity available for sensing at the furthest sensing region from the laser input.

6.2   POSSIBLE TOPOLOGIES

When deploying multiple connected sensors, the manner in which they are connected to the light source and the detector will have an impact on the light intensity that illuminates each sensor. This in turn will impact the signal-to-noise ratio and the sensing capabilities of each sensor. In this section, two possible arrangements or topologies of sensors will be examined.

6.2.1   *Serial*

In this topology, the gas sensing units are arranged serially with interspersed partial reflection points as in Figure 6.1. The reflection points provide the different path lengths of the sensing interferometer along with the common oscillator path (reference arm) shown.
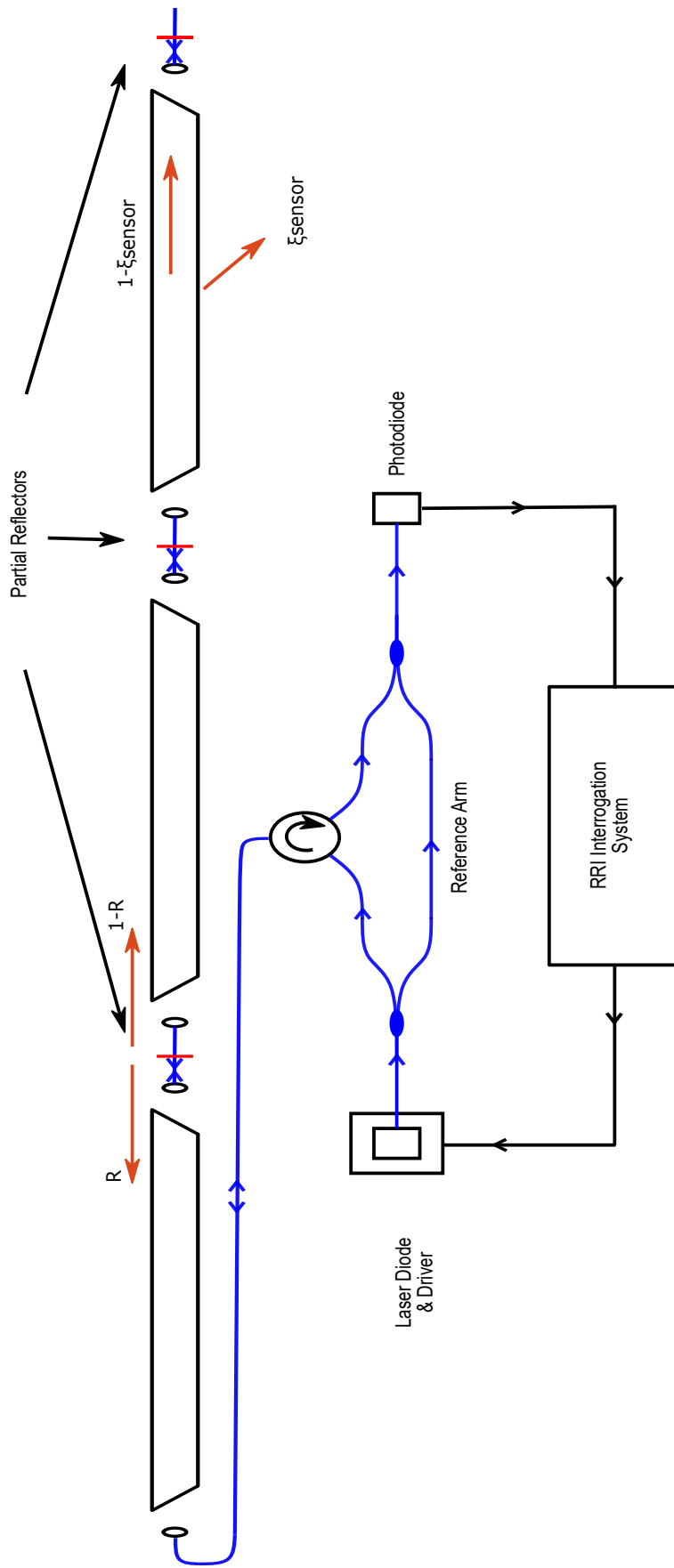
Figure 6.1: The proposed topology for a serial bus system of sensing regions showing the losses of light that reach each sensing region by way of coupling inefficiencies (ξ) and partial reflectances (R)

Light travelling through the sensing regions of the interferometer will be attenuated by the coupling in and out of the sensing regions (ξ_{sensor}), and by the partial reflectances (R). This attenuation effectively happens twice, once for the outward journey and once on the return path. For example, light reflected by the 3rd reflector will, by the time it is recoupled with the light passing through the local oscillator, have been attenuated by 6 coupling inefficiencies, the reflectance from the 1st and 2nd reflector and by passing through the 1st and 2nd reflector twice as shown in Figure 6.1. This can be generalised, and the light intensity returning from each interferometer (I) is given by Equation 6.1 wherein I_0 is the intensity of light in the sensing arm prior to any attenuation, ξ_{sensor} is the fractional loss of light intensity caused by coupling in and out of the sensing region, n is the number of gas sensing regions the light passes through, and R is the reflectivity of the chosen partial reflectors.

$$I = I_0(1 - \xi_{sensor})^{(2n)}(1 - R)^{2(n-1)}R \qquad (6.1)$$

Experimental work has shown that in the experiments described thus far, losses of approximately 60% have been experienced by light passing through the gas sensing regions in the absence of methane absorption. Using this as the value for ξ_{sensor}, the results of Equation 6.1 are plotted for sensors containing various numbers of sensing regions with various choices of reflectivity for the partial reflectors in Figure 6.2

Figure 6.2: The effect of different values of reflectance on the light returned from the final sensing region in a serial topology.

The ideal reflectance value for the partial reflectors (R_{ideal})(shown by the peaks of the curves in Figure 6.2) is dependent on the number of sensing regions (n) but independent of the attenuation within the sensing regions. It is determined by finding the values of R at which the first derivative of Equation 6.1 is equal to zero and is given by Equation 6.2.

$$R_{ideal} = \frac{1}{2n - 1} \tag{6.2}$$

replacing R by R_{ideal} in Equation 6.1 leads to Equation 6.3

$$I = I_0(1 - \xi_{sensor})^{(2n)} \left(1 - \frac{1}{2n-1}\right)^{2(n-1)} \left(\frac{1}{2n-1}\right) \tag{6.3}$$

Using the optimised values of reflectance for a given number of sensing regions, the light intensity returned from the last reflector in a system is plotted as a function of the coupling losses across the sensing region below in Figure 6.3.

Figure 6.3: The effect of coupling losses on the light returned from the final sensing region in serial topologies with different numbers of sensing regions.

The above work assumes that uniform reflectors are used throughout the sensing arm, but it would be possible to have different reflectances such that the reflectance of the partial reflector after the nth sensing region was a function of n. In general, this is beyond the scope of this thesis, but a single case can be noted wherein the reflectance of the final reflector be set to 1. As a result, all the light that reaches the final sensing region will be reflected back meaning that the light intensity associated with the final sensing region will be greater than that associated with the penultimate one. Thus, for light budget considerations, a system with n sensing regions can be analysed as if it were a system of n-1 sensing regions.

6.2.2 *Serial Bus Topology*

In this system, the sensing arm of the interferometer consists of a single fibre optic with the individual sensing regions coupled off from it in a branching configuration as shown by Figure 6.4. In this topology, the common oscillator is provided by the light reflected back from a terminal reflector This arrangement means that the furthest sensing region from the light source, while having the lowest light intensity, has the shortest optical path difference with the common

oscillator. This means that there is less potential for polarisation be-tween these two paths, which should lower the resultant noise in the amplitude of the resultant interferometric signal, compensating for the lower light intensity and thus lower signal in this sensing region. While in the serial configuration, the amount of light returning from any given sensing region was determined by the coupling losses in and out of the sensing region and the reflectance of the partial reflectors, in the topology shown in Figure 6.4 the light returning from the sensing regions is determined by the coupling losses (ξ) and the coupling ratio (Co)
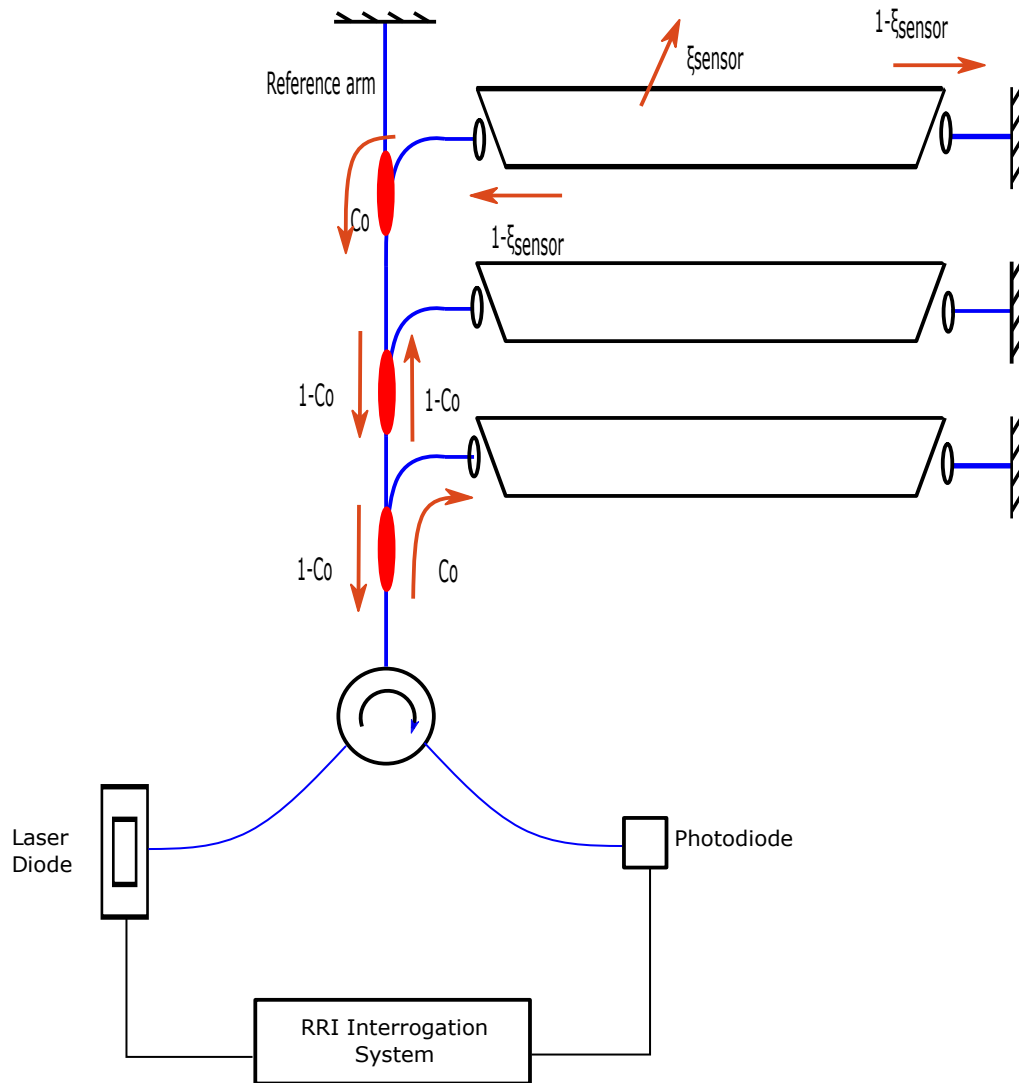
Figure 6.4: The proposed topology for a serial bus system of sensing regions. Showing the losses from the system due to coupler ratios (Co) and coupling inefficiencies (ξsensor)

In the case of this serial bus, the light reflected back from the third sensing region will have been attenuated by passing through the one side of a coupler 4 times, twice through the other side of a coupler and through the losses caused by inefficiencies of coupling through the actual sensing region. This is generalised so that the light intensity returning from the nth sensing region (I) is given by

Equation 6.4 wherein C_o is the coupler ratio, and ξ_{sensor} is the coupling inefficiency caused by coupling in and out of the sensing region.

$$I = I_0 C_o^2 (1 - \xi_{sensor})^2 (1 - C_o)^{2(n-1)} \tag{6.4}$$

Similarly to Section 6.2.1, using a value of 0.6 for the attenuation caused by passing through the sensing region, the results for Equation 6.4 are plotted in Figure 6.5 for sensors containing various numbers of sensing regions with varying choices of coupler ratios.
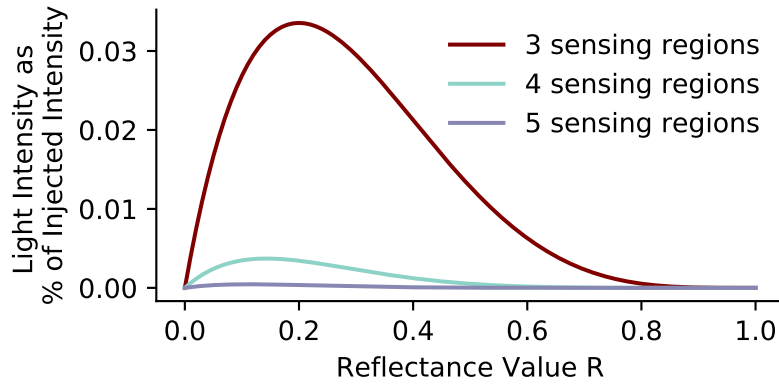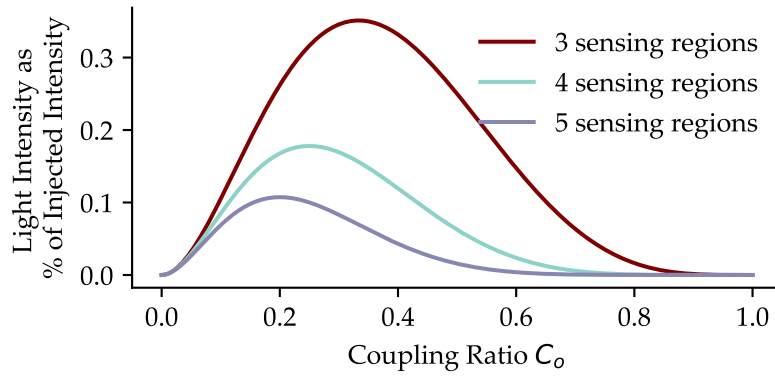

Figure 6.5: The effect of different values of coupling ratio on the light returned from the final sensing region in a serial bus topology.

Just as for Equation 6.2, the value for the optimal coupling ratio for a given number of sensing regions (n) can be evaluated and is given by C_{ideal} in Equation 6.5.

$$C_{ideal} = \frac{1}{n} \tag{6.5}$$

Using this ideal coupler ratio, Equation 6.4 can be written as Equation 6.6

$$I = I_0 \left(\frac{1}{n}\right)^2 (1 - \xi_{sensor})^2 \left(1 - \frac{1}{n}\right)^{2(n-1)} \tag{6.6}$$

Using the optimised value of coupler ratios for each system, the effect of the losses within the sensing region on the intensity of light returned from the final

sensor in the system can be calculated using equation Equation 6.4, and is shown in Figure 6.6.
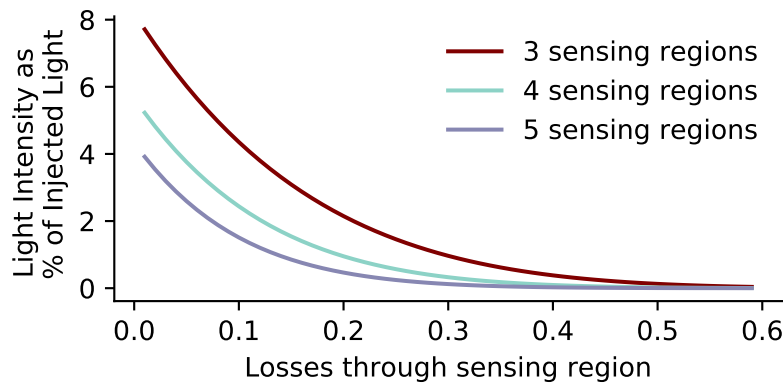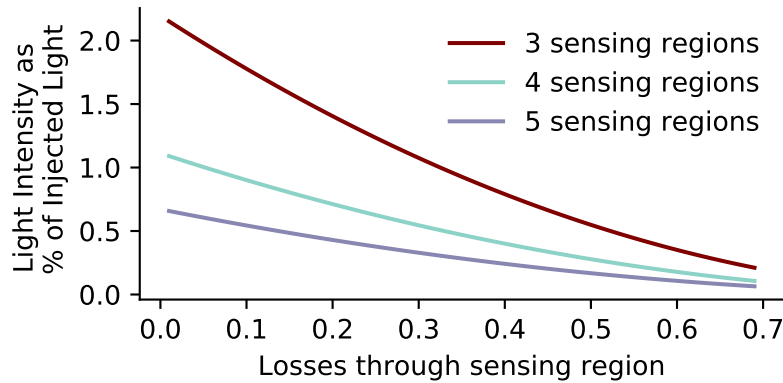

Figure 6.6: The effect of coupling losses on the light returned from the final sensing region in serial bus topologies with different numbers of sensing regions

6.2.2.1   *Choosing Between The Topologies*

Having seen the behaviour of the two topologies in sections Section 6.2.1 and Section 6.2.2 they can be compared and informed decisions made about deployment. For a selection of systems with differing numbers of sensing regions, the behaviours shown in Figure 6.2 and Figure 6.6 are shown for both topology types together in Figure 6.7 (assuming the use of the ideal coupler and reflectivity values for each system).
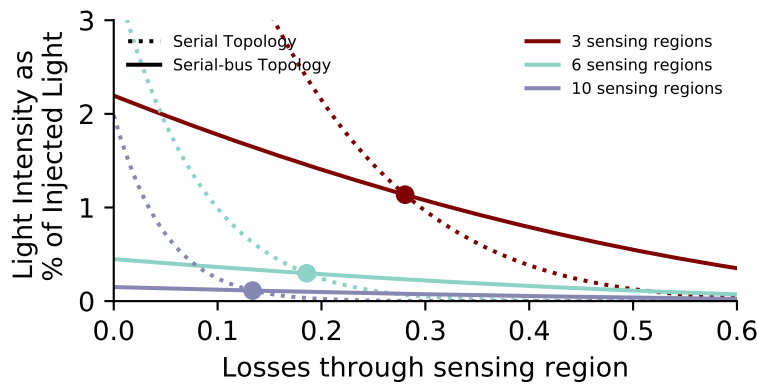
Figure 6.7: The light intensity returned from the final sensing region as a function of the sensor region coupling inefficiencies for sensors with different numbers of sensors. The point where the dotted line (serial topology) crosses the solid line (serial bus) shows the value of sensor region coupling inefficiency (ξ_{sensor}) at which the serial bus topology with that number of sensor regions is more efficient than the serial topology

This figure shows that for each value of n of sensing regions there is a value for the amount of attenuation within the sensing region at which the lines cross. This indicates the sensing loss attenuation value at which the serial bus topology returns more light to the photodiode than the serial topology. For example, in a system of three sensing units, if the loss within the sensing units is greater than 28% of the incident light, then the serial bus topology will return more light from the 3rd sensing region than would a three sensor system set up in a serial topology, while a loss of less than 28% would mean a serial topology would return more light from the final sensor. This 'crossover value' was calculated for systems containing differing numbers of sensing regions and is shown in Figure 6.8, which shows that for all losses within the sensor region greater than 15%, the serial bus topology allows a greater intensity of light to pass to the photodiode than the serial configuration with the same number of sensors, and that as more sensors are added the crossover value drops. This effect makes the deployment of a serial system unsuitable for any situations at which this saturation is possible and so the serial bus topology is a more realistic option in safety critical regimes.
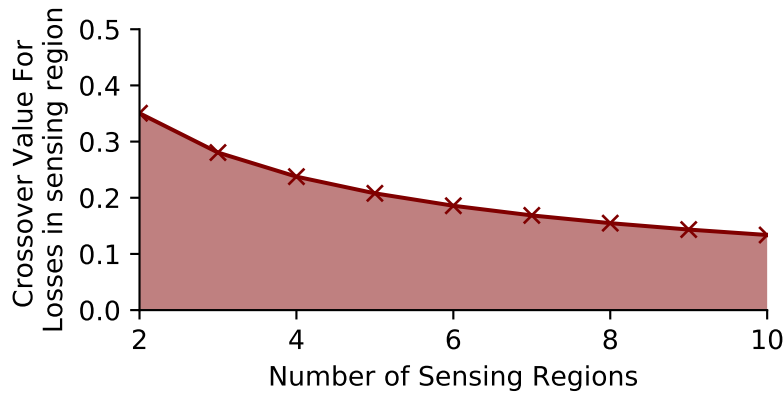
Figure 6.8: Assuming optimal coupling and reflectance values, this chart shows the coupling losses at which the serial bus topology returns more light than the serial topology. The red area shows the region in which the serial topology is more efficient

Thus far, we have only considered sensor region losses that are intrinsic to the system itself, rather than any losses that will be caused by the absorption of methane within the sensing regions. In order to be used in certain safety applications, a methane detection system has to be able to sense methane over the full concentration range from 0-100%[19]. The Beer-Lambert Law (Equation 2.7) along with the absorption coefficient of methane at 1651nm being $0.38atm^{-1}cm^{-1}$ in a 1m absorption thickness, gives a near 100% absorption of light. Thus, in the serial topology, any sensing regions beyond this point of light absorption saturation will be unusable. Other safety applications only require sensing capabilities over the concentration range from 0-5%[19] but even at 5% concentration, this would cause 85% of the light to be absorbed by each gas cell, reducing the signal-to-noise ratio in the downstream gas cells. As a consequence, it is unlikely that a serial topology would be a suitable way to deploy multiplexed gas sensors.

6.2.3 *signal-to-noise Ratio Measurements*

The effectiveness of each topology will depend on the signal-to-noise ratio of the signal from the furthest sensing region which will experience the greatest attenuation of light power as described in Section 6.2. Therefore, the effect of light attenuation on the SNR was investigated. Still using the Mach-Zehnder configuration, the arrangement shown in Figure 6.9 was investigated.
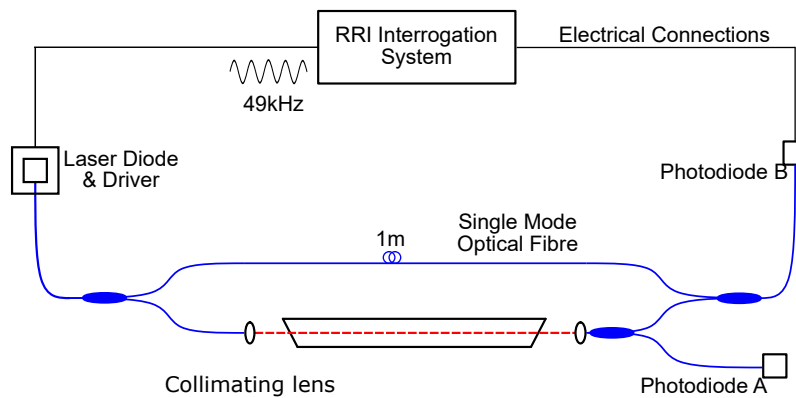
Figure 6.9: Light Budget Experiment Layout. A single two armed interferometer measured by two photodiodes.

The system was set up and aligned to allow the maximum coupling efficiency between the two collimating lenses. With no modulation applied to the laser, a measure of the mean voltage produced by photodiode A was taken over a one second period. This was then converted into a measure of the light power passing through the system and compared to a measure of the power that was emitted from the laser, which was measured separately. The RRI system was simultaneously employed to produce an RRI signal amplitude from the interferometric signal produced at photodiode B as in Section 5.2 although no ramping was applied and so no Gaussian peak reconstruction was needed. The mean value of the RRI amplitude was calculated as indicative of the signal amplitude in the system, and the standard deviation of the RRI amplitude was taken as a measure of noise within the system. From these, a signal-to-noise ratio was

calculated. The alignment of the collimating lenses was then adjusted so that less light was coupled through the system. The new average light power was calculated, and a new signal-to-noise ratio was calculated on an RRI amplitude measurement over a second of measurement. This signal-to-noise ratio was then plotted against the light power passing through the system as a percentage of the light power emitted by the laser ($\approx$5mW). This is shown below in Figure 6.10.
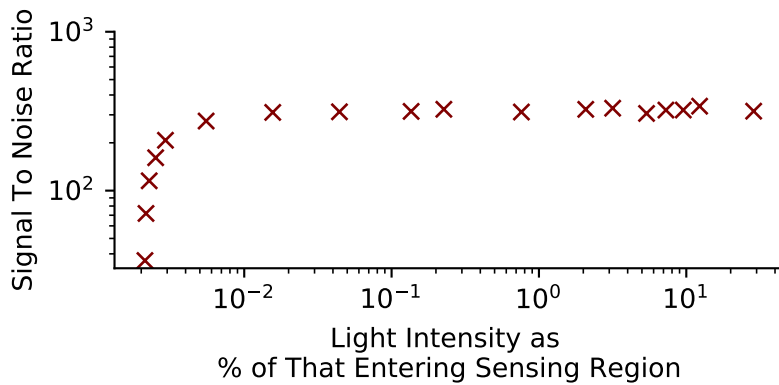
Figure 6.10: The SNR measured in as a function of the light intensity passing through the sensing region in Figure 6.9

Figure 6.10 shows that when the light power coupling through the sensing region is less than approximately 0.005% of the output, there is a steep drop in the signal-to-noise ratio as the light power continues to fall. However, if the light intensity coupled through the sensing region is increased beyond 0.02% there is no associated increase in signal-to-noise ratio, instead the ratio plateaus beyond this point. This experiment suggests that in order to avoid operating in the regime in which SNR rapidly drops, the light intensity returning from the final sensor region should be no less than 0.03% of the light intensity emitted from the laser diode used in this experiment. By reference to Equation 6.3 and Equation 6.6, it can be shown that to meet the desired criterion of >0.03% of the total intensity of the laser light being returned from the final sensing region, a system arranged in the serial topology can have a maximum of 3 sensing regions, while a system arranged in the serial-bus topology could have up to 13

sensing regions with the laser operated in the power regime of approximately 3mW investigated in this work. There is the possibility for a greater number of sensing regions to be interrogated by using a laser operating at higher powers or by reducing the losses associated with the coupling in and out of the sensing regions. The laser used in the experiments described here is capable of operating at powers of up to 10mW, meaning there is the possibility of trebling the number of sampling regions while staying on the SNR plateau. The existence of this SNR plateau suggests that in this power region, sources of noise other than laser intensity or sensor noise dominate. Previous work[128] has shown that increasing path lengths increase the noise within the system. While no work has been done within the context of this thesis to quantify this effect, this finding is borne out by the work in Chapter 5 wherein the sensing regions with the OPDs have worse signal-to-noise ratios as shown by the lower sensitivities of those sensing regions in Figure 5.20. In this light intensity regime, the dominant noise source is the phase noise caused by the finite linewidth of the laser output which is transduced into noise on the RRI amplitude due to changes in the phase carrier amplitude in Equation 4.4.

6.3 DEPLOYING THE SERIAL BUS TOPOLOGY

The work previously detailed in Section 6.2 suggests that the serial bus topology was the most suitable configuration for deployment in field applications. In order to test this arrangement, the experimental apparatus as shown in Figure 6.11 was put together. As described in Section 6.2.1, the common path is provided by the light reflected from the terminal reflector. The individual sensor regions branch from the main bus by way of 90:10 couplers with 10% of the light passing into the sensing region. While this ratio is not the ideal coupler ratio for a system of three sensing regions, it allowed the testing under less than ideal situations and would give results that would be more applicable to sensing systems with

larger numbers of sensing regions. The light is reflected back from the end of the gas tube by a prism retro-reflector. This is a change from the in fibre reflectors proposed in Figure 6.4, and was chosen for convenience. However, these retrore-flectors have an effect on the polarisation state of the light that they reflect. The nature of this effect depends on the part of the retroreflector that the light strikes on its way in[152]. No attempt was made to measure this, but it was considered that the system was stable enough for the effect to be constant over time and, as before, the position of the fibres connecting to the sensing regions were adjusted to produce the highest visibility and held in place using tape. As with the Mach-Zehnder topology, it is necessary to carefully arrange the various OPDs of the constituent interferometers within the system. This is achieved by the insertion of various lengths of fibre (Lx1-Lx3) marked in red in the diagram.
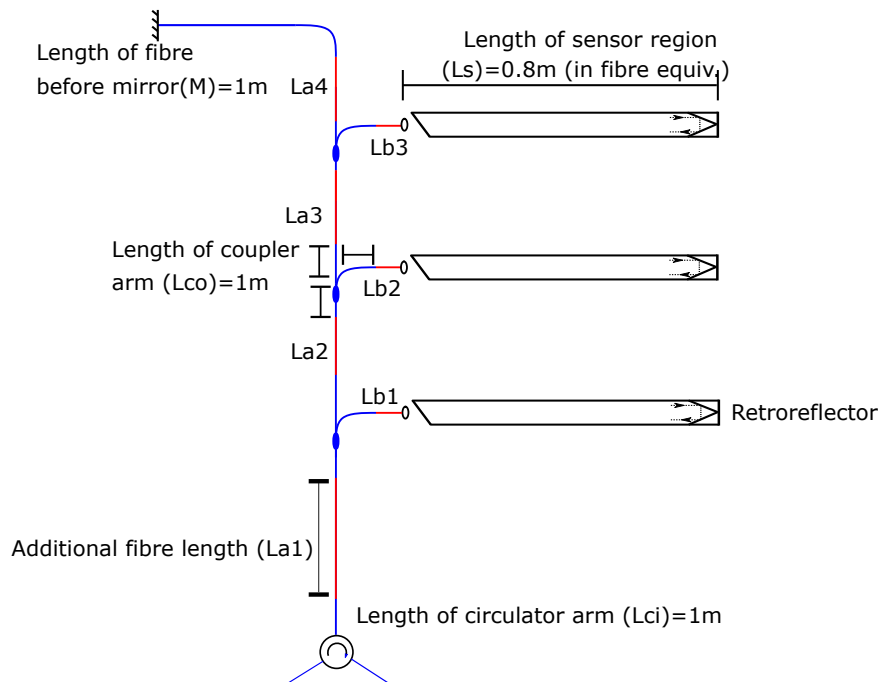
Figure 6.11: A universal serial bus topology showing the ability to alter the OPDs by adjusting the lengths of fibre (La, Lb) within the system.

The arms of the couplers were approximately 1m long, there was approximately 1m of fibre before the reflection point in the terminal reflector and each arm of the circulator is 1m long. The additional lengths of fibre within the back-

bone of the bus topology are labelled as La, while the additional fibre in the branches are labelled as Lb. The sensing regions are all 1.2m in length, which given the refractive index of silica is equivalent to 0.8m in fibre.

Sensing Region	Path of Light	Simplified Path Length
A	$4L_{ci}+4L_{co}+ 2La1+2Lb1+2Ls$	$9.6+2*(La1+Lb2)$
B	$4L_{ci}+8L_{co}+2La1+2La2$ $+2Lb2+2Ls$	$13.6+2*(La1+La2+Lb2)$
C	$4L_{ci}+12L_{co}+2La1+2La2$ $+2La3+2Lb3 +2Ls$	$17.6+2*(La1+La2+La3+Lb3)$
Common	$4L_{ci}+12L_{co}+2La1+2La2+2La3$ $+2La4+2M$	$18+2*(La1+La2+La3+La4)$

Table 6.1: The path travelled by light illuminating each part of the interferometer, and the simplified path lengths as functions of the lengths of the sections shown in Figure 6.11.

Table 6.1 describes all the possible path lengths for a system as in Figure 6.11. In the following experiments, however, no extra path lengths (La & Lb) were added, so the sensing region path lengths were 9.6m, 13.6m, and 17.6m. Thus, the OPDs that exist between these paths will be 4m and 8m. Therefore, for the OPDs of interest to be properly spaced from these parasitic interferometers, the OPDs of interest should be at 6m, 10m and 14m. This produces the largest possible spacing between the parasitic OPDs and the OPDs of interest. When such a system was put together and interrogated by RRI, the RRI amplitude map shown below in Figure 6.12 was generated. The positioning of the RRI amplitude peaks is such that a similar arrangement could be expanded to a larger number of sensing regions with parasitic interferometer OPDs remaining situated between the OPDs of interest.
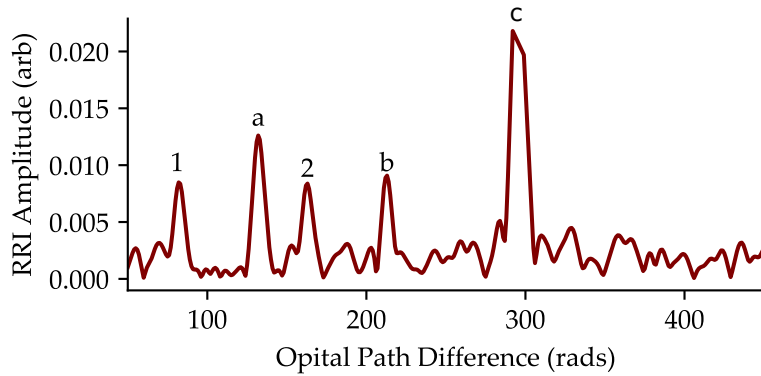
Figure 6.12: An RRI amplitude map produced by the interrogation of the chosen topology. The peaks labelled a, b & c are those of interest formed by the interactions between light in the sensing regions and the common local oscillator. Those labelled 1 and 2 are the parasitic peaks caused by interferences between the sensing regions.

A ramp modulation was then added to the RRI modulation and the RRI amplitude of the three interferometers of interest over the period of the sweep were calculated as before. The resulting RRI amplitudes are shown below in Figure 6.13.
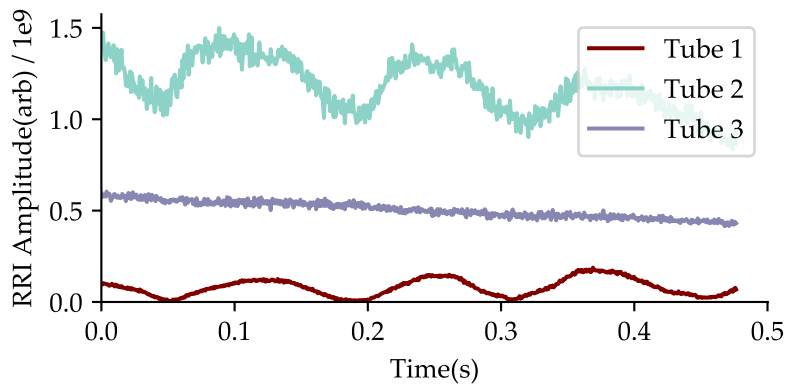
Figure 6.13: The RRI amplitudes measured when a ramp is applied to the serial bus topology system as shown in Figure 6.11

As is shown in Figure 6.13, the recovered TDLS-like plots show the existence of interference that prevents them from being straight lines. This interference had been seen before in earlier, unrecorded iterations of experiments using the Mach-Zehnder configuration and was the driving factor in the choice of path lengths used in that configuration. The chosen OPDs in Chapter 5 were those

at which this previously observed interference was not present. The fact that changing the OPDs was previously able to remove this interference shows that it was not due to physical reflections in the lightpath causing optical fringing but down to interactions between the interferometers themselves. The process by which this can happen is illustrated in Figure 6.14. To show the effect of the parasitic OPDs on the measurement of one of the OPDs of interest, a system as in Figure 6.15 was investigated.
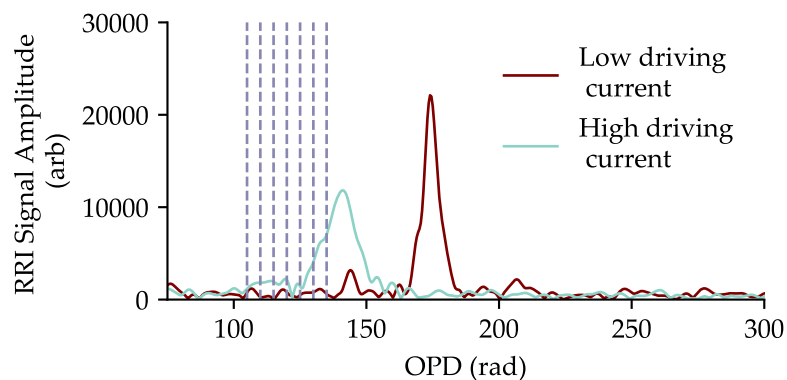
Figure 6.14: The motion of an RRI amplitude peak due to change in driving current. Showing the position of the parasitic RRI amplitude peak at high and low driving crurrent (red and blue) and the OPDs used to investigate an interferometer of interest (grey)
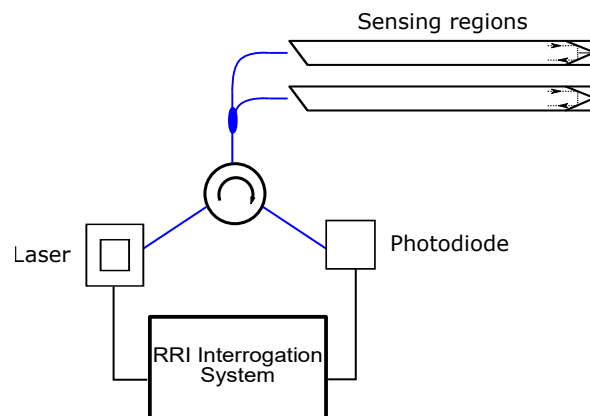
Figure 6.15: The experimental layout used to demonstrate the interaction between the interferometric signals of two sensing regions. The only interferometer formed is that between the light reflected from the ends of the two sensing regions.

In this experimental set-up, the only interferometer formed is that between the light reflected from the end of the two sensing regions, which is a parasitic

interferometer, rather than one of interest. This forms the peak labelled as (a) in Figure 6.12. The ramp modulation on the laser, the centre wavelength was adjusted from its initial position (producing the blue peak in Figure 6.14) to a wavelength corresponding to a lower point on the ramp modulation (producing the blue peak). As can be seen in Figure 6.14, the RRI amplitude peak associated with the parasitic interferometer moves so that it is within the region marked by the OPDs that are interrogated to reconstruct the OPD associated with sensing region 3 (indicated by the vertical dashed lines). This means that any reconstruction of the RRI amplitude peak associated with sensing region 3 will be incorrect, given that it will not be reconstructing a single RRI amplitude peak but various combinations of the two peaks as they move across the region being sampled.

In order to prevent this interference between OPDs, it is possible to adjust the spacing between the OPDs so that as they move, there is sufficient difference between each one that they do not interfere in this way. However, while this was possible in the earlier experiments in the Mach-Zehnder configuration with a limited number of sensing regions, application of this to a system with many sensing regions would be impractical. As the OPDs of the constituent interferometers are increased, as would be the case with larger numbers of sensing regions, the apparent motion of the peaks increases. This dependence of apparent RRI amplitude peak motion on OPD is shown in Figure 6.16, which was plotted by measuring the apparent motion of the RRI amplitude peaks over a single ramp modulation in a Mach-Zehnder interferometer with varying OPDs. In order to measure this, systems of single interferometers were constructed and the RRI amplitude maps were examined to identify the location of the peak when a constant central driving current was applied to the laser. This driving current was changed to a value corresponding to the highest central wavelength of the ramp modulation, and the lowest. This was repeated multiple times for each interferometer and an average of the shift in RRI amplitude peak position was calculated, along with a standard deviation for each.
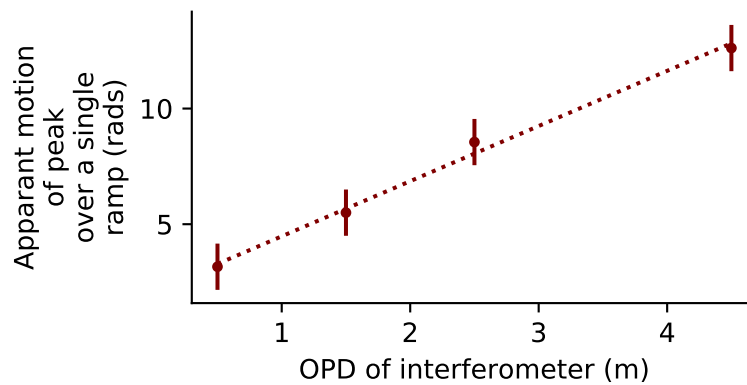
Figure 6.16: Apparent motion of RRI amplitude peak as a function of OPD.

As the magnitude of this apparent motion increases, in order to prevent the peaks crossing over the regions in which other peaks are measured, greater separation between the peaks will be needed. This can only be achieved by increased OPDs, and so increased path lengths of fibre, which will in turn lead to higher levels of noise as result of the phase noise of the laser. While this effect of fibre length on signal-to-noise ratio was not quantified, it will reduce the limit of detection of the device, as was seen in Section 5.4.3 As a result, this is not a practical solution, and so an alternative had to be found.

6.4 PREVENTION OF RRI AMPLITUDE PEAK MOTION

6.4.1 *The source of RRI amplitude peak Motion*

During Range Resolved Interferometric demodulation of a photodiode signal, the RRI system multiplies the photodiode signal by a Gaussian window and by a complex demodulation signal that is the interferometric signal that would be expected to be formed by an interferometer with given parameters, specifically of a given OPD. The result of this multiplication is a complex number, the magnitude of which is proportional to the amplitude of the portion of the total photodiode signal that is provided by an interferometer with the same parameters as the

demodulation signal. The equation used to produce the demodulation signal is first stated in Equation 4.6, and is repeated here for convenience as Equation 6.7, wherein A_d is the demodulation phase carrier amplitude, ω_m is the frequency at which the phase is modulated and τ_d is the a factor that is approximately half the time of flight delay for the light travelling down the two arms of the notional interferometer.

$$C(t) = e^{iA_d \sin(\omega_m(t - t_s p - 0.5\tau_d))} \tag{6.7}$$

The function A_d, which has units of radians, is chosen, either as part of a swept measurement of all values of A_d within a range for the production of an RRI amplitude map or at a set value for interrogation of a particular notional OPD. As such it can be interpreted as containing similar information about the notional interferometer as the phase carrier amplitude in Equation 4.5, again repeated here for convenience as Equation 6.8

$$A_n = \frac{2\pi\Delta f_{opt}\eta_k}{c_0} \tag{6.8}$$

In this equation, η_k is the OPD of the kth notional interferometer, and Δf_{opt} is the output frequency range over which the laser is modulated. This range is determined by the magnitude of the modulating driving current applied to the laser by the RRI system, and is considered during the demodulation process to be constant. As a result, the phase modulation amplitude is only a function of η_k, the OPD of the system. In previous implementations of RRI, this assumption was valid as the only modulation of the laser was the sinusoidal RRI modulation. However, the application of the ramp modulation makes this assumption invalid as will be shown in the next section of this text.

6.4.1.1 *Measurement of Optical Wavelength Modulation*

As discussed before in Section 4.4, the process of measuring the amplitude of an RRI signal at a given notional OPD is achieved by comparison of a superposition of interferometric signals and extracting the magnitude of the portion of that signal that is equivalent to the signal that would be produced by an interferometer of a given phase modulation amplitude. In previous applications of RRI, that phase modulation amplitude (A_n) is proportional to the OPD of the interferometer itself and so each unique OPD of the combined interferometers is equivalent to a unique value of this phase modulation amplitude. However, looking at Equation 6.8 shows that this is only true if the output wavelength range ($\Delta\lambda_{opt}$) remains constant. If this value changes, then, even as the OPD remains constant, the value of A_n will change. As a result, the value of the magnitude of the product of the interferometric signal ($U(t)$) and the complex carrier signal($C(t)$) will reduce as the notional interferometer signal will have different parameters to the actual interferometer signal being measured. As a first step towards mitigation of this effect, the change in the value of Δf_{opt} needs to be measured.

In order to measure $\Delta\lambda_{opt}$ as a function of the central wavelength, the laser fibre output was connected to a Yokagawa optical spectrum analyser (OSA). The driving current applied to the laser was set, in the absence of modulation to various points along the ramp used to sweep the laser wavelength across the gas absorption feature. A signal generator was then used to apply a sinusoidal modulation to the current driver at a frequency of 49kHz, which is the same as that produced by the RRI system, and with an amplitude of 500mV, which is approximately double the amplitude of the driving voltage of the RRI system as used in this thesis. This amplitude was chosen to amplify the effect of the modulation making it measurable using available equipment. In the absence of modulation, the OSA recorded a Gaussian profile for the laser emission, but,

upon application of modulation, the output of the OSA changed. An example of the new profile of the laser is shown below in Figure 6.17.
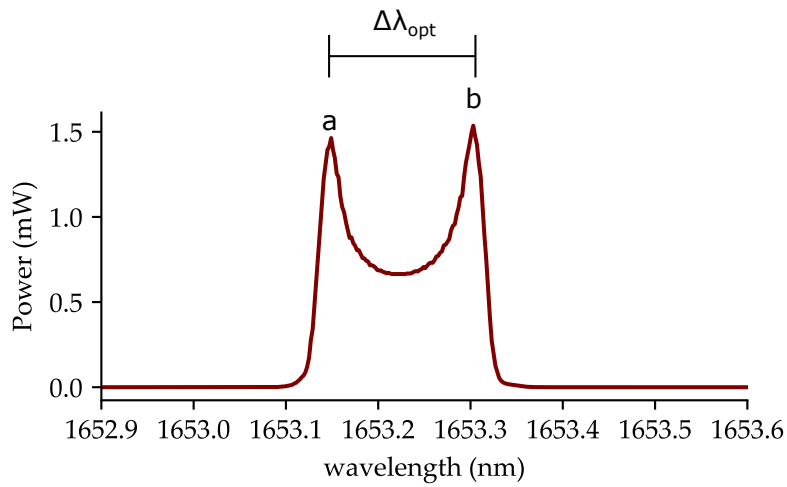
Figure 6.17: The power spectrum of the laser undergoing 49kHz, 500mV modulation, a and b mark the positions of the peaks used as a proxy for the value of the wavelength modulation of the laser ($\Delta\Lambda$)

The OSA trace was measured over a large number of modulations periods and maps the average intensity at each wavelength. As the laser was driven sinusoidally, the resulting behaviour was simple harmonic motion in the wavelength space and the height of the peak at each wavelength was a function of the time the laser spends at each wavelength and the power of the laser at each point. Hence the existence of the two peaks labelled a and b in Figure 6.17 where the rate of change of wavelength was lowest (peak b is higher than peak a because the laser has a higher power at that point). The separation between the peaks was measured and used as a proxy for the wavelength excursion ($\Delta\lambda_{opt}$) as in Equation 6.8. With a central driving current of 179mA applied to the laser, the amplitude of the current modulation was changed, and the peak separation was measured to check that the separation was proportional to the current modulation. This proportionality is shown below in Figure 6.18.
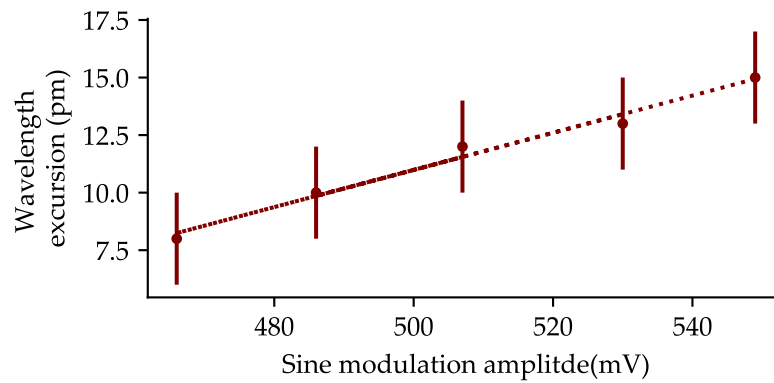
Figure 6.18: The measured difference between the frequencies of the two peaks in Figure 6.17, as a function of the applied sinusoidal modulation, the uncertainty being given by the resolution of the OSA used.A line of best fit shows the linearity of the response

This proportionality gives confidence that while the OSA is unable to resolve the peak separation caused by modulations at the amplitude used within the system described in this thesis (approximately 250mV), the findings of measurements at higher modulations amplitudes will be applicable to the system as used.

The current controller was used to set the central DC driving current of the laser at various currents that corresponded to various points on the ramp current applied when the laser was swept in previous work. At each central driving current, a 500mV 49kHz modulation was applied, and the OSA was used to measure the optical wavelength excursion ($\Delta\lambda_{opt}$) as shown in Figure 6.17. This optical wavelength excursion was plotted as a function of the central driving current in Figure 6.18
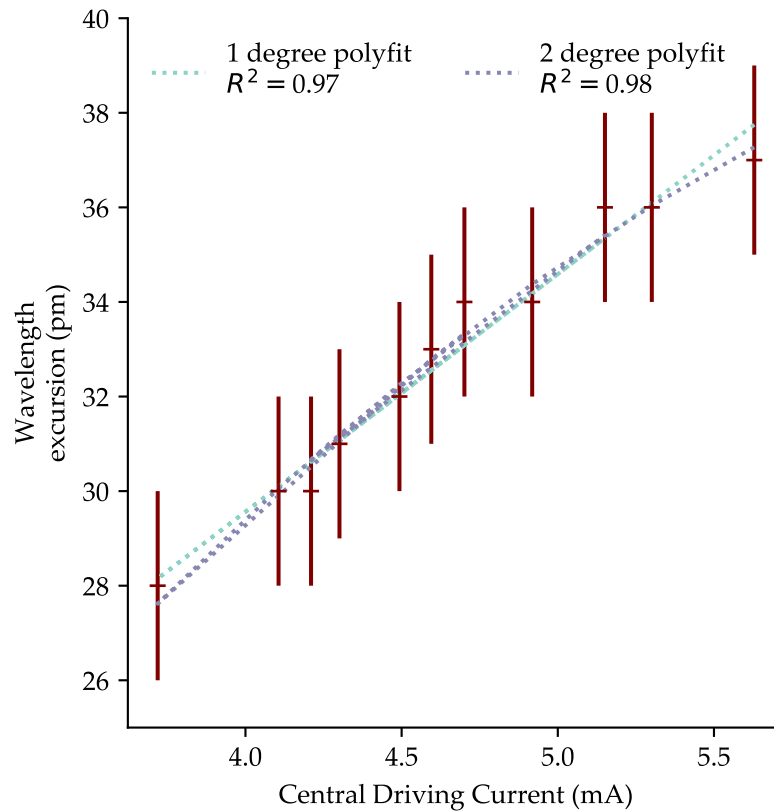
Figure 6.19: The measured difference between the wavelength of the two peaks in Figure 6.17, as a function of the central driving current

Figure 6.19 shows that the wavelength excursion varies by a factor of approximately 25% over the period of a single ramp modulation. However, given the apparent noise within the measurements (possibly caused by a lack of resolution on the OSA combined with the use of the two peaks in Figure 6.17 as a measure of $\Delta\lambda_{opt}$ rather than a more precise measurement such as the use of a Fabry-Perot interferometer) means that the actual relationship between the central driving current and $\Delta\lambda_{opt}$ cannot be precisely determined. Both a 1st and 2nd degree polynomial fit to the data are shown on Figure 6.18, and both have similar coefficients of determination.

Having determined the effect and the underlying cause of the motion of the peaks, there exist two possible solutions and these will be discussed in the next section of this thesis.

6.4.2 *Methods to Prevent The Motion of RRI Amplitude Peaks*

The apparent motion of the RRI amplitude peaks described in Section 6.3 and thus the interference between the measurement channels is caused by the fact that at different central driving currents, the laser used in this work has different behaviours when a modulation is applied on top of the driving current. As a result, the phase modulation amplitude (A_k) as given most recently by Equation 6.7 becomes a function of the central driving current applied to the laser as well as the OPD of the interferometer. This in turn causes a mismatch between the demodulation complex interferometer signal and the measured signal causing a loss of the signal when demodulated at a fixed notional OPD.

In Chapter 5, this problem was mitigated by simultaneously demodulating the signal at 7 OPDs per measurement channel, thus capturing the signal as the RRI amplitude peak moved in phase space, and rebuilding the RRI amplitude curve at each instant in post-processing. While this was suitable for demonstrating the potential of RRI to measure gas concentration, the lack of real-time measurement means that it is not an appropriate method for deployment as a safety critical gas detector. Further, the motion of the RRI amplitude peaks into regions that contain RRI amplitude peaks associated with other sensing regions means that even a real-time system based on multiple notional OPDs per sensing region would be unfeasible. Therefore an alternative system of mitigation needs to be used.

The calculation of the RRI amplitude at any point is determined by the multiplication of a complex demodulation signal and the measured interferometer signal. In the system as currently deployed, the complex demodulation signal is kept constant, while the measured interferometer signal is a function of time. In order to avoid mismatch between the two, it would be possible to adjust either the applied demodulation signal, or to adjust the modulation on the laser and thus the measured interferometer signal. Both would be mathematically equiva-

lent, but for the purposes of simplicity of implementation it was decided to work towards a system wherein the wavelength excursion ($\Delta\lambda_{opt}$) is kept constant. This is similar to problems faced in speckle interferometry where modulation preshaping was used to mitigate nonlinear laser response to current[153, 154].

Figure 6.18 shows that the value of $\Delta\lambda_{opt}$ is proportional to the amplitude of the sinusoidal voltage modulation A_{sm}. At the same time, Figure 6.19 shows that it is possible to model the response of $\Delta\lambda_{opt}$ as a 1st or 2nd order polynomial function of the central driving current I_D. Consequently, the value of $\Delta\lambda_{opt}$ can be modelled by an equation of the form of Equation 6.9 where q_t is a polynomial function of time that can be derived from Figure 6.19 and a is a constant that connects the sinusoidal voltage to the wavelength modulation of the laser. It is possible to have q be a function of t, rather than the central driving current, as in a single ramp, the current is a linear function of time.

$$\Delta\lambda_{opt} \propto aA_{sm}q_{(t)} \tag{6.9}$$

In order for the RRI amplitude peak to be stationary and for $\Delta\lambda_{opt}$ to be a constant, a function of time $P_{(t)}$ needs to be found such that $q_{(t)}P_{(t)} = 1$. Multiplying the sinusoidal modulation by this function $P_{(t)}$ will adjust the amplitude of the sinusoidal modulation as a function of time, to counter the effect of the rising central driving current and keep the value of Δf_{opt} constant across the ramp. An example of one such potential modulation program, with arbitrary values for the modulations and the enveloping function is shown in Figure 6.20.
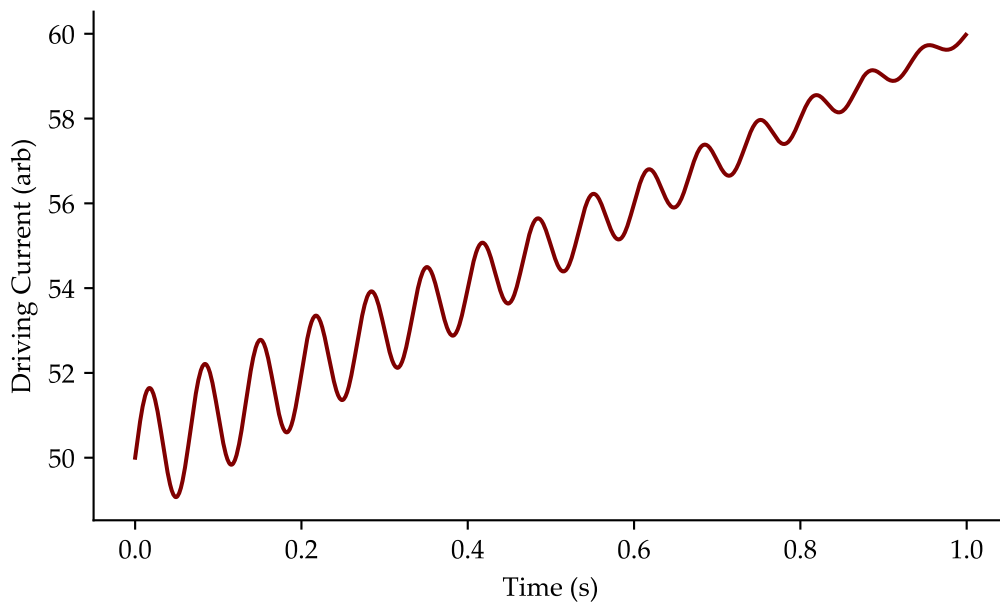
Figure 6.20: An example of the combined result of the enveloping function (P) to the ramped and sinusoidally modulated driving current

$P_{(t)}$ could simply be the reciprocal of $q_{(t)}$, but due to choices made in coding the software that will implement this solution, it is implemented in the form of a simple polynomial.

In order to implement a system that implements the above ideas, an RRI system that had previously been developed by K. Wiseman in the course of his PhD at Cranfield University for use in laser stability applications was modified. Unlike the system used in Chapter 5, this system was built on National Instruments hardware and programmed in LabView software, making modification of its processes possible for the author. The system already produced a sinusoidal modulation the amplitude and frequency of which could be altered in the software. A schematic diagram of the part of the LabView code that produces the laser modulation is shown below in Figure 6.21. A clock module, along with user defined values for the frequency and amplitude of the sinusoidal modulation is used by a module to produce a sinusoidally varying voltage that is applied to the current control of the laser to produce the wavelength modulation needed for interferometry. The software that demodulates and interprets the signal is not in-

cluded in the schematic as it is left unchanged and performs the same functions as described in Section 4.4. It should be noted that this Wiseman RRI system has the ability to measure the RRI amplitude at only three OPDs simultaneously.
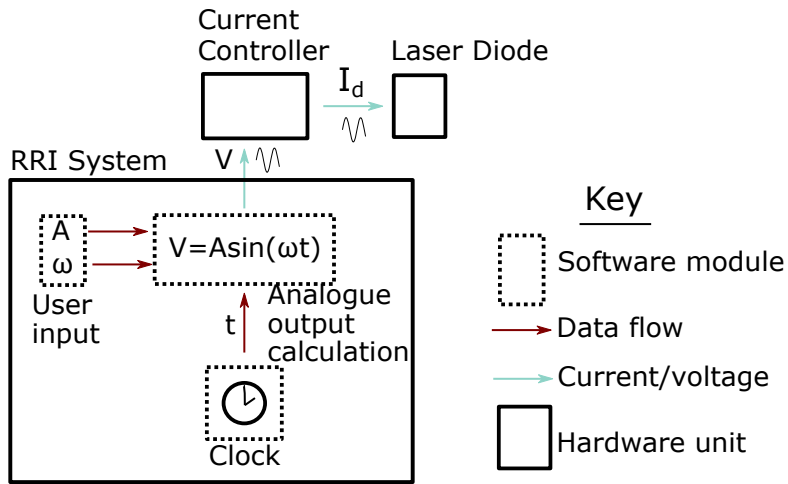
Figure 6.21: A schematic of the data flow and output of the LabView software as supplied showing the clock module, user inputs and the produced sine modulation.

In order to sweep the laser's central frequency across the methane absorption feature, a ramp function generator module was added, the value of which could be added to the sinusoidal function pin software, as was done by the external signal generator and voltage adder in the work described in Chapter 5. The ramp function was programmed to have a time period that would be set as an integer number of the sinusoidal periods. To perform the enveloping, a module was created that created a polynomial using the time produced by the clock. The value of this polynomial was calculated at the frequency of the sinusoidal modulation and multiplied by the value of the sinusoidal modulation. This product was then added to the ramp modulation value and output as a voltage to the current controller. This process is shown schematically in Figure 6.22
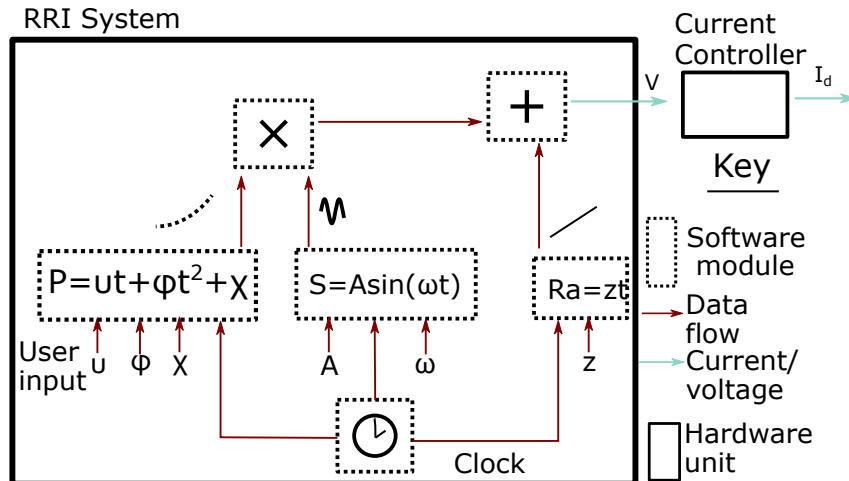
Figure 6.22: A schematic of the data flow and output of the software modules that provide the modulation to the current controller of the laser. The user defined parameters for the ramp (R_a), enveloping (P) and sinusoidal (S) modulation are used to produce a voltage modulation (V) similar in shape to that shown in Figure 6.20

6.5 USING LABVIEW SOFTWARE TO PERFORM REAL-TIME GAS MEASUREMENTS

With the software that was described in Section 6.4.2, the user is able to set the parameters for the ramp, the sinusoidal modulation, and the polynomial functions that are used to modulate the laser injection current. The input screen is shown in Figure 6.23.
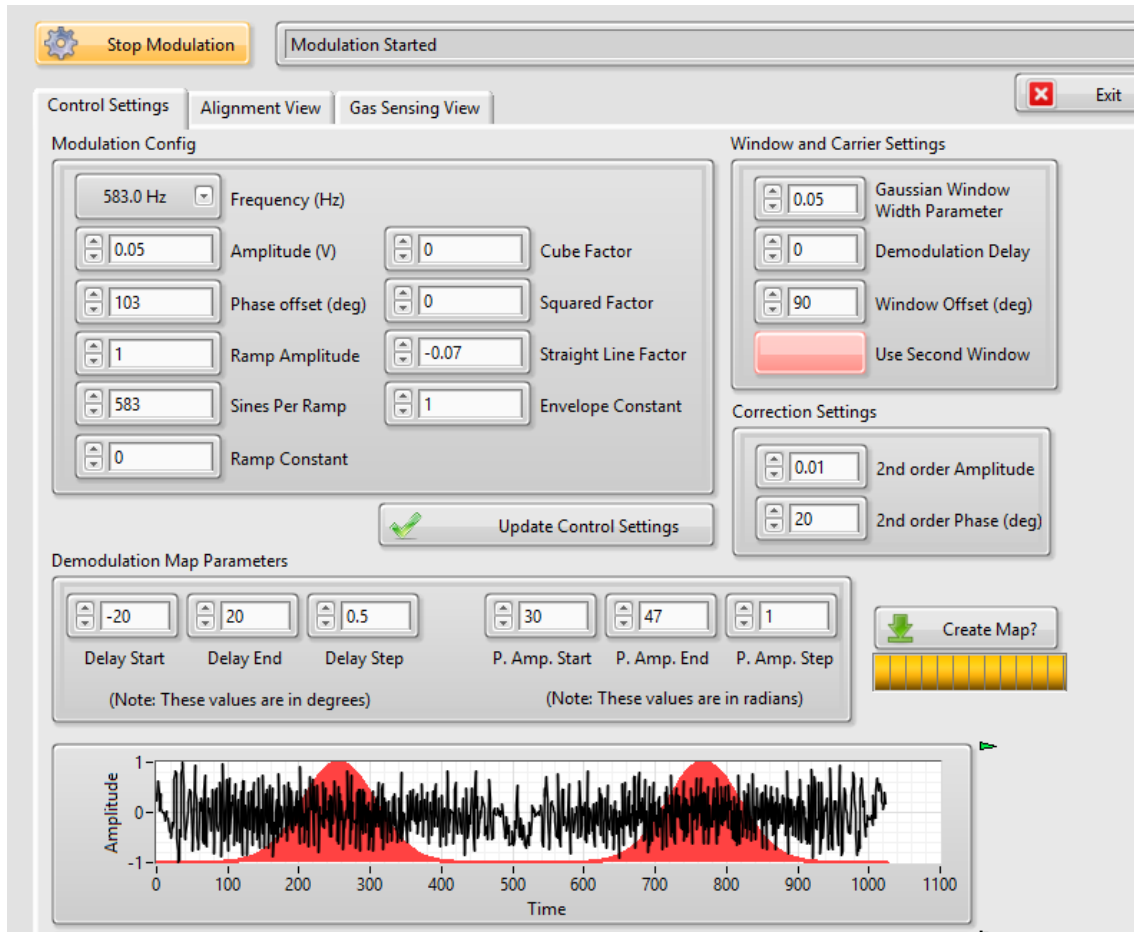
Figure 6.23: The user interface for the LabView software

For the purposes of gas sensing, the key panel where the parameters are set is labelled Modulation Config. In the implemented software, the user is able to define the parameters of the enveloping function as a 3rd degree polynomial as well as the parameters of the ramp and sinusoidal modulation. The other settings are for fine control of the RRI demodulation process and are beyond the scope of this thesis.

The experiment was set up using the topology described in Figure 6.11 with no additional fibres (Lxn). The sinusoidal modulation was set to operate at 583Hz, with an output amplitude of 0.05V. An RRI amplitude map was then produced and displayed as in
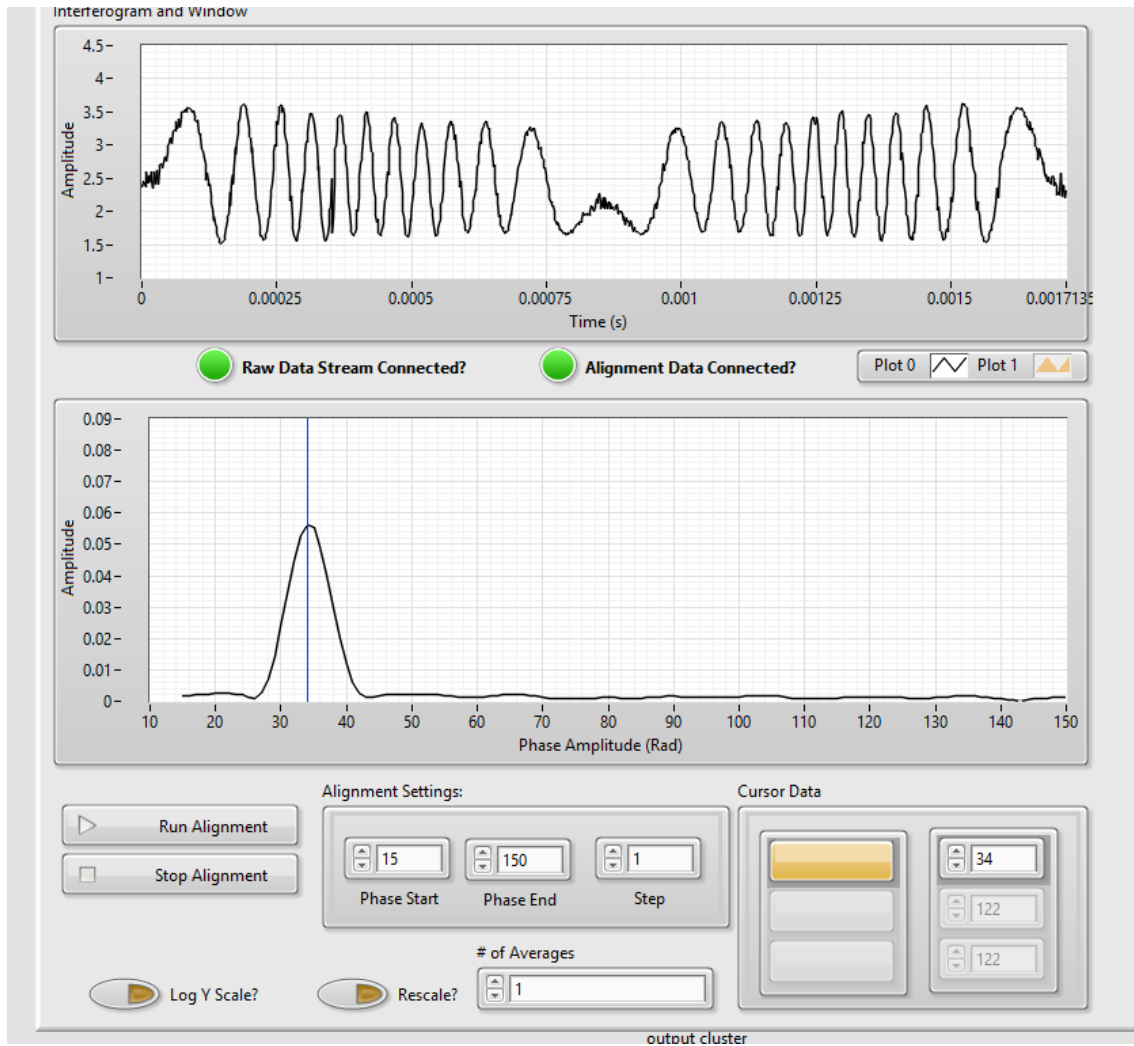
Figure 6.24: The RRI amplitude map produced by the LabView software. The top region shows the interferogram measured at the photodiode and the bottom represents an RRI amplitude map of the system.
This image is of a system with a single sensing region.

The user is then able to set up to three OPDs to demodulate, and the system then interrogates the RRI amplitude of the signals associated with those interferometers. With a ramp applied so that the central output wavelength of the laser crossed the absorption feature of methane, a measure of the RRI amplitude at an OPD associated with an interferometer of interest was taken over a period of 2 seconds, the ramp having a period of 1 second. With the enveloping polynomial function set to a constant value of 1, no enveloping was applied and the RRI amplitude peak moved as expected. This had the effect on the RRI amplitude at

the measured OPD as shown below in Figure 6.25. This is equivalent to the plot shown in Figure 5.8
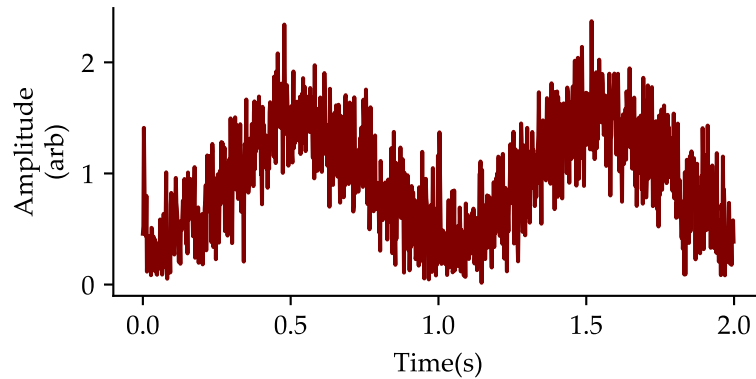
Figure 6.25: Normalised RRI amplitude measured in the absence of an enveloping polynomial (P). The amplitude starts from zero when the peak is not at the same OPD as the measurement, rises as it comes closer to that OPD and then drops again as the peak moves away.

A polynomial function was then created by adjusting the values on the user interface shown in Figure 6.23 and then simply watching the RRI map shown in Figure 6.24, adjusting the parameters by eye until the peak appeared to be stationary. Theoretically it should be possible to calculate the necessary parameters from a plot similar to Figure 6.19, but the relationship between wavelength excursion and the central driving current was measured at 49kHz, while the Lab-View software was only able to operate at frequencies of the order of hundreds of Hertz and the relationship cannot be assumed to hold at this lower modulation frequency. The enveloping polynomial that was found to cause the position of the RRI amplitude peak to remain stationary was $P = 1 - 8t + 0t^2$. With this enveloping polynomial enveloping applied, the RRI amplitude at the OPD of interest was measured again, and is plotted below in Figure 6.26
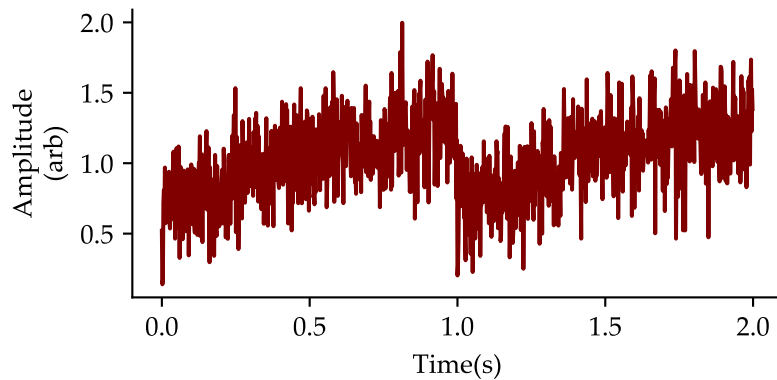
Figure 6.26: Normalised RRI amplitude measured over two ramp periods with the applied sinusoidal modulation subject to a polynomial enveloping. This looks like a noisy TDLS signal with the rising amplitude due to the increasing laser power over the ramp.

Visual inspection of the measured amplitude shows a clear reduction in any effect of the motion of the RRI amplitude peak. The resulting plot of RRI amplitude resembles a standard TDLS signal over two ramp periods. The LabView system however, shows the presence of a lower signal-to-noise ratio that previous work done with the RRI system used in Chapter 5. It is likely that this is in part due to a difference in bit-depth between the National Instruments hardware and the hardware used in the system used in Chapter 5. However, no work was done to investigate the sources of noise as this work is considered to be a proof of concept, and any further development of the technique will be done on a system closer in nature to that used in Chapter 5.

To more precisely measure the effect of the enveloping, we consider the fact that the purpose of the RRI amplitude measurement is to produce a TDLS-like curve from which gas concentrations can be calculated. To that end, the data from a single ramp period was taken and compared to a fitted straight line to calculate what would be measured as the normalised absorption across the sweep, as in Chapter 5 before that normalised absorption was fitted to a Lorentzian curve.
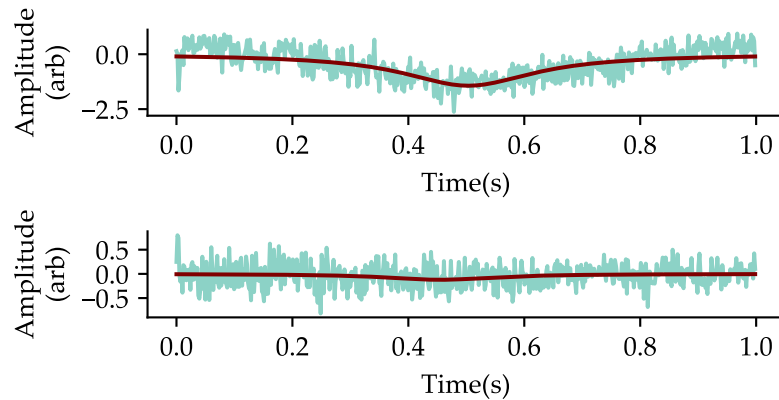
Figure 6.27: The residuals from the fitting of each of the data sets in Figure 6.25 (top) and Figure 6.26 (bottom)

Given that no gas was present when the data was gathered, we should expect the measured normalised absorption and the height of the fitted lorentzian curve to be zero. However, in the case with no enveloping, the fitted Lorentzian curve has a height of -1.43. The data taken with the enveloping applied produces a Lorentzian with a height of -0.12. This is an improvement by a factor of 11.9. It is likely that further improvements could be made with a more systematic approach to the setting of the enveloping polynomial, but that would best be performed on a system with lower noise levels than the currently available one.

6.5.1 *real-time Gas Detection*

With the LabView system capable of preventing the motion of the RRI amplitude peaks, and thereby producing a TDLS-like curve, in order for it to act as a real-time, stand alone gas sensing unit, a module was added that would interpret the TDLS curve and provide a value for the amplitude of any detected normalised absorption curve. This module took a simple ramp period's worth of data for each of the three measured channels, and applied the same algorithm that was applied to extract the absorption peak height from the TDLS-like curves in Chapter 5. This process is not computationally difficult and is done in less time than

the ramp period, meaning that a real-time measure of the calculated absorption peak height can be provided. To allow user monitoring, the software was modified to display a number of pieces of information as shown in Figure 6.28
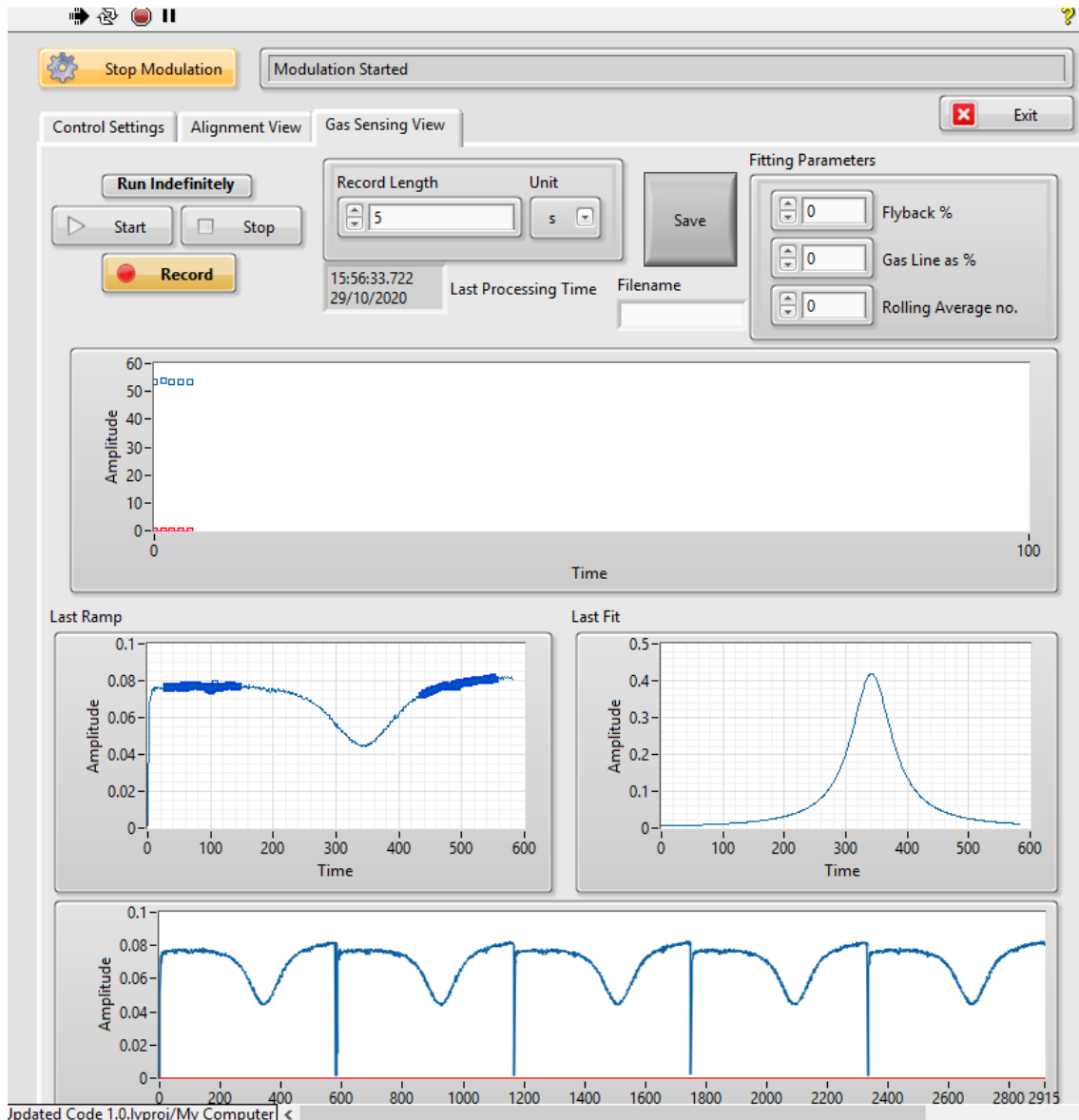
Figure 6.28: The gas concentration monitoring screen.
The screen contains user input options that allow the user to determine the regions of the plot that are used to fit the zero gas background
This figure shows a single OPD being interrogated. (2.5% methane present in the gas tube)

The system allows the real-time monitoring of the RRI amplitude at each of the monitored OPDs, as well as the extracted gas absorption curve and the resultant peak height over time. The gas concentration data can be saved to file along

with the last five TDLS-like curves. The system was unable to show any response to methane concentrations of 1000ppm, with any absorption being indistinguishable from noise levels within the system. Criteria were added to the peak fitting algorithm so that peaks that were not in the centre of the data and were not of the expected width would be rejected and the absorption reported as zero. Three sensing regions were used and starting from being filled with zero hydrocarbon air, they were filled at different times with a 2.5% concentration of methane. The methane was then replaced with hydrocarbon free air once more. The recorded values of the absorption height peaks are shown below in Figure 6.29.
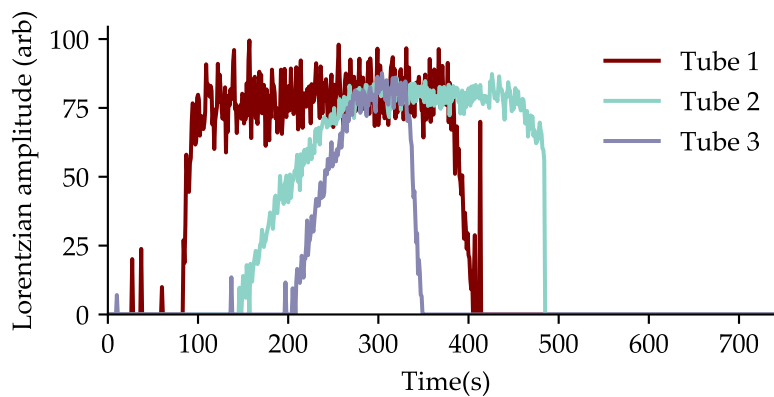
Figure 6.29: The values measured for the amplitude of the Lorentzian absorption curve measured in each sensing location as a function of time.

Figure 6.29 shows that the system responds to changes in methane concentration at the three sensing locations independently and in real-time. When the sensing regions were all filled with 2.5% methane, they all showed approximately the same absorption heights. The system also shows response to levels of methane below the 2.5% concentration as evidenced by the readings as the methane filled the tubes. However, the LabView software itself was not stable over the long term, crashing, possibly due to memory leaks, meaning that no calibration or long term stability testing as discussed in Chapter 5 could be performed.

6.6 SUMMARY

While Chapter 5 demonstrated that Range Resolved Interferometry could be used, in principle, to measure the presence and concentration of methane in a number of places simultaneously, the system as presented there was only shown to operate in a Mach-Zehnder topology and not in a real-time capacity. Both of these problems would make it unsuitable for deployment. Two possible topologies were examined, a serial and a serial bus topology. It was shown that the serial-bus topology had a number of advantages including a higher light intensity illuminating the later sensing regions as well as maintaining the independence of each sensing region.

It was shown that the response of the laser to sinusoidal modulation was not constant over the applied ramp modulation, and that this was the cause of the apparent motion of the RRI amplitude peak that had previously required off line, non real-time data processing to form a TDLS-like curve from which gas concentrations could be measured. A method to overcome this problem by applying an enveloping function was developed so that the amplitude of the sinusoidal modulation varied over time. This removed the need for post-processing to produce a TDLS-like curve, instead producing it in real-time and thus allowing the detection of gas in three independent locations in real-time.

Both the ability to deploy sensing regions in an effective topology and the ability to measure methane in real-time are essential factors in deployment of an RRI system in a safety critical environment.

THE EFFECTS OF RRI ON TDLS MEASUREMENTS

7.1 INTRODUCTION

Previous chapters have shown the possibility of using Range Resolved Interferometry to measure the concentration of methane in a number of locations simultaneously in real-time. In order for such a system to be put into use, a number of parameters of the system would need to be measured and optimised. As an example of one such parameter, the effect of the amplitude of the sinusoidal wavelength modulation on measurement capabilities is investigated in this chapter. As this sinusoidal RRI modulation amplitude is varied, the laser interaction with the wavelengths that are absorbed by the methane are shifted in time. This has an effect on the measured shape of the absorption feature, as opposed to its natural shape, and this effect must be understood since the shape of the absorption feature is used to calculate the methane concentrations. In addition, the ability of the RRI system to identify individual interferometers is used to extract the signal of interest from with a system with unwanted optical fringing, fringing being a potentially serious impediment to the measurement of gas concentration[155]. Fringing occurs when etalons are formed in the gas path which forms interferometric signals that sit on top of the measurement signal. Range Resolved Interferometry is used to identify the desired signal and measure it without the influence of the parasitic signal.

7.2   EFFECTS OF MODULATION DEPTH

In the work presented in this thesis, Range Resolved Interferometry has been used to extract an absorption curve produced when light passes through a sample of methane gas. As discussed in Section 2.4.1, the shape of an absorption feature of a gas is determined by factors such as the temperature and pressure of the sample being tested. This can be thought of as the absorption feature's natural line shape in those conditions. In standard direct tunable diode laser spectroscopy, the shape of the absorption feature is directly measured. The use of RRI to interrogate the gas absorption feature, as with wavelength modulation spectroscopy, however adds a sinusoidal modulation to the ramp modulation, which has an effect on the measured lineshape as described in this chapter. As shown in Figure 7.1, a sinusoidally modulated laser beam has a wavelength equivalent to the a point on the absorption curve of a gas species earlier than a the purely ramped laser. In Figure 7.1, this is ilustrated by showing the point at which the sinusoidal (red) and ramped (blue) laser wavelengths cross a point corresponding with the full width half maximum (FWHM) points of the absorption curve (shown in grey).
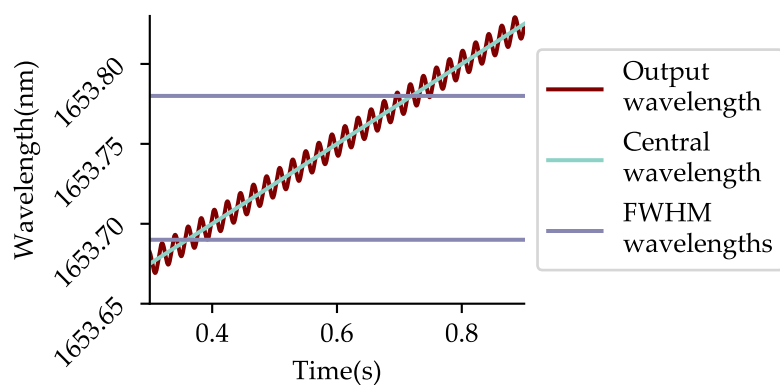
Figure 7.1: The different behaviour of a standard TDLS ramp and a RRI modulated laser. The blue line shows the behaviour of a laser undergoing a sawtooth modulation, while the red line shows the wavelength response of a laser being modulated for RRI. The grey lines are the fullwidth half maximum points on the natural line shape of a methane absorption feature.

The rapid sinusoidal modulation of the laser effectively produces a wavelength emission that is wider in wavelength space, and when this is convolved with the natural lineshape of the absorption feature will produce a measured lineshape that is broader and shallower than the natural one.

In order to visualise the effect of the magnitude of RRI modulation, software that modelled the process of Range Resolved Interferometry and its interaction with absorption features was created. The logic flow of this software is shown in Figure 7.2
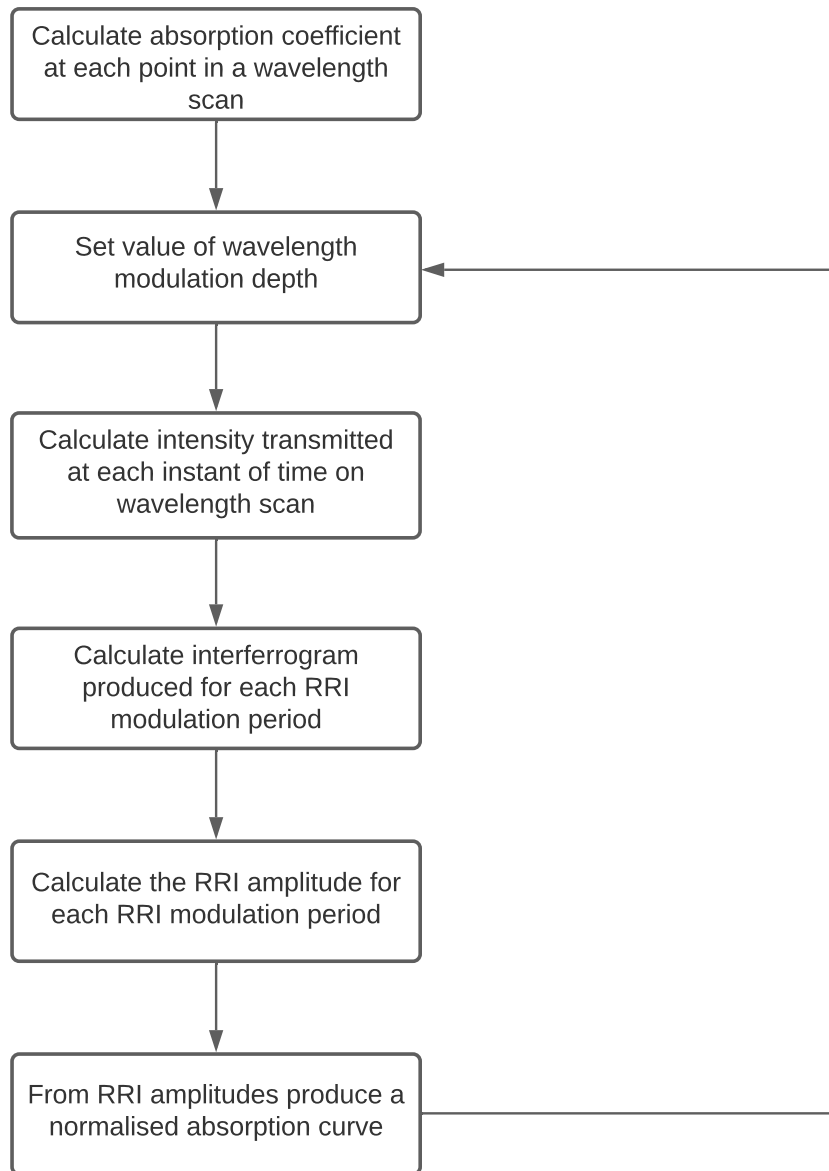
Figure 7.2: Logic flow for software used to simulate the effect of modulation depth on measured absorption lineshape

Using different values for the amplitude of the RRI modulation, the system was used to simulate the RRI amplitude that would be measured when light was passed through a two armed interferometer that contained a set concentration of methane in the sensing arm. The results are shown in Figure 7.3
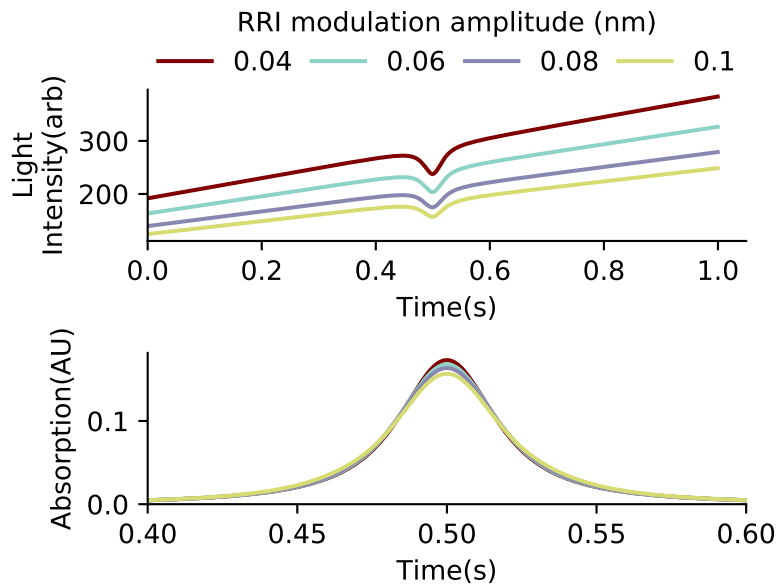
Figure 7.3: Top: The TDLS-like curves produced from a simulated interferometer containing a constant constant concentration of methane in a single sensing region when different amplitudes of RRI modulation are applied.
Bottom: The normalised absorption curves calculated from the TDLS-like curves, showing the perceived broadening of the absorption feature as the modulation amplitude increases

Figure 7.3 shows the broadening of the perceived absorption feature as the RRI modulation amplitude increases, and this effect is quantified in Figure 7.4.
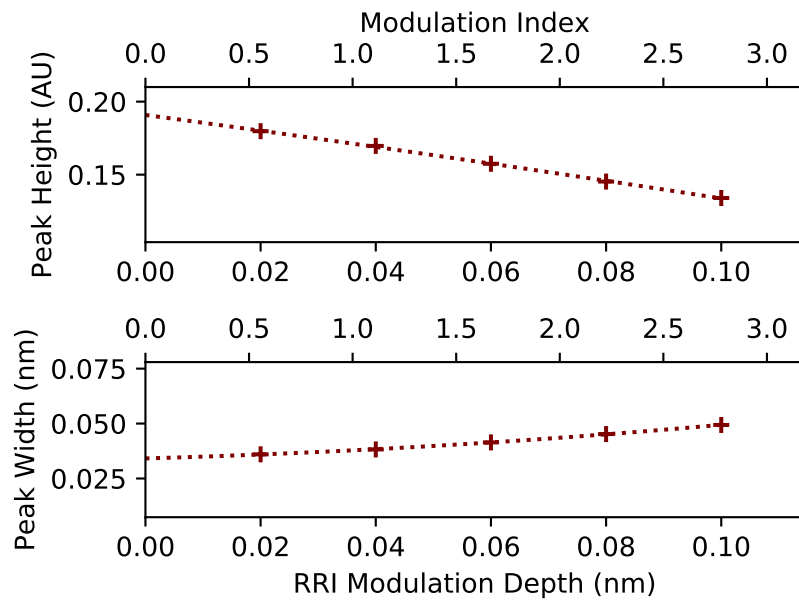
Figure 7.4: The peak height and the full width half maximum of the absorption curves from Figure 7.3, as a function of the RRI modulation amplitude applied in terms of the modulation depth and the modulation index (the ratio between the modulation amplitude and the width of the absorption feature)

In order to validate this simulated decrease in peak height as a function of RRI modulation amplitude. experimental tests were performed wherein the absorption peak height was measured using RRI. The Wiseman RRI system allows control of the amplitude of the RRI amplitude applied to the laser control in a range of 0.05V to 0.3V. The system outputs the calculated absorbance values as a function of time and a fitted Lorentzian curve. These outputs, measured at various RRI modulation amplitudes are shown in Figure 7.5
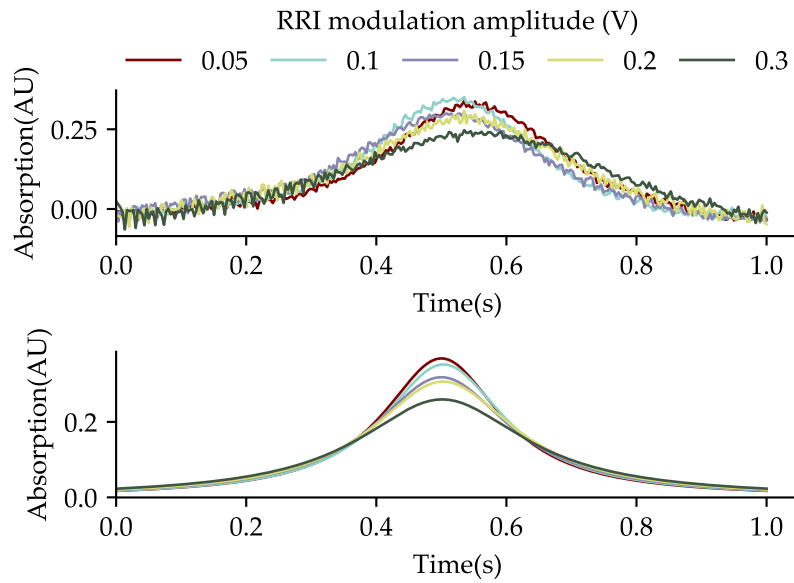
Figure 7.5: Top: The reported absorption curves measured with a sensing region filled with a constant concentration of methane, using different amplitudes of RRI modulation.
Bottom: The Lorentzian curves fitted to these absorption curves after the data has been centred for ease of comparison

As with the simulated data, decreased absorption height is seen as RRI modulation increases, and this is again quantified in Figure 7.6
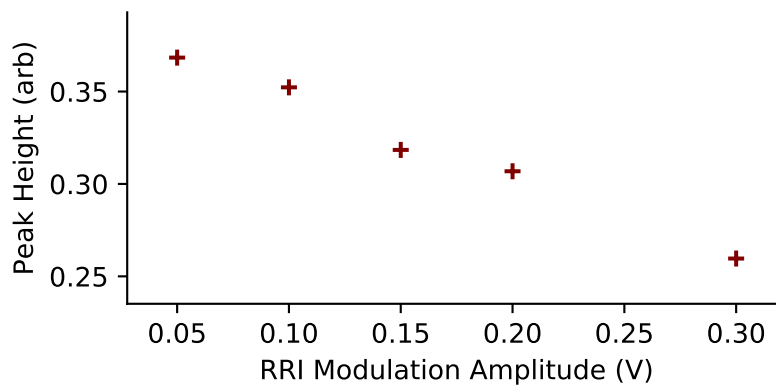
Figure 7.6: The peak height of the absorption curves from Figure 7.5, as a function of the RRI modulation amplitude applied

In agreement with the modelled relationship, there is a drop in the measured height of the absorption curve as the RRI modulation amplitude increases. Assuming a constant value for the noise within the system, this would lead to a

lower signal-to-noise ratio and a lower limit of detection. This could be countered by using a lower RRI modulation amplitude, but due to the nature of the phase carrier amplitude (A_n) in Equation 4.4 which is proportional to the optical path difference and the RRI modulation amplitude, a decrease in the RRI modulation amplitude would lead to a loss of spatial resolution in the system. The spatial resolution of the RRI system, defined as the minimum difference in the OPDs that can be resolved is set by the ability of the window function ($W(t)$) to suppress contributions to the demodulated signal from anything other than the interferometer of interest. This ability, expressed in terms of a broadband suppression ration (S_{bb}) is greater for narrower window functions and for each given window function is a function of the applied phase modulation amplitude (A_k) for a given OPD. The relationship between the phase modulation amplitude and the broadband suppression ratio is plotted in the work of Kissinger[24]. For any chosen limit of S_{bb}, a corresponding minimum value of A_k can be determined and converted to a minimum OPD separation as shown in Equation 7.1 wherein λ_0 represents the central wavelength about which the laser is oscillated

$$\eta_{min} \approx \frac{A_{min}\lambda_0{}^2}{\Delta\lambda} \tag{7.1}$$

If values for a minimum acceptable value of S_{bb} is chosen to be 80dB, then using the figure in Kissinger[24] and a window width of 0.0225, a value of $A_m in$ of 40rads is established. Thus, a laser modulated by 0.01nm around a wavelength of 1653nm, then a minimum OPD seperation of 1.3m is shown to be possible, while under the same criteria, a modulation of 0.02nm yields a spatial resolution of 0.65m. This work therefore shows the existence between a trade-off between the spatial resolution and gas sensing capabilities of any RRI based gas detection system. Spatial resolution in this context refers to the minimum separation between the OPDs of the system, but does not directly relate to the spacings of the sensors. For example, while the system shown in Chapter 5 has the interferometers of interest with OPDs that are separated by multiples of 2m, Figure 5.16

shows that the sensing regions are placed approximately 20cm apart on the optical bench and could in fact be placed anywhere that the fibre connections will allow. Spatial resolution would be a determining factor in the number of sensors that could be deployed in a serial topology, as the system is limited by the coherence length of the laser being used and the number of sensors that could fit within any given length would be determined in part by the necessary separation between their OPDs.

7.3 RRI AS A FRINGE SUPPRESSION TECHNIQUE

As was discussed in Section 2.4.2.1, in many instances the existence of interference fringes is a limiting factor in the measurement capabilities of tunable diode laser spectroscopy (TDLS)[72]. In gas sensing, these fringes are often caused by reflections between surfaces that form the gas cells such as the cell windows[70]. While care can be taken to avoid these in the design of the cells, using components such as wedged windows and anti-reflection coatings, some etalons may persist or develop over time. The fringes are caused by the interference of multiple beams within the system, with the fringes having a free spectral range determined by the size of the etalon that gives rise to them. Thus, they are effectively the product of parasitic interferometers that are added to the interferometers of interest within the system. Given RRI's ability to interrogate the interferometers of interest and disregard the parasitic ones, it was decided to investigate whether this could be used to reduce the influence of unwanted optical fringing on a measurement. In order to test this hypothesis, a system with a reliable source of unwanted interference fringes was needed. To that end, the equipment shown in Figure 7.7 was used.
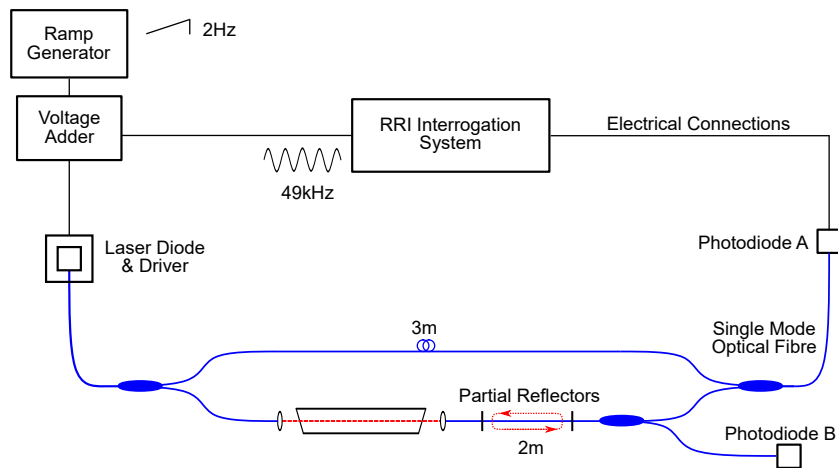
Figure 7.7: The experimental apparatus used to test the ability of the RRI system to suppress the effect of etalon fringes. An etalon of 2m length of fibre was formed in the measurement arm by use of Thor Labs in-fibre partial reflectors.

The use of Thor Labs in-fibre partial reflectors with reflectance of 90% created an etalon between them of a known, and stable length of 2m in fibre which acted as a reliable source of fringes. To show the presence of the fringes, the signal at Photodiode B was measured over the period of a single sawtooth modulation with no RRI modulation applied. This is shown below in Figure 7.8.
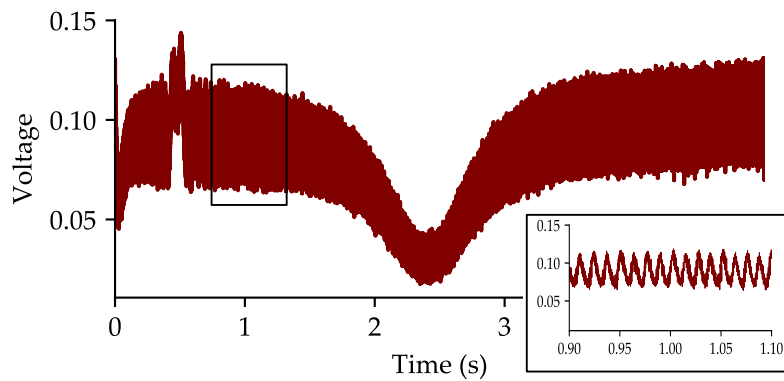
Figure 7.8: The signal at photodiode B during a single sawtooth modulation period. The sinusoidal nature of the features in the zoomed in section shows it to be an interferometric, rather than random source.

The amplitude of the fringes is visible to the naked eye, but to quantify their effect, the photodiode signal was turned into a plot of normalised absorption (Figure 7.9) and the height of the absorption peak (0.78) was compared to the

standard deviation of the last 10% of the curve (0.15) to produce a signal-to-noise ratio of 5.2.
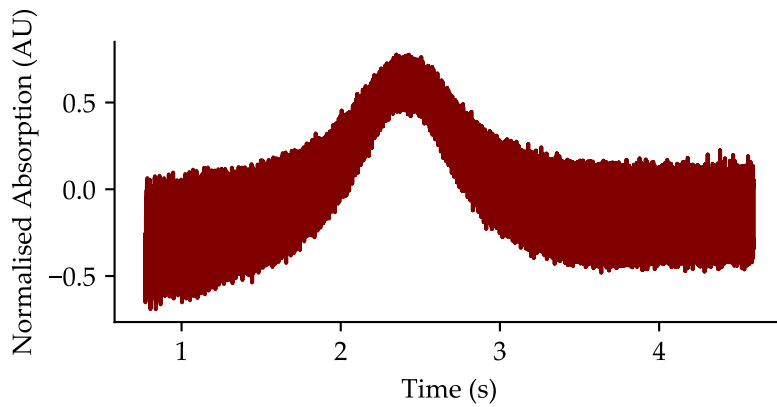
Figure 7.9: The normalised absorption curve calculated from the data shown in Figure 7.8

RRI modulation was then applied and the signal at photodiode A was demodulated to produce the RRI amplitude map in Figure 7.10.
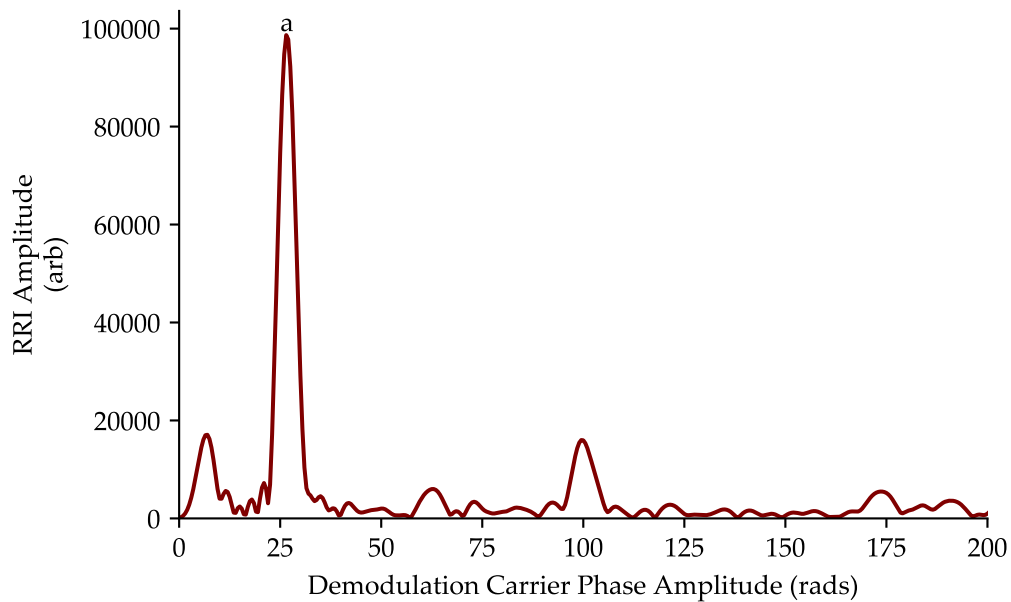
Figure 7.10: The RRI amplitude map of the system shown in Figure 7.7. The peak labelled (a) was that of the interferometer of interest, while other peaks were parasitic interferometers, including those caused by the etalon

Using the the techniques described in Chapter 5, a TDLS-like curve of the light intensity passing through the sensing region was taken and is shown below in Figure 7.11
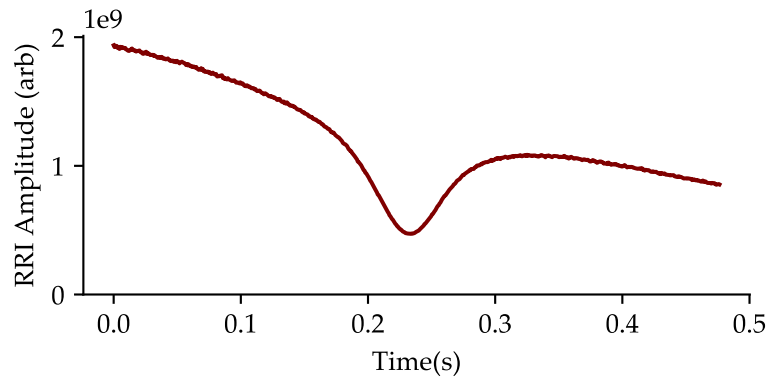
Figure 7.11: The RRI signal taken from the interferometer of interest in Figure 7.7

Visual inspection shows that the application of RRI to a system with optical fringes provides a large improvement in the signal-to-noise ratio, but for the purposes of quantification, the same process as for the previous TDLS data was performed. The normalised absorption curve was calculated Figure 7.12, and the height of the absorption curve (0.66) was compared to the standard deviation of the last 10% of the data points in the curve (0.0069) to produce an SNR of 94.
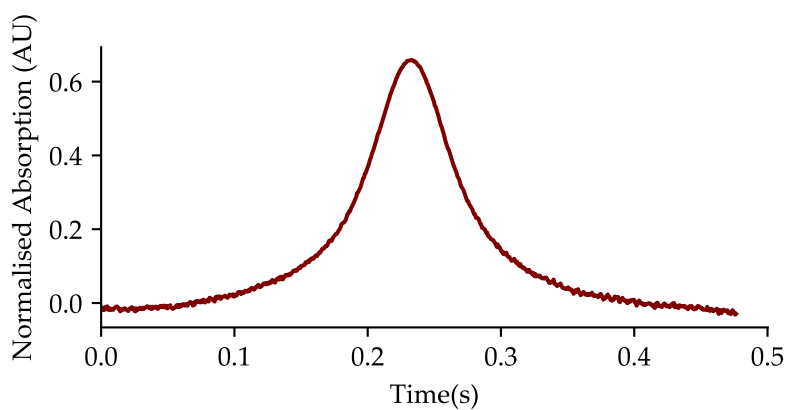
Figure 7.12: The normalised absorption curve calculated from the data shown in Figure 7.11

Thus, the application of RRI to a system beset with optical fringes can increase the signal-to-noise ratio by a factor of 18. The fact that in Figure 7.12 are not visible, suggests that they have been suppressed below the level of other noise sources. In addition, an Fourier transform of an equivalent portion of each of the data sets was calculated and shown in Figure 7.13
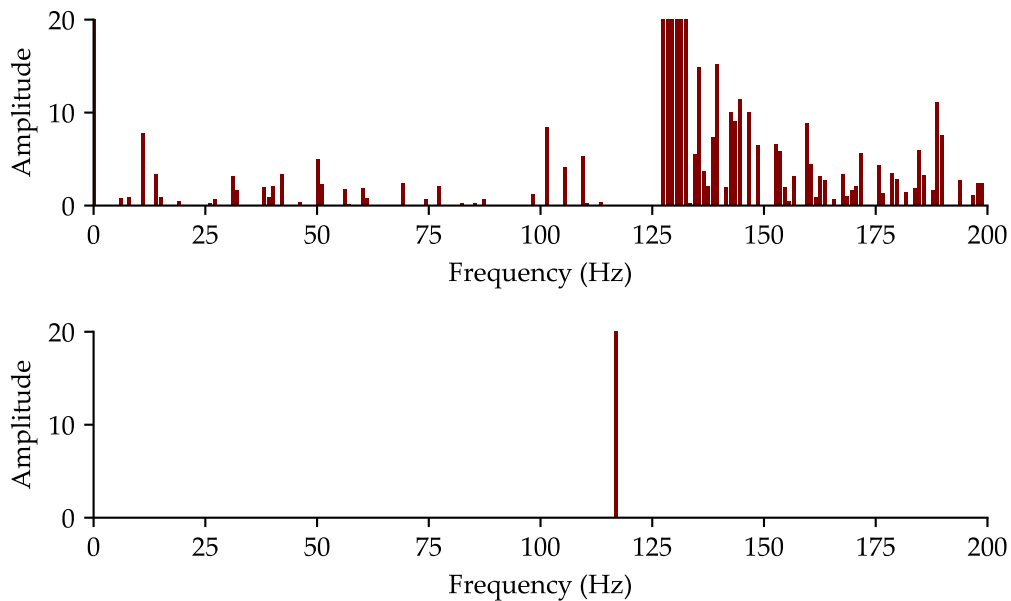
Figure 7.13: The Fourier transforms of the TDLS plot with fringes present (top) and the RRI measure of the same system (bottom)

Figure 7.13 shows, at the top, the Fourier transform of the system without the application of RRI. As well as other noise sources, there are a number of frequency components at around 50Hz, which corresponds with the frequency of the fringing shown in Figure 7.8. The Fourier transform of the RRI amplitude (Figure 7.11 shows no such frequency contribution at 50Hz suggesting that the effect of the etalon has been suppressed to a level that is not detectable.

7.4 SUMMARY

In this chapter, two experiments were undertaken, one aimed at showing an example of the work needed to optimise the RRI system for real world deployment

and one to show an additional capability of the RRI system for uses other than in multipoint gas sensing. It was shown that the RRI modulation amplitude applied to the system lowers the perceived peak height and increases the width of the absorption curves measured in the presence of methane concentrations. This will worsen the signal-to-noise ratio of the signal and so lower its potential limit of detection. However, simply reducing the amplitude of the RRI modulation is not necessarily the solution as this will lead to impaired spatial resolution. The second experiment showed that the ability of the RRI system to differentiate between different interferometric signal within a complex system can be used for the purposes of optical fringe suppression. By interrogating only the interferometer of interest, the RRI system reduced the effect of noise in a system with optical fringes by a factor of at least 18.

CONCLUSIONS AND FUTURE WORK

8.1 THESIS SUMMARY AND CONCLUSIONS

This thesis has described how Range Resolved Interferometry, used previously for positional measurements, was used for the spectroscopic measurement of methane gas concentrations in three locations simultaneously.

Range Resolved Interferometry, which allows the demodulation of individual signals from superpositions of multiple interferometric signals, was used with a Mach-Zehnder arrangement of three fibre coupled gas tubes that could be independently filled with methane and a reference path. When a 49kHz sinusoidal modulation was applied to a diode laser whose output was coupled into the interferometer, the system was able to identify the amplitude of interferometric signals associated with each of the interferometers. The system provided range information for each of the interferometers on an RRI amplitude map, with the interferometers having OPDs that differed by 2m. This allowed the identification of the signals associated with the interferometers of interest; those formed between a gas cell and the reference path, while allowing the user to measure their behaviour. A slow 2Hz ramped modulation was then added to the sinusoidal modulation to sweep the laser's central wavelength across a methane absorption feature at 1653nm. Monitoring the RRI amplitude of each of the interferometers of interest was then used as a method to measure the light intensity passing through the gas sensing region and thus the methane concentration. Due to the fact that the DFB laser used in the system did not have a constant wavelength modulation response to an applied sinusoidal current modulation at every cen-

tral driving current produced by the slow ramp modulation, the system was not capable of being operated in real-time, as the data had to be subject to significant post-processing in order to produce a TDLS-like curve from which methane concentrations could be measured.

In order to assess the potential of future iterations of the system for use in safety critical environments, the measurement capabilities of the system in its current form were tested. The height of the absorption peaks in the recovered TDLS-like curves were measured at various concentrations of methane and the system showed good linearity of response in the range 200-1000ppm with $R^2 \geqslant$ 0.95. In order to find the theoretical limit of detection of the system, Allen-Werle calculations were performed over time series data of absorption heights. This showed that with appropriate averaging times of around 3 minutes, the system would be capable of detecting concentrations as low as 4ppm. Finally, measurements of the gas concentration readings in one sensing region while the concentrations in the other regions were changed showed that the sensing regions were independent, with no detectable cross talk between them.

In order to operate in a field safety role, RRI needs to be able to be deployed in a more convenient way than the Mach-Zehnder topology would allow. Two topologies, serial and serial bus were theoretically examined to determine the loss budget for each. It was found that for expected levels of coupling inefficiencies in a system, the serial bus topology would be the most suitable in almost all real world use cases.

Finally, in order to be of value, RRI would have to be able to detect the presence of methane in real-time. To counter the non-constant wavelength response to the sinusoidal current, a LABVIEW based system was designed and built that applied an envelope function to the sinusoidal modulation current allowing it to vary as a function of the ramp modulation. This produced a constant wavelength modulation across the scan and enabled the real-time and simultaneous measurement of 2.5% methane in three locations, which is a concentration equiv-

alent to half of the lower explosive limit of methane, suggesting that RRI has potential to operate in safety critical roles where speed of response is important.

8.2 SUMMARY OF PROGRESS TOWARDS THESIS OBJECTIVES

The initial aims of the work described in this thesis were outlined in Chapter 1 and were met as follows:

- Investigate the ability of RRI to show the presence of methane in a single location

    - In Section 5.2.2 it was shown that a reduction in the RRI amplitude measured was associated with the presence of methane. In order to do this, the RRI amplitude of a single sensing region was measured as the laser was swept across a gas feature. The outcome was a visible dip in the RRI amplitude caused absorption.

- Determine if it can be used to produce a measurement of methane concentration using a similar approach to TDLS

    - Section 5.2.3 details the creation of a TDLS-like absorption curve from multiple RRI amplitudes using post-processing. Measuring each sensing region with a single complex carrier function did not produce a TDLS-like curve due to non constant response of the laser to the sinusoidal modulation as the central bias current was ramped. In order to mitigate this a number of complex carriers were applied per sensing region which allowed the reconstruction of the RRI amplitude and thus light intensity as a function of time.This allowed the production of TDLS-like spectra showing the presence of methane.

- Establish whether RRI can perform this measurement of methane concentration in multiple locations simultaneously and independently

– Section 5.4 showed that the RRI system could be used to measure three locations simultaneously, while Section 5.4.4 showed that each sensing location could be measured independently of one another with no detected crosstalk. above the level of experimental uncertainty.

• Confirm the ability of RRI to perform this measurement in real-time

– Section 6.5 shows the ability of an RRI based system to operate in real-time measuring the presence of gas in three locations in real-time. In order to achieve this, the effect of the non-uniform response to sinusoidal modulation was mitigated by preshaping of the applied modulation to produce a constant wavelength modulation.

• Characterise the limits of detection of the system built to perform these tasks

– Section 5.4.2 found that the post-processed system of RRI had a linear response in response to methane concentrations as low as approximately 200ppm, while an Allen-Werle analysis in Section 5.4.3 showed that it had the potential, given adequate averaging time, to measure gas concentrations as low as 4ppm for the sensing region with the lowest signal-to-noise ratio to 16ppm for the region with the greatest SNR.

8.3   FUTURE WORK

This thesis has described the first use of the RRI technology to perform real-time multipoint measurements of gas concentrations. While the measurement system met the expectations described in the thesis objectives, the complete capabilities of this technology are as yet unknown. As it stands, the system does not meet the requirements of combined limit of detection and speed of response required for operation in explosion prevention. Speed of response is only possible using the

Wiseman system, although it was not directly measured, as the Kissinger system requires slow post-processing, while the Wiseman system does allow real-time measurement but has a signal-to-noise ratio such that no methane below concentrations of 2.5%(25000ppm) were detected. Some ways to improve the capabilities of an RRI based gas detection system are described below. Two systems were used in the work described in this thesis, referred to as the Kissinger and the Wiseman systems(see Appendix A). The Kissinger system, based on Altera Cyclone IV FPGA technology had a higher signal-to-noise ratio, but was not able to be adjusted by the author to provide the preshaping of the modulation needed for real-time concentration measurements. The Wiseman system, being based on National Instruments hardware and programmed in LabVIEW software could be modified to provide this preshaping and thus allow real-time measurement. However this came at the expense of a lower signal-to-noise ratio inherent in that system. It is thought that the main cause of this noise level is down to the lower resolution of the analogue to digital converter used. The next step in development of an RRI gas detection system would be to produce a system closer in design to the Kissinger system that would allow immediate improvements in signal-to-noise ratios while still allowing the preshaping of the modulation that allows the real-time measurement of methane concentrations. Once such a system has been built, a method of determining the form of the preshaping should be undertaken that is more thorough and precise than the judgement by eye used in this work. A system could be designed that would allow the system to measure the location of an RRI amplitude peak at various bias currents and at various modulation depths and use this information to pre-shape the sinusoidal modulation to prevent the apparent motion of the RRI amplitude peak. If the peak was more stable in its position, then this would lead to a better fit for the baseline used to calculate the absorption, and thus the concentration. The only source of noise detailed in this thesis was that due to the phase noise of the diode laser. The fact that decreasing the light coupled through the sensing region does

not improve the SNR suggests that this phase noise is dominant, as does the fact that the longer path lengths have greater levels of noise. Given the fact that it is this phase noise that dominates the system as currently operated, it is likely that this will be the deciding factor determining the number of sensors that can be deployed. The work done on the effect of modulation depth shows that greater spatial resolution and thus more sensors with an acceptable phase noise could be achieved but at the expense of lower signal produced by a given concentration of gas. It has been shown that the sensing regions with the longest path lengths have greater noise, no quantification of noise as a function of path length was made and so no reliable estimate of the number of sensing regions that could be monitored is as yet possible. Work on characterising the effect of pathlength on the ratio of phase noise to gas absorption signal will need to be performed in the future. The use of a laser with greater coherence would be a method to reduce this source of noise. The form of the Allen-Werle diagram, and the fact that greater averaging times leads to improved limits of detection show that white noise is present in the system and an early task for system improvement would be a full noise audit of the next iteration of the technology. This would then enable the identification of potential improvements that could be made. Effects due to any polarisation drift in the system will also need to be investigated, particularly as the system is deployed with longer lengths of fibre. It may be that polarisation diversity systems[156] could be implemented to mitigate this effect and produce a more stable measurement over long measurement periods. RRI has primarily been used to investigate the phase of the interferometric signals and extract information from that. Gas detection systems have been developed that can use changes in the phase of light caused by the dispersion effect of gas on light incident upon it[157, 158]. There is therefore the potential to use this phase information in a gas detection technique. As well as the signal processing, improvements can be made in the deployment of the sensing regions themselves. The work presented in Chapter 6 was done on the assumption that in each of the

investigated deployment topologies, a single coupler ratio or reflectance value was used. The aim of this was to simplify the system for deployment with an unknown number of sensing regions up to a given maximum. However, this is not the most efficient way of dividing the light between any given number of sensors and alternatives could be investigated. This could be done in consultation with a sensor manufacturer with understanding of potential end users' needs from such a system. Improvements in the sensing regions themselves could also be made. Losses of 60% on each pass are not suitable for field deployment and far better coupling needs to be achieved. Commercially available gas cells are available with fibre-to-fibre throughputs of >50%[159] which would be an immediate improvement. Another method, the use of fibre lenses to couple light into and out of gas cells is claimed to have "low" losses compared to conventional lens systems[160]. An alternative to conventional gas cells is the use of structured fibres. These were mentioned in Chapter 3 and allow the interaction of light with the gas within the fibre. They allow long gas cells and thus potentially more sensitive gas detection[161]. Technical issues with the use of these fibres include the method used to allow gas to enter the hollow core of the fibre and thus interact with the light. This has been achieved by the designing of particular splices with gaps to allow the gas to enter[116] or by drilling holes into the fibre along its length[162]. In addition, engineering solutions would be needed that would protect the fibre from damage and environmental dirt, while still allowing air to enter the sensing region of the fibre. If these technical and signal processing improvements are made, Range Resolved Interferometry has the potential to provide a cost effective answer to the problem of multipoint gas sensing.

PUBLICATIONS AND OTHER OUTCOMES

The following publications and other outcomes have resulted from the work presented in this thesis.

PEER REVIEWED JOURNAL ARTICLE

J. A. Bremner, T. Kissinger, J. Hodgkinson, and R. P. Tatam, "Fibre-coupled,multiplexed methane detection using range-resolved interferometry,"Journal of Physics: Photonics, vol.3, no.2, 02LT01 2021.

PEER REVIEWED CONFERENCES

J. Bremner, T. Kissinger, J. Hodgkinson, and R. P. Tatam, "Range resolved interferometric multiplexing of optical fibre coupled gas cells," at Field Laser Applications in Industry and Research, 2018(Poster presentation)

J. A. A. Bremner, T. Kissinger, J. Hodgkinson, and R. P. Tatam, "A comparison of topologies used in an interferometric gas detection technique," Proceedings .SPIE, vol.11354, 2020(Invited Talk).

J. A. Bremner, T. Kissinger, J. Hodgkinson, and R. Tatam, "The use of range resolved interferometry for multi point methane detection (Poster presentation accepted but cancelled due to Covid restrictions)," 27th International Conference on Optical Fiber Sensors ,2020.

AWARDS AND OTHER CONFERENCES

J. Bremner, T. Kissinger, J. Hodgkinson, and R. P. Tatam, "Multiplexed gas detection with range resolved interferometry," Early Career researchers in gas/volatile analysis and sensing (Gas analysis and sensing group),2020(Awarded 2nd place in oral presentation competition).

RESEARCH FUNDING ARISING FROM WORK PRESENTED IN THIS THESIS

J. Hodgkinson, T. Kissinger, and R. P. Tatam, "Optical fibre linked gas sensors,"EPSRC Impact Acceleration Award, 2019 £9193 (3 months)

J. Hodgkinson, T. Kissinger, and R. P. Tatam, "Optical fibre linked gas sensors,"EPSRC Impact Acceleration Award, 2020 £36244 (6 months)

PATENT APPLICATION

J. Bremner, T. Kissinger, E. J. Hodgkinson, and R. P. Tatam, Fluid sensing systems and methods, WO2020/049287 2021

A

HARDWARE IMPLEMENTATION

The experimental work in this thesis was performed using two hardware systems, both designed in the Centre for Engineering Photonics. The work described in Chapter 5 was performed on a system designed to support the work of T Kissinger in he PhD thesis[128] and has therefore been referred to in this work as the Kissinger system. The work described in Chapter 6 was designed for the work of K Wiseman and is therefore referred to as the Wiseman system. Both systems were altered by the author of this thesis for use in the experimental work described here.

A.1 KISSINGER SYSTEM

This system was built around a Terasic DE-115 development board that uses a Altera Cyclone IV FPGA. It is the field programmable gate array (FPGA) that performs the demodulation calculations described in Chapter 4. The System is capable of interrogating 24 range channels simultaneously and can provide a modulation to the laser at frequencies of 49kHz.

Figure A.1: The hardware system used for the experimental work described in Chapter 5

A.2   WISEMAN SYSTEM

The Kissinger system was not capable of providing the preshaping required in Chapter 6 and the code was not easily amended and so an alternative system was built based on work done for the the PhD thesis of Keiran Wiseman and is consequently referred to as the Wiseman system. This is based on National Instruments hardware NI 9755 analogue to digital input and a NI 9262 digital to analogue output controlled by a CRIO FPGA system. Software had been written by K Wiseman to perform RRI analysis and that software was adjusted by the author of this thesis to allow the addition of a ramp modulation and a preshaping of the sinusoidal modulation. This system was capable of producing a sinusoidal modulation at an frequency of 1133Hz, and with 14 bit resolution over a ±10V range giving a resolution of approximately 0.08V.

Figure A.2: The hardware system used for the experimental work described in Chapter 6

REFERENCES

[1] M. Righettoni, A. Tricoli, and S. E. Pratsinis, "Si:WO3 sensors for highly selective detection of acetone for easy diagnosis of diabetes by breath analysis," *Analytical Chemistry*, vol. 82, no. 9, 3581–3587, 2010.

[2] S. M. Cristescu, S. T. Persijn, S. Te Lintel Hekkert, and F. J. Harren, "Laser-based systems for trace gas detection in life sciences," *Applied Physics B: Lasers and Optics*, vol. 92, 343–349, 2008.

[3] P. E. Dennison, A. K. Thorpe, E. R. Pardyjak, D. A. Roberts, Y. Qi, R. O. Green, E. S. Bradley, and C. C. Funk, "High spatial resolution mapping of elevated atmospheric carbon dioxide using airborne imaging spectroscopy: Radiative transfer modeling and power plant plume detection," *Remote Sensing of Environment*, vol. 139, 116–129, 2013.

[4] D. R. Thompson, I. Leifer, H. Bovensmann, M. Eastwood, M. Fladeland, C. Frankenberg, K. Gerilowski, R. O. Green, S. Kratwurst, T. Krings, B. Luna, and A. K. Thorpe, "Real-time remote detection and measurement for airborne imaging spectroscopy: A case study with methane," *Atmospheric Measurement Techniques*, vol. 8, no. 10, 4383–4397, 2015.

[5] O. Hennig, R. Strzoda, E. Mágori, E. Chemisky, C. Tump, M. Fleischer, H. Meixner, and I. Eisele, "Hand-held unit for simultaneous detection of methane and ethane based on NIR-absorption spectroscopy," *Sensors and Actuators, B: Chemical*, vol. 95, 151–156, 2003.

[6] G. Eranna, B. C. Joshi, D. P. Runthala, and R. P. Gupta, "Oxide materials for development of integrated gas sensors - A comprehensive review,"

Critical Reviews in Solid State and Materials Sciences, vol. 29, no. 3-4, 111–188, 2004.

[7]   United Nations Trust Fund for Human Security, "Human Security: Building Resilience to Climate Threats," 2015.

[8]   *Paris Agreement to the United Nations Framework Convention on Climate Change*, 2015.

[9]   International Protocol on Climate Change, "Climate Change 2014 Synthesis Report: Summary Chapter for Policymakers," in *IPCC: Climate Change 2014: Synthesis Report. Contribution of Working Groups I, II and III to the Fifth Assessment Report of the Intergovernmental Panel on Climate Change*, R. Pachauri and L. Meyer, Eds., 2014.

[10]   J. J. Davenport, J. Hodgkinson, J. R. Saffell, and R. P. Tatam, "Non-Dispersive Ultra-Violet Spectroscopic Detection of Formaldehyde Gas for Indoor Environments," *IEEE Sensors Journal*, vol. 18, no. 6, 2218–2228, 2018.

[11]   G. G. Mandayo, E. Castaño, and F. J. Gracia, "Carbon monoxide detector fabricated on the basis of a tin oxide novel doping method," *IEEE Sensors Journal*, vol. 2, no. 4, 322–327, 2002.

[12]   Det Norske Veritas Industry AS, *Accident statistics for fixed offshore units on the UK Continental Shelf for the Health and Safety Executive 2003 Accident statistics for fixed offshore units on the UK Continental Shelf*. HSE, 2003.

[13]   M. G. Zabetakis, *Flammability characteristics of combustible gases and vapors*. Washington DC: Bureau Of Mines, 1965.

[14]   Health And Safety Executive, *Offshore gas detector siting criterion investigation of detector spacing*. London: HSE, 1993.

[15] R. Gonzalez-Valencia, F. Magana-Rodriguez, J. Cristóbal, and
      F. Thalasso, "Hotspot detection and spatial distribution of methane
      emissions from landfills by a surface probe method," *Waste Management*,
      vol. 55, 299–305, 2016.

[16] N. Dossi, R. Toniolo, A. Pizzariello, E. Carrilho, E. Piccin, S. Battiston,
      and G. Bontempelli, "An electrochemical gas sensor based on paper
      supported room temperature ionic liquids," *Lab on a Chip*, vol. 12, no. 1,
      153–158, 2012.

[17] M. Bavcon, P. Trebše, and L. Zupančič-Kralj, "Investigations of the
      determination and transformations of diazinon and malathion under
      environmental conditions using gas chromatography coupled with a
      flame ionisation detector," *Chemosphere*, vol. 50, no. 5, 595–601, 2003.

[18] W. Wang, H. Hu, X. Liu, S. He, Y. Pan, C. Zhang, and C. Dong,
      "Development of a room temperature SAW methane gas sensor
      incorporating a supramolecular cryptophane A coating," *Sensors
      (Switzerland)*, vol. 16, no. 1, 73, 2016.

[19] J. Hodgkinson and R. P. Tatam, "Optical gas sensing: A review,"
      Measurement Science and Technology, vol. 24, no. 1, 012004, 2013.

[20] D. L. Andrews and A. A. Demidov, Eds., *An Introduction To Laser
      Spectrsocopy*, 2nd. New York: Kluwer Academic, 2002.

[21] H. Nasim and Y. Jamil, "Recent advancements in spectroscopy using
      tunable diode lasers," *Laser Physics Letters*, vol. 10, no. 4, 043001, 2013.

[22] G. Stewart, C. Tandy, D. Moodie, M. A. Morante, and F. Dong, "Design
      of a fibre optic multi-point sensor for gas detection," *Sensors and
      Actuators, B: Chemical*, vol. 51, 227–232, 1998.

[23] X. Lou, Y. Feng, C. Chen, and Y. Dong, "Multi-point spectroscopic gas
      sensing based on coherent FMCW interferometry," *Optics Express*,
      vol. 28, no. 6, 9014–9026, 2020.

[24] T. Kissinger, T. O. Charrett, and R. P. Tatam, "Range-resolved interferometric signal processing using sinusoidal optical frequency modulation," *Optics Express*, vol. 23, no. 7, 9415–9431, 2015.

[25] A. Garcia-Ruiz, J. Pastor-Graells, H. F. Martins, K. H. Tow, L. Thévenaz, S. Martin-Lopez, and M. Gonzalez-Herraez, "Distributed photothermal spectroscopy in microstructured optical fibers: towards high-resolution mapping of gas presence over long distances," *Optics Express*, vol. 25, no. 3, 1789–1805, 2017.

[26] T. Kissinger, R. Correia, T. O. Charrett, S. W. James, and R. P. Tatam, "Fiber segment interferometry for dynamic strain measurements," *Journal of Lightwave Technology*, vol. 34, no. 19, 4620–4626, 2016.

[27] NOAA, *Global Monitoring Laboratory - Carbon Cycle Greenhouse Gases*, https://www.esrl.noaa.gov/gmd/ccgg/trends/monthly.html (Date accessed 29 Sep 2020).

[28] T. F. Stocker, Q. Dahe, G.-K. Plattner, M. M. Tignor, S. K. Allen, J. Boschung, A. Nauels, Y. Xia, V. Bex, and P. M. Vincent, *IPCC, 2013: Climate Change 2013: The Physical Science Basis. Contribution of Working Group I to the Fifth Assessment Report of the Intergovernmental Panel on Climate Change*. 2013, 203.

[29] Y. Cai, X. Cai, R. L. Desjardins, D. E. Worth, and R. Srinivasan, "Methane emissions from a waste treatment site: Numerical analysis of aircraft-based data," *Agricultural and Forest Meteorology*, vol. 292-293, 108102, 2020.

[30] K. Rashid, A. Speck, T. P. Osedach, D. V. Perroni, and A. E. Pomerantz, "Optimized inspection of upstream oil and gas methane emissions using airborne LiDAR surveillance," *Applied Energy*, vol. 275, no. June, 1–8, 2020.

[31]   IEA, *Methane emissions from oil and gas – Tracking Fuel Supply – Analysis*,
       https://www.iea.org/reports/methane-emissions-from-oil-and-gas
       (Date accessed: 29 Sep 2020).

[32]   S. Chaulya and G. Prasad, *Gas Sensors for Underground Mines and
       Hazardous Areas*. Elvesier, 2016.

[33]   Institute of Gas Engineers, *Dealing with reported gas escapes*.
       Loughborough: Institute Of Gas Engineers and Managers, 1998.

[34]   ION Science, *The Role of Gas Detection in OffShore Applications*,
       https://www.ionscience-usa.com/news/gas-detection-offshore-
       applications (Date accessed: 13 Oct
       2020).

[35]   British Standards Institution, "BS EN 50241-2:1999 Specification for open
       path apparatus for the detection of combustible or toxic gases and
       vapours—Part 2: Performance requirements for apparatus for the
       detection of combustible gases," 1999.

[36]   J. Hodgkinson and R. D. Pride, "Methane-specific gas detectors: The
       effect of natural gas composition," *Measurement Science and Technology*,
       vol. 21, no. 10, 105103, 2010.

[37]   J. Sharaf, "Exhaust Emissions and Its Control Technology for an Internal
       Combustion Engine," *International Journal of Engineering Research and
       Applications (IJERA) www.ijera.com*, vol. 3, no. 4, 947–960, 2013.

[38]   W. Kuipers and J. Müller, "Sensitivity of a planar micro-flame ionization
       detector," *Talanta*, vol. 82, no. 5, 1674–1679, 2010.

[39]   Cambustion, *Fast FID Principles*,
       https://www.cambustion.com/products/knowledgebase/fast-fid-
       principles (Date accessed: 3 May
       2020).

[40]   RAE Systems, *Comparison of photoionization detectors (PIDs) and flame ionization detectors (FIDs)*, https://safety.honeywell.com/content/dam/his-sandbox/marketing/gas-and-flame-detection/documents/RS_app-notes_application-note-226_comparison-of-photoionization-detector.pdf (Accessed: 13th Jan 2020).

[41]   B. Caballero, P. M. Finglas, and F. B. T. Toldrá, Eds., *Encyclopedia of Food and Health*. Oxford: Academic Press, 2016.

[42]   H. A. Mohammed, M. S. Al-Omar, S. A. Mohammed, M. S. Aly, A. N. Alsuqub, and R. A. Khan, "Drying induced impact on composition and oil quality of rosemary herb, Rosmarinus officinalis Linn.," *Molecules*, vol. 25, no. 12, 2830, 2020.

[43]   Sick, *Extractive gas analyzers | EuroFID3010*, https://www.sick.com/gb/en/gas-analyzers/extractive-gas-analyzers/eurofid3010/c/g54725 (Date accessed: 2 Jan 2021).

[44]   J. Y. Yoon, *Introduction to Biosensors: From Electric Circuits to Immunosensors: Second edition*. Springer International Publishing, 2016.

[45]   Z. Yunusa, M. N. Hamidon, A. Kaiser, and Z. Awang, "Gas Sensors: A Review," *Sensors & Transducers*, vol. 168, no. 4, 61–75, 2014.

[46]   Climate Control Middle East, *Getting Sensitised to Sensors*, http://climatecontrolme.com/2014/08/getting-sensitised-to-sensors/ (Date accessed: 3 May 2021).

[47]   T. Romih, E. Menart, V. Jovanovski, A. Jerič, S. Andrenšek, and S. Hočevar, "Sodium-Polyacrylate-Based Electrochemical Sensors for Highly Sensitive Detection of Gaseous Phenol at Room Temperature," *ACS Sensors*, vol. 5, no. 8, 2570–2577, 2020.

[48] H. Zhang, J. Liu, Q. Liu, R. Chen, H. Zhang, J. Yu, D. Song, X. Jing, M. Zhang, and J. Wang, "Electrochemical Oxygen Sensor Based on the Interaction of Double-Layer Ionic Liquid Film (DLILF)," *Journal of The Electrochemical Society*, vol. 165, no. 16, B779–B786, 2018.

[49] Z. Li, H. Li, Z. Wu, M. Wang, J. Luo, H. Torun, P. Hu, C. Yang, M. Grundmann, X. Liu, and Y. Fu, "Advances in designs and mechanisms of semiconducting metal oxide nanostructures for high-precision gas sensors operated at room temperature," *Materials Horizons*, vol. 6, no. 3, 470–506, 2019.

[50] J. R. Saffell, M. L. Hitchman, and D. H. Dawson, *Electrochemical sensor for determining analyte in the presence of interferent and method of using the sensor*, 2001.

[51] P. K. Sekhar, J. Kysar, E. L. Brosha, and C. R. Kreller, "Development and testing of an electrochemical methane sensor," *Sensors and Actuators, B: Chemical*, vol. 228, 162–167, 2016.

[52] G. Korotcenkov, "Metal oxides for solid-state gas sensors: What determines our choice?" *Materials Science and Engineering B: Solid-State Materials for Advanced Technology*, vol. 139, no. 1, 1–23, 2007.

[53] T. Hong, J. T. Culp, K. J. Kim, J. Devkota, C. Sun, and P. R. Ohodnicki, "State-of-the-art of methane sensing materials: A review and perspectives," *TrAC - Trends in Analytical Chemistry*, vol. 125, 115820, 2020.

[54] P. Bhattacharyya, P. K. Basu, N. Mukherjee, A. Mondal, H. Saha, and S. Basu, "Deposition of nanocrystalline ZnO thin films on p-Si by novel galvanic method and application of the heterojunction as methane sensor," *Journal of Materials Science: Materials in Electronics*, vol. 18, no. 8, 823–829, 2007.

[55]   G. K. Flingelli, M. M. Fleischer, and H. Meixner, "Selective detection of methane in domestic environments using a catalyst sensor system based on Ga2O3," *Sensors and Actuators, B: Chemical*, vol. 48, no. 1-3, 258–262, 1998.

[56]   X. Liu, S. Cheng, H. Liu, S. Hu, D. Zhang, and H. Ning, "A survey on gas sensing technology.," *Sensors (Switzerland)*, vol. 12, no. 7, 9635–65, 2012.

[57]   A. H. F. Hazadi, A. A. M. Ralib, and N. Saidin, "Design and Simulation of Electroacoustic Sensor for exhaled breath analysis," in *Proceedings of the 2018 7th International Conference on Computer and Communication Engineering, ICCCE 2018*, IEEE, 2018, 388–391.

[58]   W. P. Jakubik, "Surface acoustic wave-based gas sensors," in *Thin Solid Films*, vol. 520, 2011, 986–993.

[59]   P. Moseley and B. Tofield, *Solid State Gas Sensors*, P. Mosely and M. Tofield, Eds. Bristol: CRC Press, 1987.

[60]   J. M. Hollas, *Modern Spectroscopy*, Fourth Edi. New York: John Wiley and Sons, 2004.

[61]   C. Banwell and E. McCash, *Fundamentals of Molecular Spectroscopy*. London, UK: McGraw-Hill, 1994.

[62]   I. E. Gordon *et al.*, "The HITRAN2016 molecular spectroscopic database," *Journal of Quantitative Spectroscopy and Radiative Transfer*, vol. 203, 3–69, 2017.

[63]   A. D. McNaught and A. Wilkinson, Eds., *Compendium of Chemical Terminology*. Oxford: Blackwell Scientific Publications, 2006.

[64]   E. D. Hinkley and P. L. Kelley, "Detection of air pollutants with tunable diode lasers," *Science*, vol. 171, no. 3972, 635–639, 1971.

[65] A. H. Hartog, "A distributed temperature sensor based on liquid core optical fibers," *Journal of Lightwave Technology*, vol. 1, no. 3, 498–509, 1983.

[66] J. Reid, J. Shewchun, B. K. Garside, and E. A. Ballik, "High sensitivity pollution detection employing tunable diode lasers," *Applied Optics*, vol. 17, no. 2, 300, 1978.

[67] M. Newville, T. Stensitzki, D. B. Allen, and A. Ingargiola, "LMFIT: Non-Linear Least-Square Minimization and Curve-Fitting for Python," 2014.

[68] NEL Laser Diodes, *NLK1U5EAAA data sheet*, https://www.acalbfi.com/uk/media/ UK_NEL_NLK1U5EAAA_DS?pegId= productDetails&product=000000000Y (Date accessed: 23 Jan 2020).

[69] P. Werle, F. Slemr, K. Maurer, R. Kormann, R. Mücke, and B. Jänker, "Near- and mid-infrared laser-optical sensors for gas analysis," *Optics and Lasers in Engineering*, vol. 37, no. 2-3, 101–114, 2002.

[70] D. S. Bomse, A. C. Stanton, and J. A. Silver, "Frequency modulation and wavelength modulation spectroscopies: comparison of experimental methods using a lead-salt diode laser," *Applied Optics*, vol. 31, no. 6, 718, 1992.

[71] J. A. Silver and A. C. Stanton, "Optical interference fringe reduction in laser absorption experiments," *Applied Optics*, vol. 27, no. 10, 1914–1916, 1988.

[72] D. Masiyano, J. Hodgkinson, S. Schilt, and R. P. Tatam, "Self-mixing interference effects in tunable diode laser absorption spectroscopy," *Applied Physics B: Lasers and Optics*, vol. 96, no. 4, 863–874, 2009.

[73] H. I. Schiff, G. I. Mackay, and J. Bechara, "The use of tunable diode laser absorption spectroscopy for atmospheric measurements," in *Air*

Monitoring by Spectroscopic Techniques, M. W. Sigrist, Ed., New York: Wiley, 1994, ch. 5.

[74]   J. Reid, M. El-Sherbiny, B. K. Garside, and E. A. Ballik, "Sensitivity limits of a tunable diode laser spectrometer, with application to the detection of NO2 at the 100-ppt level," *Applied Optics*, vol. 19, no. 19, 3349–3354, 1980.

[75]   C. B. Carlisle and D. E. Cooper, "Quantum limited FM spectroscopy with a lead-salt diode laser," vol. 28, no. 13, 68–69, 1989.

[76]   A. Hartmann, R. Strzoda, R. Schrobenhauser, and R. Weigel, "Arithmetical elimination of superimposed interference modulation in laser spectroscopic gas concentration measurements," *Procedia Engineering*, vol. 47, 1350–1353, 2012.

[77]   W. Ma, W. Yin, L. Dong, L. Wang, C. Li, and S. Jia, "High-sensitivity detection of methane near 6106 cm-1 using tunable external-cavity diode laser," *Japanese Journal of Applied Physics, Part 1: Regular Papers and Short Notes and Review Papers*, vol. 44, no. 4 A, 1961–1965, 2005.

[78]   K. Duffin, A. J. McGettrick, W. Johnstone, G. Stewart, and D. G. Moodie, "Tunable diode-laser spectroscopy with wavelength modulation: A calibration-free approach to the recovery of absolute gas absorption line shapes," *Journal of Lightwave Technology*, vol. 25, no. 10, 3114–3125, 2007.

[79]   S. Schilt, L. Thévenaz, and P. Robert, "Wavelength modulation spectroscopy: combined frequency and intensity laser modulation," *Applied Optics*, vol. 42, no. 33, 6728–6738, 2003.

[80]   D. G. Lancaster, D. Richter, R. F. Curl, and F. K. Tittel, "Real-time measurements of trace gases using a compact difference-frequency-based sensor operating at 3.5 μm," *Applied Physics B: Lasers and Optics*, vol. 67, 339–345, 1998.

[81] G. Wysocki, Y. Bakhirkin, S. So, F. K. Tittel, C. J. Hill, R. Q. Yang, and M. P. Fraser, "Dual interband cascade laser based trace-gas sensor for environmental monitoring," *Applied Optics*, vol. 46, no. 33, 8202–8210, 2007.

[82] G. Gagliardi, S. Borri, F. Tamassia, F. Capasso, C. Gmachl, D. L. Sivco, J. N. Baillargeon, A. L. Hutchinson, and A. Y. Cho, "A frequency-modulated quantum-cascade laser for spectroscopy of CH4 and N2O isotopomers," *Isotopes in Environmental and Health Studies*, vol. 41, no. 4, 313–321, 2005.

[83] A. G. Bell, "On the production and reproduction of sound by light," *American Journal of Science*, vol. s3-20, no. 118, 305–324, 1880.

[84] S. Crouch, D. Skoog, and F. Holler, *Principles of Instrumental Analysis*, Mason OH, 2017.

[85] T. Yang, W. Chen, and P. Wang, "A review of all-optical photoacoustic spectroscopy as a gas sensing method," *Applied Spectroscopy Reviews*, vol. 56, no. 2, 143–170, 2020.

[86] T. Yanzhen, Y. Fan, M. Jun, H. Hoi Lut, and J. Wei, "All-fiber photoacoustic gas sensor with graphene nano-mechanical resonator as the acoustic detector," in *24th International Conference on Optical Fibre Sensors*, vol. 9634, 2015, 1–4.

[87] K. Chen, Y. Chen, B. Zhang, L. Mei, M. Guo, H. Deng, S. Liu, F. Ma, Z. Gong, and Q. Yu, "Highly sensitive photoacoustic microcavity gas sensor for leak detection," *Sensors (Switzerland)*, vol. 20, no. 4, 1–10, 2020.

[88] S. Palzer, "Photoacoustic-based gas sensing: A review," *Sensors (Switzerland)*, vol. 20, no. 9, 2745, 2020.

[89] S. Schilt, J. P. Besson, and L. Thévenaz, "Near-infrared laser photoacoustic detection of methane: The impact of molecular

relaxation," *Applied Physics B: Lasers and Optics*, vol. 82, no. 2 special issue, 319–329, 2006.

[90] J. Wong and R. Anderson, *Non-Dispersive Infrared Gas Measurement*. International Frequency Sensor Association (IFSA) Publishing, 2012.

[91] C. Massie, G. Stewart, G. McGregor, and J. R. Gilchrist, "Design of a portable optical sensor for methane gas detection," *Sensors and Actuators B: Chemical*, vol. 113, no. 2, 830–836, 2006.

[92] S. E. Alexandrov, G. A. Gavrilov, A. A. Kapralov, S. A. Karandashev, B. A. Matveev, G. Y. Sotnikova, and N. M. Stus', "Portable optoelectronic gas sensors operating in the mid-IR spectral range (λ=3 5 µm)," in *Second International Conference on Lasers for Measurement and Information Transfer;*, V. E. Privalov, Ed., St Petersburg, 2002, 188–194.

[93] Alphasense, *IRM-AT Methane IR sensor - Thermopile detector*, http://www.alphasense.com/WEB1213/wp-content/uploads/2015/05/IRM-AT.pdf (Date accessed: 20 Oct 2019).

[94] M. Nikodem and G. Wysocki, "Molecular dispersion spectroscopy - new capabilities in laser chemical sensing," *Annals of the New York Academy of Sciences*, vol. 1260, no. 1, 101–111, 2012.

[95] M. Nikodem and G. Wysocki, "Differential optical dispersion spectroscopy," *IEEE Journal of Selected Topics in Quantum Electronics*, vol. 23, no. 2, 464–468, 2017.

[96] M. Nikodem, "Chirped laser dispersion spectroscopy for remote open-path trace-gas sensing," *Sensors (Switzerland)*, vol. 12, 16466–16481, 2012.

[97] G. Plant, M. Nikodem, P. Mulhall, R. K. Varner, D. Sonnenfroh, and G. Wysocki, "Field test of a remote multi-path CLaDS methane sensor," *Sensors*, vol. 15, no. 9, 21315–21326, 2015.

[98]   Mirico, *Orion CH4*, https://mirico.co.uk/orion-ch4/ (Date accessed: 13 Jan 2021).

[99]   E. C. Richard, K. K. Kelly, R. H. Winkler, R. Wilson, T. L. Thompson, R. J. McLaughlin, A. L. Schmeltekopf, and A. F. Tuck, "A fast-response near-infrared tunable diode laser absorption spectrometer for in situ measurements of CH4 in the upper troposphere and lower stratosphere," *Applied Physics B: Lasers and Optics*, vol. 75, no. 2-3, 183–194, 2002.

[100]   B. H. Hjertager, K. Fuhre, and M. Bjørkhaug, "Concentration effects on flame acceleration by obstacles in large-scale methane-air and propane-air vented explosions," *Combustion Science and Technology*, vol. 62, no. 4-6, 239–256, 1988.

[101]   A. Kelsey, M. A. Hemingway, P. T. Walsh, and S. Connolly, "Evaluations of flammable gas detector networks based on experimental simulations of offshore , high pressure gas releases," *Transactions of the Institution of Chemical Engineers*, vol. 80, no. 2, 78–86, 2002.

[102]   X. Wang, X. Zhao, Z. Liang, and M. Tan, "Deploying a wireless sensor network on the coal mines," in *2007 IEEE International Conference on Networking, Sensing and Control*, IEEE, 2007, 324–328.

[103]   *The Smoke and Carbon Monoxide Alarm (England) Regulations*, SI 2015/16. 2015.

[104]   Y. B. Wei, J. Chang, J. Lian, and T. Y. Liu, "Multi-point optical fibre oxygen sensor based on laser absorption spectroscopy," *Optik*, vol. 126, no. 20, 2394–2397, 2015.

[105]   J. Hodgkinson, R. Pride, C. Tandy, D. G. Moodie, and G. Stewart, "Field evaluation of a multipoint fiber optic sensor array for methane detection (OMEGA)," in *Applications of Optical Fiber Sensors*, vol. 4074, SPIE, 2000, 90–98.

[106] C. Liu, Z. Cao, F. Li, Y. Lin, and L. Xu, "Flame monitoring of a model swirl injector using 1D tunable diode laser absorption spectroscopy tomography," *Measurement Science and Technology*, vol. 28, no. 5, 54002, 2017.

[107] C. Liu and L. Xu, "Laser absorption spectroscopy for combustion diagnosis in reactive flows: A review," *Applied Spectroscopy Reviews*, vol. 54, no. 1, 1–44, 2019.

[108] B. Culshaw, W. Johnstone, A. McLean, I. Mauchline, D. Moodie, and G. Stewart, "Large scale multiplexing a point sensor for methane gas detection," in *2002 15th Optical Fiber Sensors Conference Technical Digest, OFS 2002*, vol. 1, IEEE, 2002, 261–264.

[109] Z. L. Wang, C. W. Tian, Q. Liu, J. Chang, Q. D. Zhang, and C. G. Zhu, "Wavelength modulation technique-based photoacoustic spectroscopy for multipoint gas sensing," *Applied Optics*, vol. 57, no. 11, 2909–2914, 2018.

[110] C. Zhang, Y. Yang, Y. Lin, Y. Tan, M. Lengden, G. Humphries, W. Johnstone, H. L. Ho, and W. Jin, "All-optical fiber multi-point photoacoustic spectroscopic gas sensing system," in *26th International Conference on Optical Fiber Sensors*, OSA, 2018, WF17.

[111] Q. Zhang, J. Chang, Z. Cong, Z. Wang, F. Wang, J. Sun, and C. Zhu, "Intra-cavity multi-point sensor for C2H2 detection in photoacoustic spectroscopy based on acousto-optic Q-switched fiber laser," *Optik*, vol. 206, 164277, 2020.

[112] H. Lo, W. Jin, and M. Demoka, "Sensitive, multipoint gas detection using TDM and wavelength modulation spectroscopy," *Electronics Letters*, vol. 36, no. 14, 1191–1193, 2000.

[113]   H. L. Ho, W. Jin, and M. S. Demokan, "Time division multiplexed gas
        sensing system with a forward-coupled ladder topology," in *International
        Conference on Sensors and Control Techniques*, vol. 4077, 2000, 7–10.

[114]   W. Jin, "Performance analysis of a timedivision-multiplexed fiber-optic
        gas-sensor array by wavelength modulation of a distributed-feedback
        laser," *Applied Optics*, vol. 38, no. 25, 5290–5297, 2001.

[115]   Y. Lin, F. Liu, X. He, W. Jin, M. Zhang, F. Yang, H. L. Ho, Y. Tan, and
        L. Gu, "Distributed gas sensing with optical fibre photothermal
        interferometry," *Optics Express*, vol. 25, no. 25, 31568–31585, 2017.

[116]   J. P. Parry, B. C. Griffiths, N. Gayraud, E. D. McNaghten, A. M. Parkes,
        W. N. MacPherson, and D. P. Hand, "Towards practical gas sensing with
        micro-structured fibres," *Measurement Science and Technology*, vol. 20,
        no. 7, 075301, 2009.

[117]   M. N. Petrovich, C. Grivas, F. Poletti, A. van Brakel, E. Austin, and
        D. J. Richardson, "Microstructured optical fibers for gas sensing: design,
        fabrication, and post-fab processing," in *20th International Conference on
        Optical Fibre Sensors*, vol. 7503, 2009, 750303.

[118]   A. van Brakel, C. Grivas, M. N. Petrovich, and D. J. Richardson,
        "Micro-channels machined in microstructured optical fibers by
        femtosecond laser," *Optics Express*, vol. 15, no. 14, 8731–8736, 2007.

[119]   A. A. Demidov, "Laser Remote Sensing," in *An Introduction To Laser
        Spectroscopy*, D. L. Andrews and A. A. Demidov, Eds., 2nd ed., New
        York: Kluwer Academic, 2002, 339–367.

[120]   A. Hauchecorne and M.-L. Chanin, "Density and temperature profiles
        obtained by lidar between 35 and 70 km," *Geophysical Research Letters*,
        vol. 7, no. 8, 565–568, 1980.

[121] M. L. Chanin, A. Garnier, A. Hauchecorne, and J. Porteneuve, "A Doppler lidar for measuring winds in the middle atmosphere," *Geophysical Research Letters*, vol. 16, no. 11, 1273–1276, 1989.

[122] D. Kim, H. Kang, J. Y. Ryu, S. C. Jun, S. T. Yun, S. C. Choi, S. H. Park, M. S. Yoon, and H. Lee, "Development of Raman lidar for remote sensing of CO_2 leakage at an artificial carbon capture and storage site," *Remote Sensing*, vol. 10, no. 9, 1439, 2018.

[123] R. W. Wolcott and R. M. Eustice, "Robust LIDAR localization using multiresolution Gaussian mixture maps for autonomous driving," *International Journal of Robotics Research*, vol. 36, no. 3, 292–319, 2017.

[124] L. De Paula Veronese, F. Auat-Cheein, F. Mutz, T. Oliveira-Santos, J. E. Guivant, E. De Aguiar, C. Badue, and A. F. De Souza, "Evaluating the limits of a LiDAR for an autonomous driving localization," *IEEE Transactions on Intelligent Transportation Systems*, vol. 22, no. 3, 1449–1458, 2021.

[125] I. Baldwin and P. Newman, "Road vehicle localization with 2D push-broom LIDAR and 3D priors," in *Proceedings - IEEE International Conference on Robotics and Automation*, 2012, 2611–2617.

[126] C. J. Karlsson, F. Å. A. Olsson, D. Letalick, and M. Harris, "All-fiber multifunction continuous-wave coherent laser radar at 1.55m for range , speed , vibration , and wind measurements," *Applied Optics*, vol. 39, no. 21, 3716–3726, 2000.

[127] M. Harris, G. N. Pearson, K. D. Ridley, C. J. Karlsson, F. Å. A. Olsson, and D. Letalick, "Single-particle laser Doppler anemometry at 155 μm," *Applied Optics*, vol. 40, no. 6, 969–973, 2001.

[128] T. Kissinger, "Range-resolved optical interferometric signal processing," Ph.D. dissertation, Cranfield University, 2015.

[129] M. K. Jindal, M. Mainuddin, S. Veerabuthiran, and A. K. Razdan, "Laser-based systems for standoff detection of CWA: a short review," *IEEE Sensors Journal*, vol. 21, no. 4, 4085–4096, 2021.

[130] O. A. Romanovskii, S. A. Sadovnikov, O. V. Kharchenko, and S. V. Yakovlev, "Remote analysis of methane concentration in the atmosphere with an IR lidar system in the 3300–3430 nm spectral range," *Atmospheric and Oceanic Optics*, vol. 33, no. 2, 188–194, 2020.

[131] N. Cezard, S. Le Mehaute, J. Le Gouët, M. Valla, D. Goular, D. Fleury, C. Planchat, A. A. A. Dolfi-Bouteyre, a. Perfor-, S. L. Mehaute, J. L. Gouët, and A. A. A. Dolfi-Bouteyre, "Performance assessment of a coherent DIAL-Doppler fiber lidar at 1645 nm for remote sensing of methane and wind," *Optics Express*, vol. 28, no. 15, 22345, 2020.

[132] Z. Ding, C. Wang, K. Liu, J. Jiang, D. Yang, G. Pan, Z. Pu, and T. Liu, "Distributed optical fiber sensors based on optical frequency domain reflectometry: A review," *Sensors (MDPI)*, vol. 18, no. 4, 1072, 2018.

[133] P. Lu, N. Lalam, M. Badar, B. Liu, B. T. Chorpening, M. P. Buric, and P. R. Ohodnicki, "Distributed optical fiber sensing: Review and perspective," *Applied Physics Reviews*, vol. 6, no. 4, 41302, 2019.

[134] C. Chen, S. Gao, L. Chen, and X. Bao, "Distributed high temperature monitoring of smf under electrical arc discharges based on OFDR," *Sensors (Switzerland)*, vol. 20, no. 22, 6407, 2020.

[135] I.-B. B. Kwon, Y.-S. S. Kwon, D.-C. C. Seo, D.-J. J. Yoon, and E. Kim, "A technic for ground anchor force determination from distributied strain using fiber optic ofdr sensor with the rejection of a temperature effect," *Applied Sciences (Basel)*, vol. 10, no. 23, 8437, 2020.

[136] T. Chen, Q. Wang, R. Chen, B. Zhang, K. P. Chen, M. Maklad, and P. R. Swinehart, "Distributed hydrogen sensing using in-fiber Rayleigh scattering," *Applied Physics Letters*, vol. 100, 191105, 2012.

[137] F. Ye, L. Qian, B. Qi, Fei Ye, Li Qian, and Bing Qi, "Multipoint chemical gas sensing using frequency shifted interferometry," *Journal of Lightwave Technology*, vol. 27, no. 23, 5356–5364, 2009.

[138] A. D. Kersey and A. Dandridge, "Distributed and multiplexed fibre-optic sensor systems," *Journal of the Institution of Electronic and Radio Engineers*, vol. 58, no. 5, 1988.

[139] A. D. Kersey and A. Dandridge, "Comparative analysis of multiplexing techniques for interferometric fiber sensors," in *Fibre Optics '89*, vol. 1120, 1989, 236–246.

[140] W. Jin, M. S. Demokan, G. Stewart, W. Philp, and B. Culshaw, "Performance limit of fibre-optic gas sensors from coherent backscatter," *IEEE Proceedings - Optoelectronics*, vol. 145, no. 3, 186–190, 1998.

[141] H. C. Lefevre, "Single-mode fibre fractional wave devices and polarisation controllers," *Electronics Letters*, vol. 16, no. 20, 778–780, 1980.

[142] D. W. Stowe, D. R. Moore, and R. G. Priest, "Polarization fading in fiber interferometric sensors," *IEEE Transactions on Microwave Theory and Techniques*, vol. 30, no. 10, 1632–1635, 1982.

[143] L. Li, Q. Ma, M. Cao, G. Zhang, Y. Zhang, L. Jiang, C. Gao, J. Yao, S. Gong, and W. Li, "High stability Michelson refractometer based on an in-fiber interferometer followed with a Faraday rotator mirror," *Sensors and Actuators, B: Chemical*, vol. 234, 674–679, 2016.

[144] N. J. Frigo, A. Dandridge, and A. B. Tveten, "Technique for elimination of polarisation fading in fibre interferometers," *Electronics Letters*, vol. 20, no. 8, 319–320, 1984.

[145] Z. Ren, K. Cui, R. Zhu, W. Peng, and J. Qian, "Efficient and compact inline interferometric fiber sensor array based on fiber Bragg grating and rectangular-pulse binary phase modulation," *IEEE Sensors Journal*, vol. 18, no. 23, 9556–9561, 2018.

[146] T. Kissinger, T. O. H. Charrett, S. W. James, A. Adams, A. Twin, and R. P. Tatam, "Simultaneous laser vibrometry on multiple surfaces with a single beam system using range-resolved interferometry," *Proc. SPIE 9525*, 952520, 2015.

[147] S. Weber, T. Kissinger, E. Chehura, S. Staines, J. Barrington, K. Mullaney, L. Z. Fragonara, I. Petrunin, S. James, M. Lone, and R. Tatam, "Application of fibre optic sensing systems to measure rotor blade structural dynamics," *Mechanical Systems and Signal Processing*, vol. 158, 107758, 2021.

[148] K. B. Wiseman, T. Kissinger, and R. P. Tatam, "Three-dimensional interferometric stage encoder using a single access port," *Optics and Lasers in Engineering*, vol. 137, no. 2021, 106342, 2021.

[149] T. O. Charrett, T. Kissinger, and R. P. Tatam, "Workpiece positioning sensor (wPOS): A three-degree-of-freedom relative end-effector positioning sensor for robotic manufacturing," in *12th CIRP Conference on Intelligent Computation in Manufacturing Engineering*, 2019.

[150] S. H. Pyun, J. Cho, D. F. Davidson, and R. K. Hanson, "Interference-free mid-IR laser absorption detection of methane," *Measurement Science and Technology*, vol. 22, no. 2, 025303, 2011.

[151] P. Werle, F. Slemr, M. Gehrtz, and C. Bräuchle, "Wideband noise characteristics of a lead-salt diode laser: possibility of quantum noise limited TDLAS performance," *Applied Optics*, vol. 28, no. 9, 1638, 1989.

[152] Thor Labs, *Polarization change after propagation through a prism retroreflector*, https://www.thorlabs.com/newgrouppage9.cfm?objectgroup_id=9030 (Date Accessed: 20 Jun 2021).

[153] H. Atcha and R. P. Tatam, "Heterodyning of fibre optic electronic speckle pattern interferometers using laser diode wavelength modulation," *Measurement Science and Technology*, vol. 5, no. 6, 704–709, 1994.

[154] J. L. Santos, T. P. Newson, and D. A. Jackson, "Electronic speckle-pattern interferometry using single-mode fibers and active fringe stabilization," *Optics Letters*, vol. 15, no. 10, 573–575, 1990.

[155] C. C. Teng, E. J. Zhang, C. Xiong, W. M. J. Green, and G. Wysocki, "Dynamic computational optical fringe mitigation in tunable laser absorption spectroscopy," *Optics Express*, vol. 28, no. 26, 39017–39023, 2020.

[156] J. Yang, C. Yu, Z. Chen, J. Ng, and X. Yang, "Suppression of polarisation-induced signal fluctuation in optic distributed sensing system based on stimulated Brillouin scattering," *Electronics letters*, vol. 45, no. 3, 154–156, 2009.

[157] M. A. Abbas, L. van Dijk, K. E. Jahromi, M. Nematollahi, F. J. Harren, and A. Khodabakhsh, "Broadband time-resolved absorption and dispersion spectroscopy of methane and ethane in a plasma using a mid-infrared dual-comb spectrometer," *Sensors (MDPI)*, vol. 20, no. 23, 6831, 2020.

[158] Z. Wang, K. P. Cheong, M. Li, Q. Wang, and W. Ren, "Theoretical and experimental study of heterodyne phase-sensitive dispersion spectroscopy with an injection-current-modulated quantum cascade laser," *Sensors (MDPI)*, vol. 20, no. 21, 6176, 2020.

[159] Wavelength References, *Single-mode fiber-coupled gas flowcells*, https://www.wavelengthreferences.com/wp-content/uploads/Data-FCS-2019.pdf (Date accessed: 31 Mar 2021).

[160] M. Li, J.-m. Dai, and G.-d. Peng, "Thin gas cell with GRIN fiber lens for intra-cavity fiber laser gas sensors," *International Symposium on Photoelectronic Detection and Imaging 2009: Laser Sensing and Imaging*, vol. 7382, 73823Q–8, 2009.

[161] W. Jin, H. F. Xuan, and H. L. Ho, "Sensing with hollow-core photonic bandgap fibers," *Measurement Science and Technology*, vol. 21, 094014, 2010.

[162] B. M. Masum, S. M. Aminossadati, C. R. Leonardi, M. S. Kizil, and M. Amanzadeh, "Numerical analysis of gas diffusion in drilled hollow-core photonic crystal fibres," *Measurement: Journal of the International Measurement Confederation*, vol. 127, 283–291, 2018.